Toward Practical Multi-Reference Configuration Interaction Methods and Applications

Hang Hu

A dissertation
submitted in partial fulfillment of the
requirements for the degree of

Doctor of Philosophy

University of Washington

2023

Reading Committee:

Xiaosong Li, Chair

Cody Schlenker

Stefan Stoll

Ting Cao

Program Authorized to Offer Degree:
Molecular Engineering and Sciences

University of Washington

Abstract

Toward Practical Multi-Reference Configuration Interaction Methods and Applications

Hang Hu

Chair of the Supervisory Committee:
Xiaosong Li
Department of Chemistry

The accurate description of electronic structures in molecular systems has always been the central question in the field of quantum chemistry. For problems such as studying chemical properties of the late-row element components or investigating the energy dissipation pathways in electronically excited/ionized molecules, relativistic effects, static and dynamic electron correlations must be addressed. Despite of the simple formalism, the multireference configuration interaction (MRCI) method can treat both electron correlations and relativistic effects variationally with high accuracy. However, the large scaling of computational resources demanded by MRCI method becomes the bottleneck to apply it to any realistic systems. To shed lights on practical approaches to perform MRCI calculations, this dissertation covers important aspects including correlation space tuning to lower the number of determinants and algorithm advancements to increase the computational capability. Particularly, with the novel implementation, relativistic MRCI wavefunction with more than 1 billion determinants could be resolved using just a few computer machines. After a brief introduction to the preliminary theory concepts in Chapter 1, Chapter 2 further reviews the research and development effort for CI algorithm in the past three decades. Chapter 3 introduces a novel relativistic MRCI formalism and its distributed implementation, and parallel performance is evaluated and discussed. Chapter 4 discussed about how correlation tuning could impact MRCI calculations. Chapter 5 and 6 focused real world applications of

MRCI methods to resolve X-ray absorption spectra of iron complex and study non-radiative decay pathways of electronically excited/ionized molecules, respectively.

TABLE OF CONTENTS

LIST OF FIGURES

Figure Number Page

GLOSSARY

AO: Atomic Orbital

CAS: Complete Active Space.

CASCI: Complete Active Space Configuration Interaction

CASSCF: Complete Active Space Self-Consistent Field

CI: Configuration Interaction

FCI: Full Configuration Interaction

DGEMM: Double Precision General Matrix Multiplication

GHF: Generalized Hartree-Fock

GAS: Generalized Active Space

HF: Hartree-Fock

MCSCF: Multi-Configurational Self-Consistent Field

MO: Molecular Orbital

MPI: Message Passing Interface

MRCI: Multi-Reference Configuration Interactions

RAS: Restricted Active Space.

SA: State-Average

SOC: Spin-Orbit Coupling

SCF: Self-Consistent Field

SMP: Share-Memory multi-Processing

XAS: X-ray Absorption Spectra

X2C: Exact Two Component

ACKNOWLEDGMENTS

Six years ago, when I started this PhD student journey, I was not confident about the path awaiting in front of me. But now, looking back to the things I have achieved and the passion I found along the way, I can conclude that this journey has been very pleasant and worthwhile. There were a lot of struggles but luckily more help and support from all the people I could not ask for. Thus, here I want to express my gratitude to them.

First of all, I would like to thank my advisor Prof. Xiaosong Li. I know that from my bottom of my heart, without you, none of this wonderful journey could ever happen. When I came to you without any computational chemistry background, I was not expecting to be treat seriously. But instead, you gave the opportunity to learn, to grow and to make impact in this field. Your insightful guidance and endless enthusiasm towards sciences have influenced and helped me through many difficulties during my PhD study and will continue to support my mentality for a life time. You are always supportive, even when I was chasing my passion further in computer science beyond computational chemistry, you gave me so much encouragement I could not expect from any other advisors. It was truly a great honor and pleasure to work with you!

I would also like to thank my committee member, Prof. Cody Schlenker, Prof. Stefan Stoll, and Prof. Ting Cao, for supervising my research and providing me different perspectives that I would not easily think of.

I want to thank my colleagues in Li Group, who worked with me very closely in the past 6 years. Dr. Hongbin Liu and Dr. Andrew Jenkins gave me tremendous help when I was ramping up the domain knowledge of quantum chemistry, especially my initial implementations of MRCI on Gaussian. Dr. Hongbin Liu's unique insights in chemistry guided me through

a lot of application projects are well, and he also mentored me during my first internship at Microsoft Research. Lixin Lu worked closely with me for all the CI implementations in Chronus Quantum for the past three years. We spent days and nights for pushing the limit of relativistic MRCI methods and eventually our effor paid well. I would like to express my great gratitude to those three persons and the relativistic MRCI work are our mutual efforts. Besides, I would like to thank Dr. Tianyuan Zhang, Dr. Joshua Goings, Dr. Shichao Sun, Dr. Chad Hoyer, Dr. David Williams-Young, Dr. Andrew Wildman, Dr. Torin Stetina, Dr. Ryan Beck and all others in Li Group, for all the good science conversions and funny stories.

I felt great honor to work with many gifted experimental and theoretical scientists and I want express my thanks as well. Prof. Xin Zhang and Prof. Thomas Orlando, thanks for giving me the opportunities to work on the frontier science problems. Dr. Charles Wolstenholme, Dr. Conner Hoelzel, Brant Jones and Sramana Kundu, it was quite a pleasure to work with them. I would also like to thank Prof. Luna Huang, who taught me a lot on data science and we worked together to investigated how machine learning can be used in material sciences. I want to thank Dr. Mike Frisch who gave me the opportunities to learn programming and implement the proof-of-concept relativistic MRCI in Gaussian. All of our discussions on code performance laid out a great foundation for the later designs in Chronus Quantum.

I would like to thank my friends Quoc Truong, Yangpai Liu, Dr. Chris Lowy, Haoxuan Chen, Zeyuan Li, Dr. Jiacheng Xu, Wenzheng Zhang, Xin Zhao, Nathan Winemiller and many others for all the companionship and emotional supports throughout the past 6 years.

Last but not least, I want to thank my parents for always giving me the best opportunities on life and education. I want to thank my little sister who gives me a lot of inspirations and motivations. Without their support, I have no long way to come this far.

DEDICATION

to my sister and parents

Chapter 1

THEORETICAL BACKGROUND OF CONFIGURATION INTERACTION METHODS

In this dissertation, the following notations are used, unless otherwise specified:

- μ , ν , λ , σ: atomic orbitals (AOs)
- *p, q, r, s*: general molecular orbitals (MOs)
- *I, J, K, L*: Slater determinants

1.1 Non-relativistic and Relativistic Electronic Hamiltonian

The center question of quantum chemistry is to resolve the electronic structures in molecular systems and how they would response upon interactions with the surrounding environments. Conventionally without considering the relativistic effects and under Born-Oppenheimer Approximation (where nuclei are treated statically), the governing equation is the time-independent Schrödinger equation [142]:

$$\hat{H}_{\text{non-rel}}\Psi = E\Psi \tag{1.1}$$

The non-relativistic electronic Hamiltonian consists of three parts:

$$\hat{H}_{\text{non-rel}} = -\hat{T} - \hat{V}_{\text{nuc}} + \hat{V}_{\text{ee}} \tag{1.2}$$

where $\hat{T}$, $\hat{V}_{\text{nuc}}$ and $\hat{V}_{\text{ee}}$ are electronic kinetic energy, nuclear potential and electron-electron

repulsion operators respectively. They are defined as:

$$\hat{T} = \frac{1}{2}\sum_{i} \nabla_i \tag{1.3}$$

$$\hat{V}_{\text{nuc}} = \sum_{i} \frac{Z_A}{r_{iA}} \tag{1.4}$$

$$\hat{V}_{\text{ee}} = \frac{1}{2}\sum_{ij} \frac{1}{r_{ij}} \tag{1.5}$$

where i, j refer to electrons, A refers to nuclei, Z is nuclear charge and r is the distance between electron and electron/nuclear positions.

When special relativity is considered with the time-independent Schrödinger equation, the Dirac equation is derived in four-component picture where the one-electron wavefunction is expressed in the four-spinor form:

$$\phi = \begin{pmatrix} \psi^L \\ \psi^S \end{pmatrix} \tag{1.6}$$

where ψ^L and ψ^S are two-spinors of the large and small components consisting α and β part:

$$\psi^L = \begin{pmatrix} \psi^L_\alpha \\ \psi^L_\beta \end{pmatrix}, \; \psi^S = \begin{pmatrix} \psi^S_\alpha \\ \psi^S_\beta \end{pmatrix} \tag{1.7}$$

Then, the Dirac equation can be written as [141]

$$\hat{H}^{\text{4C}}_{\text{rel}} \begin{pmatrix} \psi^L \\ \psi^S \end{pmatrix} = E \begin{pmatrix} \psi^L \\ \psi^S \end{pmatrix} \tag{1.8}$$

and the four-component relativistic Hamiltonian in matrix form then is:

$$\hat{H}^{\text{4C}}_{\text{rel}} = \begin{pmatrix} \mathbf{I} \otimes V & c\boldsymbol{\sigma} \cdot \mathbf{p} \\ c\boldsymbol{\sigma} \cdot \mathbf{p} & \mathbf{I} \otimes (V - 2mc^2) \end{pmatrix} \tag{1.9}$$

where $\mathbf{p} = -i\boldsymbol{\nabla}$ is the momentum operator and $\boldsymbol{\sigma}$ are Pauli matrices.

$$\mathbf{I} = \begin{pmatrix} 1 & 0 \\ 0 & 1 \end{pmatrix}, \boldsymbol{\sigma}_x = \begin{pmatrix} 0 & 1 \\ 1 & 0 \end{pmatrix}, \boldsymbol{\sigma}_y = \begin{pmatrix} 0 & -i \\ i & 0 \end{pmatrix}, \boldsymbol{\sigma}_z = \begin{pmatrix} 1 & 0 \\ 0 & -1 \end{pmatrix}. \tag{1.10}$$

For the one-electron system, V is the nuclear potential that gives rise to scalar relativistic and spin-orbit effects. For many electron systems, the leading-order two-electron interactions that enter the molecular potential are described by the Coulomb and Gaunt terms:

$$V_{ee} = \sum_{i=1}^{N} \sum_{j>i} (g^C(i,j) - g^G(i,j)) \tag{1.11}$$

$$g^C(i,j) = \frac{1}{r_{ij}} \tag{1.12}$$

$$g^G(i,j) = \frac{\boldsymbol{\alpha}_i \cdot \boldsymbol{\alpha}_j}{r_{ij}} \tag{1.13}$$

where the components of the $\boldsymbol{\alpha}$ matrices are defined as

$$\alpha_{i,J} = \begin{pmatrix} \mathbf{0}_2 & \boldsymbol{\sigma}_J \\ \boldsymbol{\sigma}_J & \mathbf{0}_2 \end{pmatrix}, \quad J = \{x, y, z\} \tag{1.14}$$

where i is i-th electron.

Between the non-relativistic and four-component Hamiltonian, there are also two-component methods where only the large component of the wavefunction is used. Among those method, the most popular one is exact-two-component(X2C), where the small component is eliminated from a four-component wavefunction and "folded" into the large component through a unitary transformation $\mathcal{U}$. Meanwhile, the one-electron part of the four-component relativistic Hamiltonian $\hat{H}^{4C}_{rel}$ can be approximately block-diagonalized and decoupled to solutions corresponding to electrons and positrons, as $\mathbf{H}^+$ and $\mathbf{H}^-$, respectively. Since only electronic solutions are of interest, the no-pair approximation[140] can be invoked and this

two-component Hamiltonian $\mathbf{H}^+$ will be the X2C relativistic Hamiltonian $\hat{H}^{\mathrm{2c}}_{\mathrm{rel}}$.

$$\mathcal{U}\hat{H}^{\mathrm{4C}}_{\mathrm{rel}}\mathcal{U}^\dagger = \begin{pmatrix} \mathbf{H}^+ & \mathbf{0}_2 \\ \mathbf{0}_2 & \mathbf{H}^- \end{pmatrix}, \quad \hat{H}^{\mathrm{X2C}}_{\mathrm{rel}} = \mathbf{H}^+, \quad \mathcal{U}\begin{pmatrix} \psi^L \\ \psi^S \end{pmatrix} = \begin{pmatrix} \psi^{2c} \\ 0 \end{pmatrix} \tag{1.15}$$

To extend X2C method for many-electron systems, normally the bare Coulomb operator is used with other two-electron relativistic effects approximated into one-body terms. Common approaches include the use of an empirical factor (known as Boettger factor[15], to scale the one-electron spin-orbital terms or atomic mean-field field two-eletron integrals (AMFI) method. [134]

The derivation and implementation of multi-reference methods rely on the use of the second quantization, where all the operators in electronic Hamiltonian could be expressed in the form of one-electron or two-electron operators [142]:

$$\mathcal{O}_1 = \sum_{pq} h_{pq}\hat{E}_{pq} \tag{1.16}$$

$$\mathcal{O}_2 = \sum_{pqrs} g_{pqrs}\hat{e}_{pqrs} \tag{1.17}$$

where h_{pq} and g_{pqrs} are one-electron and two-electron integrals in MO basis, respectively; $\hat{E}_{pq}$ and $\hat{e}_{pqrs}$ are one-electron and two-electron excitation operator that could be written with creation and annihilation operators:

$$\hat{E}_{pq} = a_p^\dagger a_q, \qquad \hat{e}_{pqrs} = a_p^\dagger a_r^\dagger a_s a_q \tag{1.18}$$

And with the resolution of identity, the two-electron excitation can be further decompose as one-electron operators:

$$\hat{e}_{pqrs} = \hat{E}_{pq}\hat{E}_{rs} - \delta_{qr}\hat{E}_{ps} \tag{1.19}$$

Conventionally, for one-component non-relativistic Hamiltonian, molecular orbitals (MO) are defined just as the spatial parts, namely, the linear combination of atomic orbitals from basissets. As the results, MOs are up to doubly occupied and the creation/annihilation operators are defined on each spin type as:

$$a_p^\dagger = a_{p\alpha}^\dagger + a_{p\beta}^\dagger, \qquad a_p = a_{p\alpha} + a_{p\beta} \tag{1.20}$$

However, in relativistic framework, because each molecular orbital is in spinor form as a linear combination of α and β parts (as Eq. (1.7)), they become at most singly occupied and the spin type is omit from the creation/annihilation operators.

1.2 Hartree Fock and Slater Determinants

To obtain the molecular orbitals, *i.e.*, the one-electron wavefunctions, Hartree-Fock (HF) method is proposed where the many-body electron motion are decoupled and electron-electron interactions are treated in a mean field. The N-electron HF wavefunction is normally constructed in the forms of a single Slater determinant:

$$|\Psi_{\mathrm{HF}}\rangle = \frac{1}{\sqrt{N}} \begin{vmatrix} \phi_i(1) & \phi_j(1) & \cdots & \phi_k(1) \\ \phi_i(2) & \phi_j(2) & \cdots & \phi_k(2) \\ \vdots & \vdots & \ddots & \vdots \\ \phi_i(N) & \phi_j(N) & \cdots & \phi_k(N) \end{vmatrix} \tag{1.21}$$

Where the $\{\phi_i\}$ are spin-adapted molecular orbitals. Then the Schrödinger or Dirac equations could be reduced in the following form:

$$\hat{F}(1)\phi_i(1) = \epsilon_i \phi_i(1) \tag{1.22}$$

Where the Fock operator is:

$$\hat{F}(1) = \hat{h}(1) + \sum_{i=1}^{N} \left(f_c \hat{J}_i(1) - \hat{K}_i(1) \right) \tag{1.23}$$

Where the f_c is the component factor derived by whether the orbital is singly or doubly occupied ($f_c = 1$ for two- or four-component Hamiltonian and $f_c = 2$ for one-component Hamiltonian). The $\hat{h}(1)$, $\hat{J}_i(1)$, $\hat{K}_i(1)$ are one-electron core Hamiltonian operator, Coulomb operator, and exchange operator, respectively and they can be evaluated as integrals in Eqs. (1.16) and (1.17)

$$\langle \phi_p | \, \hat{h}(1) \, | \phi_q \rangle = h_{pq} \tag{1.24}$$

$$\langle \phi_p | \, \hat{J}_i(1) \, | \phi_q \rangle = g_{pqii} \tag{1.25}$$

$$\langle \phi_p | \, \hat{K}_i(1) \, | \phi_q \rangle = g_{piiq} \tag{1.26}$$

1.3 Electronic Correlations and Configuration Interactions

From Sec. 1.2, we are able to obtain the molecular orbital pictures where the electron motions are isolated as the result of the mean-field treatment. However in reality, for a many-body electron system, the electronic structures are rather reflections of collective motions. Thus accurate descriptions must take the missing electron correlation into account. A simple approach to perform correlated computation is to construct the N-electron wavefunction using configuration expansion instead of a single Slater determinant:

$$|\Phi_{\mathrm{CI}}\rangle = C_{\mathrm{HF}} \, |\Psi_{\mathrm{HF}}\rangle + \sum_{ia} C_i^a \, |\Psi_i^a\rangle + \sum_{ijab} C_{ij}^{ab} \, \left|\Psi_{ij}^{ab}\right\rangle + \cdots \tag{1.27}$$

Where, as illustrated in Fig. 1.1, $|\Psi_i^a\rangle$ is a singly excited configuration where an electron in an occupied orbital ϕ_i is excited to a virtual orbital ϕ_a. Similarly, $\left|\Psi_{ij}^{ab}\right\rangle$ is a doubly excited configuration where two electrons in orbital ϕ_i and ϕ_j are excited to two virtual orbitals ϕ_a and ϕ_b, so on and so forth. Particularly, including all the possible excited determinants give

us the full configuration interaction (FCI) methods [79], which could explicitly correlated all the electrons.

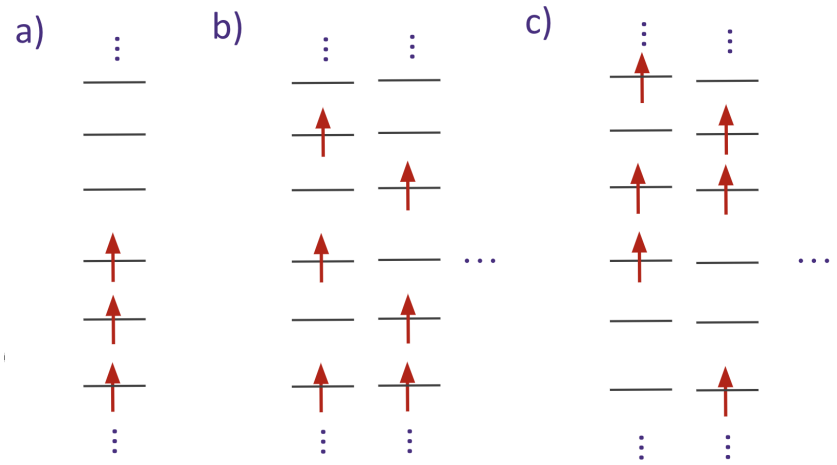

Figure 1.1. Relativistic electronic configuration expansions in diagrams, where each horizontal line represents a molecular orbitals (ordered by orbital energies), and a red arrow represents an electron. a) The HF configuration, b) singly excited electron configuration, c) doubly excited electron configuration.

The electron correlation for configuration interactions is simply defined as:

$$E_{\text{corr}} = E_{\text{CI}} - E_{\text{HF}} \tag{1.28}$$

The FCI will give the theoretical limit of the correlation energy ($E_{\text{corr}}^{FCI} = E_{\text{FCI}} - E_{\text{HF}}$) for a chosen electronic Hamiltonian and a set of atomic basis. However, the factorial scaling of the FCI method will make it impossible to be applied into any molecular systems with more than a few electrons. Thus, the most common practice for CI is to truncate the configuration expansion by excitation levels. Because of the Slater rule, normally, only singly and doubly excited configurations are included to form the single reference (SR) configuration interaction singles and doubles (CISD). The major challenge of this truncation is that it introduces imbalanced descriptions for system with near degenerate ground states. Since the near degenerate ground states can not be qualitatively describe by a single Slater deter-

minant, some of the important determinants are grouped at least in the category of singly excited configurations. Thus, to include the same single and double excited configurations, it would require at lease some of the triple or even higher excitation level of configurations corresponding to the HF configurations. Thus, a two-step treatment is often used to treat the static and dynamic correlations [98] separately as Secs. 1.4 and 1.5.

1.4 Complete-Active-Space Self-Consistent-Field (CASSCF)

The CAS wavefunction is constructed as the full configuration interaction (CI) expansion of Slater determinants $|K\rangle$, within selected active molecular orbitals:

$$|\Psi_{\mathrm{CAS}}\rangle = \sum_{K}^{N_{\mathrm{det}}^{\mathrm{CAS}}} C_K \, |K\rangle \tag{1.29}$$

where $N_{\mathrm{det}}^{\mathrm{CAS}}$ is total number of determinants in the expansion. In one-component method, $N_{\mathrm{det}}^{\mathrm{CAS}}$ can be computed as $\binom{N_{\mathrm{spatial}}}{n_\alpha}\binom{N_{\mathrm{spatial}}}{n_\beta}$, where n_α and n_β are number of α and β electrons and N_{spatial} is number of spatial orbitals in the CAS. However, for relativistic two-component or four-component methods under no-pair approximations, $N_{\mathrm{det}}^{\mathrm{CAS}}$ will be $\binom{N_{\mathrm{spinor}}}{n_e}$, where n_e is total number of electrons and N_{spinor} is total number of electronic spinor in CAS.

Other than the active space orbitals, there are remaining inactive core and virtual orbitals where they remains fully occupied and empty during a CASSCF calculations. In this section, the inactive core orbitals is indexed as $\{i, j, k, l\}$, the CAS orbitals is indexed as $\{t, u, v, w\}$ and the virtual orbitals is indexed as $\{a, b, c, d\}$. The energy of the CAS wavefunction then can be expressed as:

$$E^{\mathrm{CAS}} = \epsilon^{\mathrm{core}} + \langle \Psi_{\mathrm{CAS}} | \, \hat{H}^{\mathrm{CAS}} \, | \Psi_{\mathrm{CAS}} \rangle \tag{1.30}$$

where ϵ^{core} is the inactive core energies:

$$\epsilon^{\mathrm{core}} = \sum_i h_{ii} + \frac{1}{2} \sum_{ij} (f_c \, g_{iijj} - g_{ijji}) \tag{1.31}$$

and the $\hat{H}^{\mathrm{CAS}}$ is the active space Hamiltonian:

$$\hat{H}^{\mathrm{CAS}} = \sum_{tu} h_{tu}^{\mathrm{core}} \hat{E}_{tu} + \frac{1}{2} \sum_{tuvw} g_{tuvw} \hat{e}_{tuvw} \tag{1.32}$$

where h_{tu}^{core} is defined as the sum of one-electron interactions in CAS space and two-electron interaction between CAS electrons and inactive core electrons:

$$h_{tu}^{\mathrm{core}} = h_{tu} + \sum_{i} (g_{tuii} - g_{tiiu}) \tag{1.33}$$

The CASCI approach is formulated as the an eigenvalue problem $\boldsymbol{H}^{\mathrm{CAS}}\boldsymbol{C} = E\boldsymbol{C}$ such that energy expression Eq. (1.30) are minimized respect to CI coefficient $\boldsymbol{C}$. However, since only the active space orbitals are correlated, CASCI energies is not invariant to orbital optimization. The CASSCF method on the other hand optimize the wavefunction by making the energy stationary with respect to variations of both CI coefficients and MO coefficients. Typically, orbital optimization is performed after solving the CASCI problem, and an exponential parametrization is applied to CAS wavefunction as:

$$|\Psi'_{\mathrm{CAS}}\rangle = \exp(\boldsymbol{X}) \, |\Psi_{\mathrm{CAS}}\rangle \tag{1.34}$$

where the variational matrix $\boldsymbol{X}$ is formulated as an anti-Hermitian matrix over all MOs ($X_{pq} = -X_{qp}^{*}$) to construct an unitary matrix $\boldsymbol{R} = \exp(\boldsymbol{X})$. Then the molecular orbital could be rotate via unitary transformation of the existing orbitals:

$$\psi'_p = \sum_q R_{pq} \psi_q \tag{1.35}$$

The CASSCF wave function is then optimized when:

$$\frac{\partial E}{\partial \boldsymbol{C}} = 0; \qquad \frac{\partial E}{\partial \boldsymbol{X}} = 0; \tag{1.36}$$

The detailed of orbital optimization could be found in Ref [63]. And note that orbital optimization could be performed not only for one CAS states, but also for a few states using state-averaging (SA) active space electron density. As the result, the ground state and excited states arising from CAS space could be treated in equal footing.

1.5 Multi-Reference Configuration Interactions (MRCI)

The MRCI method normally utilize the CASSCF wavefunctions as the reference and perform additional CI expansion to correlate the selected inactive core and virtual orbitals. For example, the relativistic MO space could be partition in five sub-spaces as Fig. 1.2:

- *Frozen Core Space* consists of MOs that are occupied in all reference determinants and remain occupied in MRCI.
- *Correlated Core Space* consists of MOs that are occupied in all reference determinants but can be excited in MRCI.
- *Complete Active Space* consists of active MOs in the CASSCF reference.
- *Correlated Virtual Space* consists of MOs that are unoccupied in all reference determinants but can be occupied in MRCI.
- *Frozen Virtual Space* consists of MOs that are unoccupied in all reference determinants and remain unoccupied in MRCI.

This convenient space partition scheme can further map the MRCI framework to a restricted or generalized active space framework with computational advantages, which will be discussed in Sec. 3.2.2. In MRCI framework, the indices of $\{i, j, k, l\}$, $\{t, u, v, w\}$ and $\{a, b, c, d\}$ are adjusted accordingly for the frozen core space, correlated space and frozen virtual space, respectively. Then using the index of $\{t_i, v_j, ...\}$ and $\{u_a, w_b, ...\}$ for occupied and unoccupied orbitals within the correlated space, we can obtain the MRCI wavefunction ansatz as:

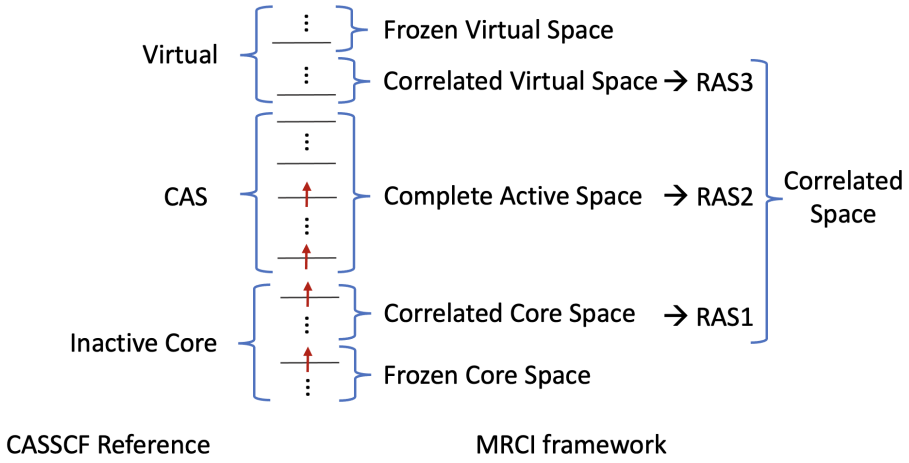

Figure 1.2. Molecular orbital space partitioning in relativistc MRCI framework using RAS concept.

$$|\Psi_{\mathrm{MRCI}}\rangle = \sum_{K}^{N_{\mathrm{det}}^{\mathrm{CAS}}} C_K |K\rangle + \sum_{t_i,u_a} \sum_{K}^{N_{\mathrm{det}}^{\mathrm{CAS}}} C_{K_{t_i}^{u_a}} \left|K_{t_i}^{u_a}\right\rangle + \sum_{t_i v_j, u_a w_b} \sum_{K}^{N_{\mathrm{det}}^{\mathrm{CAS}}} C_{K_{t_i v_j}^{u_a w_b}} \left|K_{t_i v_j}^{u_a w_b}\right\rangle + \cdots \quad (1.37)$$

where $\left|K_{t_i}^{u_a}\right\rangle$ and $\left|K_{t_i v_j}^{u_a w_b}\right\rangle$ are the singly-excited and doubly-excited electron configurations generated from a given reference determinant $|K\rangle$ by applying the excitation operators:

$$\left|K_{t_i}^{u_a}\right\rangle = \hat{E}_{u_a t_i} |K\rangle ; \quad \left|K_{t_i v_j}^{u_a w_b}\right\rangle = \hat{e}_{u_a t_i w_b v_j} |K\rangle \quad (1.38)$$

where the excitation operators are defined in Eq. (1.18)

Although MRCI are very similar as RASCI, the key difference between them however is the purpose of the calculations. RASCI is mainly an approximation to CASCI and is used to capture the static correlations, thus it's normally used along with orbital optimizations (similar in Sec. 1.4), *i.e.* as the RASSCF method; the MRCI methods however are used for accurate description of dynamic correlations and no orbital optimization is needed afterwards. This difference is also reflected on the number of correlated virtual orbitals. As the results,

in RASCI, only limited virtual orbitals are correlated, while in MRCI, virtual orbitals are included as many as the computational resources could afford.

The energy expression of MRCI will the same as Eq. (1.30) with the index range adjustment and the substitution of CAS wavefunction ansatz to MRCI wavefunction. The first term in Eq. (1.37) contains the configurations present in the CASSCF reference wave function. These configurations capture *static* correlation, to give a qualitatively correct wave function. The remaining terms include excited configurations that serve to capture the *dynamic* correlation, essential for quantitatively accurate energies and properties.

The total number of unique determinants in the relativistic MRCI framework is

$$N_{\mathrm{det}}^{\mathrm{MRCI}} = \sum_{i_{\mathrm{h}}=0}^{m_{\mathrm{h}}} \sum_{i_{\mathrm{e}}=0}^{m_{\mathrm{e}}} \binom{N_{\mathrm{RAS1}}}{i_{\mathrm{h}}} \binom{N_{\mathrm{RAS2}}}{n_{\mathrm{e}} - N_{\mathrm{RAS1}} + i_{\mathrm{h}} - i_{\mathrm{e}}} \binom{N_{\mathrm{RAS3}}}{i_{\mathrm{e}}} \tag{1.39}$$

where N_{RAS1}, N_{RAS2}, N_{RAS3} are the numbers of orbitals in RAS1, RAS2/CAS, RAS3 spaces according to Fig. 1.2, n_{e} is the total number of electrons in the correlated space, and m_{h} and m_{e} are maximum number of holes in RAS1 and maximum number of electrons in RAS3. For MRCISD, the total number of unique determinants scales factorially with N_{RAS2} and quadratically with both N_{RAS1} and N_{RAS3}.

For non-relativistic framework, the total number of unique determinants could computed similiarly as:

$$N_{\mathrm{det}}^{\mathrm{MRCI}} = \sum_{i_{\mathrm{h}}^{\alpha}=0}^{m_{\mathrm{h}}} \sum_{i_{\mathrm{h}}^{\beta}=0}^{m_{\mathrm{h}}-i_{\mathrm{h}}^{\alpha}} \sum_{i_{\mathrm{e}}^{\alpha}=0}^{m_{\mathrm{e}}} \sum_{i_{\mathrm{e}}^{\beta}=0}^{m_{\mathrm{e}}-i_{\mathrm{e}}^{\alpha}} \prod_{\sigma=\alpha,\beta} \binom{N_{\mathrm{RAS1}}}{i_{\mathrm{h}}^{\sigma}} \binom{N_{\mathrm{RAS2}}}{n_{\mathrm{e}}^{\sigma} - N_{\mathrm{RAS1}} + i_{\mathrm{h}}^{\sigma} - i_{\mathrm{e}}^{\sigma}} \binom{N_{\mathrm{RAS3}}}{i_{\mathrm{e}}^{\sigma}} \tag{1.40}$$

where n_{e}^{α} and n_{e}^{β} are the total number of α and β electrons in the correlated space, respectively.

Chapter 2

A BRIEF REVIEW OF EXISTING EFFICIENT CI IMPLEMENTATIONS

Despite of the simple formalism of CI methods and full CI as the theoretical limit for electron correlations, their applications have been limited to small and modest-size of the molecular systems. The primary reason behind this limitation is due to the fast scaling of parameter numbers needed by the CI methods to obtain accurate descriptions of the chemical systems. Let alone that the number of determinants in FCI scales exponentially as the increase of the number of electrons and orbitals, the number of determinants in common MRCISD calculations scales quadratically as increase of the number of correlated core and virtual orbitals (see Eq. (1.39) and Eq. (1.40)). Benefit from the rapid advances of modern computer hardware and the algorithm developments for solving CI problem, nowadays the limit of the CAS/RASCI calculation exceeds tens of billions (10^{10}) determinants and the limit of MRCI also increases above billion (10^9) range. In this section, I will briefly review the critical algorithms and technologies that enable the large-scale CI calculations.

2.1 Overview

In the past two decades, researchers in the field of the quantum chemistry have been exploring and pushing the limits of CI methods. Among all the efforts, the LUCIA [107] and the relativistic version LUCIAREL [42, 43, 40] developed by Olsen *et. al.* has the most influence in the field of solving CI problems. As early as 1990, Olsen *et. al.* [108] successfully demonstrated a non-relativistic FCI calculation on Mg atom that has more than 1 billion determinants. Later on, they reported large non-relativistic FCI calculations with about 20 billion determinants on the CN anion in cc-pVDZ basis[145]. The limit of non-relativistic

FCI/CASCI is further pushed in 2017 by an attempted calculation on a linear Cr_3 system by Olsen, Laura and *et. al.* [149]. They tested their algorithm on thousands of processors for days to solve a CI problem with near 1 trillion (10^{12}) determinants. For MRCI calculations, Knecht *et. al.* optimized and paralleled LUCIA and LUCITAREL with applying the generalized active space (GAS) concepts. They reported an non-relativistic MRCISD calculations on H_2O grond state with 1.5 billion determinants in 2007 [74], and a relativistic MRCISD calculations on bismuth monohydride (BiH) with 0.4 billion determinants in 2009[75]. Outside of the efforts from LUCIA/LUCIAREL researchers, non-relativistic CAS/RASCI algorithms are mainly focused. Rossi *et. al.* performed a CI calculation with 9.6 billion determinants on N_2 molecule in 1999 [128] and Gan *et. al.* reported to use a highly vectorized algorithm to solve a FCI problem with about 65 billion determinants on C_2 in cc-pVTZ basis [45]. More interestingly, Todd *et. al.* investigated CI algorithms with GPU accelerators to solve a non-relativistic CASCI with 2.4 billion determinants on Ethylene Dimer [35].

2.2 The Iterative Davidson Methods

To solve the eigenvalue problem of CASCI or MRCI, the straightforward way is to build a full Hamiltonian matrix and diagonalize it. The matrix element could be computed as:

$$H_{KL} = \langle K| \hat{H} |L\rangle , \qquad \{|K\rangle , |L\rangle\} \in \Psi_{\text{CAS}} \text{ or } \Psi_{\text{MRCI}} \tag{2.1}$$

However, the rapid scaled dimension in MRCI expansion (Eq. (1.39) & Eq. (1.40)) usually prevents direct diagonalization of the MRCI eigenvalue problem. On the other hand, for the interest of the chemical problem, primarily only the ground states and lowest excited states or excited states at certain energy range (in resolving the X-Ray spectra) are desired. Thus, the iterative Davidson method [19] is widely used to solve the eigenvalue problems in the field of computational quantum chemistry.

The typical Davidson procedure for solving n states in N dimension starts with m initial orthonormal guess vectors to form subspace basis $\boldsymbol{C}^{\text{sub}}$ with dimension $N \times m$. In each

micro-iteration, a subspace eigenvalue problem will be formed and solved; the results are improved by expanding basis with perturbed vectors until certain convergence criteria are met. Typically, the following steps are taken in each micro-iteration:

- Form matrix-vector product vectors ($\boldsymbol{\sigma}$) using the sub-space vectors from guess or last iteration, as:

$$\sigma_K = \sum_L H_{KL} C_L \tag{2.2}$$

  specifically, in second quantization form, the CI sigma formation could be expressed as:

$$\sigma_K = \sum_{pq} \sum_L h_{pq}^{\text{core}} \langle K| \hat{E}_{pq} |L\rangle C_L + \frac{1}{2} \sum_{pqrs} \sum_L g_{pqrs} \langle K| \hat{e}_{pqrs} |L\rangle C_L \tag{2.3}$$

  where h_{pq}^{core} and g_{pqrs} and one-electron and two-electron interactions arising from the chosen Hamiltonian; $\langle K| \hat{E}_{pq} |L\rangle$ and $\langle K| \hat{e}_{pqrs} |L\rangle C_L$ are symbolic matrix elements.

- Form subspace problem as $\boldsymbol{H}^{\text{sub}} = \boldsymbol{C}^{\text{sub}\dagger}\boldsymbol{\sigma}$ with a dimension of $m \times m$ and diagonalize it to obtain the subspace eigenvalues $\boldsymbol{E}$ and eigenvectors $\boldsymbol{X}$. The n states with lowest energies are of interest and the corresponding full space vectors then are easily obtained as $\boldsymbol{C}_{N\times n} = \boldsymbol{C}^{\text{sub}}_{N\times m}\boldsymbol{X}_{m\times n}$.

- Compute the residue of each full space vector and its 2-norm as:

$$\boldsymbol{r}_i = \boldsymbol{H}^{\text{sub}}\boldsymbol{X}_i - E_i\boldsymbol{C}_i \tag{2.4}$$

$$|\boldsymbol{r}_i| = \sqrt{\sum_K [\boldsymbol{r}_i(K)]^2} \tag{2.5}$$

  if the 2-norm $|\boldsymbol{r}_i|$ is smaller than the convergence threshold ϵ_{r}, a vector is considered as converged. When all the desired vector are converged, end the Davidson procedure and return the current $\{\boldsymbol{E}, \boldsymbol{C}\}$ as the full space eigenvalues and eigenvectors.

- For unconvereged full space vectors, new perturbed vectors $\{\boldsymbol{Q}_i\}$ to the subspace basis

$\boldsymbol{C}^{\text{sub}}$:

$$\boldsymbol{C}^{\text{sub}'} = \begin{bmatrix} \boldsymbol{C}^{\text{sub}} & \boldsymbol{Q} \end{bmatrix} \tag{2.6}$$

where each of the perturbed vectors are obtained from the residues:

$$\boldsymbol{Q}_i(K) = \frac{\boldsymbol{r}_i(K)}{E_i - H_{KK}} \tag{2.7}$$

where H_{KK} is the full space Hamiltonian diagonal matrix element.

For X-Ray spectra calculations, energy specific approach is adapted [111], where states above a certain threshold (ϵ_t) from the ground state in each step are solved simultaneously. With the majority of the steps same as the normal Davidson procedure, the energy-specific Davidson will pick additional n' high energy states with energy $|E_i - E_0| > \epsilon_t$, where E_0 is the energy of the ground state at the same iteration. During each interaction, the high energy states are also evaluated for convergence and perturbed vectors will be generated and append to the subspace vectors in a similar fashion.

2.3 The Sparsity Utilization in Electronic Hamiltonian

Fundamentally, the CI problems are sparse because only small amount of symbolic matrix terms (In Eq. (2.3)) will be non-zero (see more details in Sec. 3.1). The equation for one-electron and two-electron symbolic matrix are expressed as:

$$\begin{matrix} \langle K| \hat{E}_{pq} |L\rangle \\ (\text{or } \langle K| \hat{e}_{pqrs} |L\rangle) \end{matrix} = \begin{cases} \pm 1, & \text{when } |K\rangle = \pm \hat{E}_{pq} |L\rangle \, (\pm \hat{e}_{pqrs} |L\rangle) \\ 0, & \text{otherwise} \end{cases} \tag{2.8}$$

Conventionally, the information of non-zero elements of $\langle K| \hat{E}_{tu} |L\rangle$ ($\{K, L, t, u, \langle K| \hat{E}_{tu} |L\rangle\}$), *i.e.*, one-electron excitation lists are precomputed and stored in core. Thus, during sigma formation, sparse multiplications could be executed efficiently. To avoid the additional storage for $\langle K| \hat{e}_{tuwv} |L\rangle$, the two-electron excitation operator can be factorized into multiplications

of one-electron operators *via*

$$\hat{e}_{pqrs} = \hat{E}_{pq}\hat{E}_{rs} - \delta_{qr}\hat{E}_{ps} \tag{2.9}$$

As the result, the $\boldsymbol{\sigma}$ vector now has the form of:

$$\begin{aligned}\sigma_K =& \sum_{pq}\sum_{L} h_{pq}^{\text{core}} \langle K| \hat{E}_{pq} |L\rangle C_L + \frac{1}{2}\sum_{pqrs} g_{pqrs}\delta_{qr} \langle K| \hat{E}_{ps} |L\rangle C_L \\ &+ \frac{1}{2}\sum_{pqrs}\sum_{L} g_{pqrs} \langle K| \hat{E}_{pq}\hat{E}_{rs} |L\rangle C_L \qquad (2.10)\\ =& \sum_{pq}\sum_{L} h'_{pq} \langle K| \hat{E}_{pq} |L\rangle C_L + \frac{1}{2}\sum_{pqrs}\sum_{L}\sum_{J} g_{pqrs} \langle K| \hat{E}_{pq} |J\rangle \langle J| \hat{E}_{rs} |L\rangle C_L \qquad (2.11)\end{aligned}$$

where the h'_{pq} is defined as

$$h'_{pq} = h_{pq}^{\text{core}} - \frac{1}{2}\sum_{r} g_{prrq} \tag{2.12}$$

2.4 Knowles and Handy's String Methods

Normally, we can conveniently record a many-electron configuration with binary strings of zeros and ones, where zero and one represents the empty and occupied orbital respectively. For example, $|100101\rangle$ can be used for a determinant where orbital 1, 4 and 6 are occupied and orbital 2, 3 and 5 are empty. In order to avoid the explicit storage and sorting the configurations in CI problem, Knowles and Handy [79, 80] introduced the string methods based on Duch's [27] work on graphical representation of CI space. Conceptually, the string methods could be viewed as minimal perfect hash functions to map all the configurations into continuous integers (*i.e.* addresses) without any collision. In that way, all the coefficients in $\boldsymbol{C}$ and $\boldsymbol{\sigma}$ vectors are ordered as the result of the string methods, and integers of configurations are used for one excitation lists mentioned above.

The most common usage and easiest formation of string methods are within a fully expanded space, *i.e.*, complete active space (CAS). Typically, based on certain order (lexical or reverse-lexical), weights can be assigned to either unoccupied or occupied orbitals and

used for address computation. For example, weights of the occupied orbitals are used, the address is computed as:

$$A(K) = 1 + \sum_{i=1}^{n} Z(i,j) \tag{2.13}$$

where $Z(i,j)$ is the weight of the i^{th} electron occupying the j^{th} orbitals, and n is number of electrons in determinant $|K\rangle$. For instances, in the previous example, the address of $|100101\rangle$ is computed as:

$$A(100101) = 1 + Z(1,1) + Z(2,4) + Z(3,6) \tag{2.14}$$

The weights could be deducted from from the original graphical representation method (more details in [79, 80]). In our implementation, we adopted the reverse-lexical order with the weights formula:

$$Z(i,j) = \begin{cases} \sum\limits_{k=i-1}^{j-1} \binom{k}{i-1}, & \text{if } n-i \leq m-j \\ 0, & \text{otherwise} \end{cases} \tag{2.15}$$

where m is the number of orbitals. A recursive relation can be used to easily construct the weights array $\boldsymbol{Z}$:

$$Z(i,j) = \begin{cases} Z(i,j-1) + \binom{j-1}{i-1}, & \text{if } n-i \leq m-j \text{ and } j > 1 \\ 0, & \text{otherwise} \end{cases} \tag{2.16}$$

2.5 Fast Algorithms for Non-relativistic CASCI Sigma Formation

As described in Sec. 2.1, the majority of research were conducted for non-relativistic CASCI or FCI problems. The natrual separation of the electronic spins (α and β manifolds) and complete expansion within a space enable the CI problems to be easily formulated into matrix-matrix multiplication form. Specifically, each configuration and excitation operator

could be express as combination of the α and β parts:

$$|K\rangle = |K_\alpha K_\beta\rangle \tag{2.17}$$

$$\hat{E}_{pq} = \hat{E}^\alpha_{pq} + \hat{E}^\beta_{pq} \tag{2.18}$$

Naturally, each CI vector and sigma could be reshape into a matrix:

$$\boldsymbol{C}(K) \to \boldsymbol{C}(K_\alpha, K_\beta), \qquad \boldsymbol{\sigma}(K) \to \boldsymbol{\sigma}(K_\alpha, K_\beta) \tag{2.19}$$

and the one-electron symbolic matrix element could be simplify as:

$$\langle K| \hat{E}^\alpha_{pq} |L\rangle = \langle K_\alpha K_\beta| \hat{E}^\alpha_{pq} |L_\alpha L_\beta\rangle = \langle K_\alpha| \hat{E}^\alpha_{pq} |L_\alpha\rangle \delta_{K_\beta L_\beta} \tag{2.20}$$

$$\langle K| \hat{E}^\beta_{pq} |L\rangle = \langle K_\alpha K_\beta| \hat{E}^\beta_{pq} |L_\alpha L_\beta\rangle = \langle K_\beta| \hat{E}^\beta_{pq} |L_\beta\rangle \delta_{K_\alpha L_\alpha} \tag{2.21}$$

Plug in the above separation formalism, the 1e and 2e parts of the Sec. 3.2.4 could be re-written as:

$$\begin{aligned} {}^{1e}\sigma(K_\alpha, K_\beta) = &\sum_{pq} \sum_{L_\alpha} h'_{pq} \langle K_\alpha| \hat{E}^\alpha_{pq} |L_\alpha\rangle C(L_\alpha, K_\beta) \\ &+ \sum_{pq} \sum_{L_\beta} h'_{pq} \langle K_\beta| \hat{E}^\beta_{pq} |L_\beta\rangle C(K_\alpha, L_\beta) \end{aligned} \tag{2.22}$$

$$\begin{aligned} {}^{2e}\sigma(K_\alpha, K_\beta) = &\frac{1}{2} \sum_{pqrs} \sum_{L_\alpha} \sum_{J_\alpha} g_{pqrs} \langle K_\alpha| \hat{E}^\alpha_{pq} |J_\alpha\rangle \langle J_\alpha| \hat{E}^\alpha_{rs} |L_\alpha\rangle C(L_\alpha, K_\beta) \\ &+ \frac{1}{2} \sum_{pqrs} \sum_{L_\beta} \sum_{J_\beta} g_{pqrs} \langle K_\beta| \hat{E}^\beta_{pq} |J_\beta\rangle \langle J_\beta| \hat{E}^\beta_{rs} |L_\beta\rangle C(K_\alpha, L_\beta) \\ &+ \frac{1}{2} \sum_{pqrs} \sum_{L_\alpha} \sum_{L_\beta} g_{pqrs} \langle K_\alpha| \hat{E}^\alpha_{pq} |L_\alpha\rangle \langle K_\beta| \hat{E}^\beta_{rs} |L_\beta\rangle C(L_\alpha, L_\beta) \\ &+ \frac{1}{2} \sum_{pqrs} \sum_{L_\alpha} \sum_{L_\beta} g_{pqrs} \langle K_\beta| \hat{E}^\beta_{pq} |L_\beta\rangle \langle K_\alpha| \hat{E}^\alpha_{rs} |L_\alpha\rangle C(L_\alpha, L_\beta) \end{aligned} \tag{2.23}$$

For two-electron part of sigma where most of the computation time is spent, different contraction orders have been implemented and studied. For simplicity, here we only give the equation for the first term of Eq. (2.23), and the remaining terms can be deduced similarly.

2.5.1 The Knowles-Handy Method

The Knowles-Handy Method [79, 80] was an extension of Siegbahn's sigma formation [133] with configuration state function (CSF) to determinant basis. The first term in Eq. (2.23) are contracted in the following order:

$$\Omega^{rs}(J_\alpha, J_\beta) = \sum_{L_\alpha, L_\beta} \langle J_\alpha | \hat{E}^\alpha_{rs} | L_\alpha \rangle C(L_\alpha, L_\beta) \delta_{L_\beta J_\beta} \tag{2.24}$$

$$\Lambda^{pq}(J_\alpha, J_\beta) = \sum_{rs} g_{pqrs} \Omega^{rs}(J_\alpha, J_\beta) \tag{2.25}$$

$${}^{2e}\sigma(K_\alpha, K_\beta) += \frac{1}{2} \sum_{pq, J_\alpha, J_\beta} \Lambda^{pq}(J_\alpha, J_\beta) \langle K_\alpha | \hat{E}^\alpha_{pq} | J_\alpha \rangle \delta_{K_\beta J_\beta} \tag{2.26}$$

Where Ω and Λ are intermediates and the step Eq. (2.25) is conducted in matrix-matrix multiplication way.

2.5.2 The Olsen-Roos Method

Another important matrix multiplication method is reported by Olsen and Roos *et.al.*, [109] similarly, the first term in Eq. (2.23) are now contracted in the following order:

$$\Omega^{rs}(J_\alpha, J_\beta) = \sum_{L_\alpha, L_\beta} \langle J_\alpha | \hat{E}^\alpha_{rs} | L_\alpha \rangle C(L_\alpha, L_\beta) \delta_{L_\beta J_\beta} \tag{2.27}$$

$$X^{rs}(K_\alpha, J_\alpha) = \sum_{pq} g_{pqrs} \langle K_\alpha | \hat{E}^\alpha_{pq} | J_\alpha \rangle \tag{2.28}$$

$${}^{2e}\sigma(K_\alpha, K_\beta) += \sum_{rs, J_\alpha, J_\beta} \Omega^{rs}(J_\alpha, J_\beta) X^{rs}(K_\alpha, J_\alpha) \delta_{K_\beta J_\beta} \tag{2.29}$$

where the step Eq. (2.29) is conducted in matrix-matrix multiplication way.

2.5.3 The Frisch-Li Method

In 2011, Frisch and Li *et. al.* [92] also proposed another algorithm, where the first term in Eq. (2.23) are now contracted in the following order:

$$X^{pq}(J_\alpha, L_\alpha) = \sum_{rs} g_{pqrs} \langle J_\alpha | \hat{E}^\alpha_{rs} | L_\alpha \rangle \tag{2.30}$$

$$\Lambda^{pq}(J_\alpha, J_\beta) = \sum_{L_\alpha, L_\beta} X^{pq}(J_\alpha, L_\alpha) C(L_\alpha, L_\beta) \delta_{L_\beta J_\beta} \tag{2.31}$$

$${}^{2e}\sigma(K_\alpha, K_\beta) += \sum_{pq, J_\alpha, J_\beta} \Lambda^{pq}(J_\alpha, J_\beta) \langle K_\alpha | \hat{E}^\alpha_{pq} | J_\alpha \rangle \delta_{K_\beta J_\beta} \tag{2.32}$$

where the step Eq. (2.32) is conducted in matrix-matrix multiplication way.

Despite of the various efficient implementations been reported for non-relativistic CASCI, it is challenging to apply similar algorithm for relativistic MRCI calculations due to increased formalism complexity and memory bottlenecks for intermediate storage (see more detail in Sec. 3.1)

2.6 Distributed Implementation of CI using GAS framework

Because of the quickly scaling of MRCI problem, it rises demanding requirements for computational resources such as FLOPs, memory and disk storage beyond what a single machine could offer. Thus, in additional to ensuring computational efficiency on single machines, scalable algorithms are must to enable large-scale CI calculations. Olsen and Knecht *el. al.* [42, 43, 40, 74, 75] reported a generalized active space (GAS) approach for both large-scale non-relativistic and large-scale relativistic CI calculations. The essential idea of GAS is to generalize the CAS and RAS definitions and allow an arbitrary number of active spaces during CI expansion. Within each GAS, complete expansion will be performed but restrictions are normally enforced upon the maximum number of occupations in different GAS or the maximum excitation level between spaces. Because of this flexible trait of GAS, a large CI vectors could be easily divided into small segments and ready to distributed to different

computer nodes. Each segments has the same occupation types and point group symmetry for α/β strings in non-relativistic calculation or bar/unbar strings in relativistic calculations, *i.e.*, forms a TTSS block. To ensure load balancing between each computer node, their implementation utilized a static load balancing scheme and distributed the TTSS block based on the number of non-zero connections established between $\boldsymbol{\sigma}^{\mathrm{TTSS}_j}$ and $\boldsymbol{C}^{\mathrm{TTSS}_j}$. In Knecht *el. al.*'s 2009 work [75], they tested their distributed algorithm with a MRCI calculation with 428 million determinants and reported an near perfect scaling up to 16 processors in either a IBM AIX-power 6 cluster and a standard Linux cluster (with only using one out of four processors). However, the parallel performances were degraded when larger number of processors were used or/and multiple cores were used in Linux cluster. Speedup is only 2.58 times for 4 cores in one machine, and 48.42 times speedup is found for 128 processors, which could be translated into 18.78 times inter-node speedup for moving from 1 node to 32 nodes. Similar issue in Linux cluster was even more significant in a non-relativistic CI calculation with 4 billion determinants by Laura and Olsen *et. al.* in 2017. They reported only 6.3 times inter-node speedup when moving from 1 node to 16 nodes.

Chapter 3

AN EFFICIENT MRCI FORMATION AND ITS DISTRIBUTED IMPLEMENTATION

3.1 Challenges of Large-Scale Relativistic Multi-Reference Configuration Interactions

When it comes to implementations of CI methods in Kramer unrestricted relativistic region, some of the efficient approaches reviewed in Chapter 2 becomes challenging to adopt. The primary difference in Kramer unrestricted framework is that the every molecular orbitals are mixing of α and β components. As the result, the relativistic 2C/4C molecular orbitals are singly occupied and there is no natural separation of the $\{\phi_\alpha\}$ and $\{\phi_\beta\}$ manifolds. The direct implication of CI expansion within singly occupied molecular orbitals is that the number of determinants and the number of non-zero Hamiltonian matrix elements are much larger than the expansion in non-relativistic doubly occupied orbitals.

Table 3.1. The comparison of CASCI expansion in one-component (1C) non-relativistic and two-component/four-component (2C/4C) relativistic frameworks

# of correlated electrons	# of correlated orbitals		# of determinants	
	1C	2C/4C	1C	2C/4C
14	14	28	11,778,624	40,116,600
16	16	32	165,636,900	601,080,390
18	18	36	2,363,904,400	9,075,135,300
20	20	40	34,134,779,536	137,846,528,820
22	22	44	497,634,306,624	2,104,098,963,720

For example of the CASCI, Tab. 3.1 lists the number of determinants for correlating same amount of electrons and orbitals in non-relativistic and relativistic frameworks. The ratio of number of non-zero CI Hamiltonian matrix are also plotted in Fig. 3.1, which indicates

that relativistic CI calculations are computational more expensive than their non-relativistic analogs.

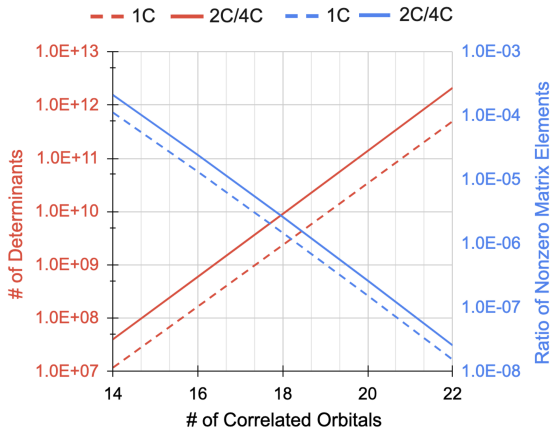

Figure 3.1. CASCI expansion in one-component (1C) non-relativistic and two-component/four-component (2C/4C) relativistic frameworks. Comparison is shown as the number of determinants and the ratio of nonzero Hamiltonian matrix elements for correlating the same number of electrons.

Table 3.2. Test MRCISD calculations with benzene. All the benchmarks here are using CAS(6, 12) as the reference with various correlated core and virtual orbitals.

Test Case	# of Correlated Cores	# of Correlated Virtuals	# of Determinants
benzene-8m	6	30	8,871,126
benzene-78m	6	90	78,176,076
benzene-311m	6	180	311,105,751
benzene-1.1b	12	180	1,155,126,588
benzene-4.4b	24	180	4,466,267,322
benzene-9.9b	36	180	9,941,540,136

Compared to CASCI calculations, MRCISD is even more challenging due to the less sparsity presented in the CI Hamiltonian matrix. To illustrate those challenges, here we presented a set of concrete examples of MRCISD calculation using benzene. As shown in Tab. 3.2, CAS(6, 12) is used for all the case. With the inclusion of different number of core and virtual orbitals for correlation calculation, the set of MRCISD calculations with determinants varying from 8 million to nearly 10 billion is obtained. We use the notation of

MR[N_c, CAS(6,12), Nv]-CISD with N_c number of core orbitals and Nv number of virtual orbitals. As shown inFig. 3.2, the ratio of nonzero matrix elements are investigated and compared against a few CASCI calculations with determinants in this range (10 million to 10 billion). Unlike that the CASCI problems get more sparse quickly as the increasing number of determinants, MRCISD remains similar sparsity even for very large problem. Specifically, for problems with about 10 billion determinatns, the sparsity of CAS(20,40)-CI goes to 99.99974% while the sparsity of MR[36, CAS(6,12), 180]-CISD remains only 99.85%.

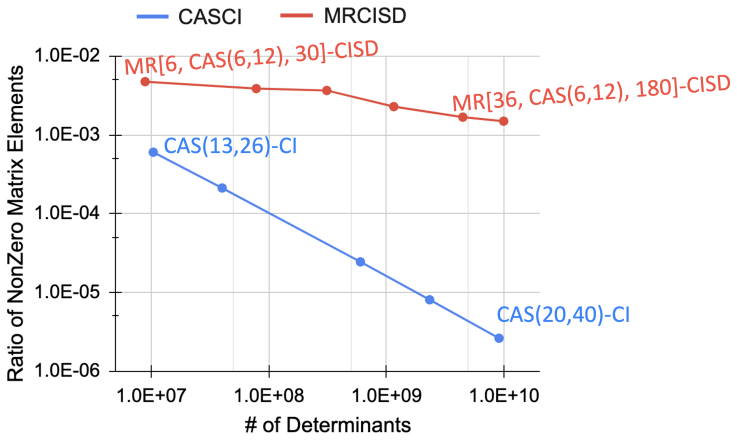

Figure 3.2. The ratio of nonzero Hamiltonian matrix elements in CASCI and MRCISD for calculations with similar number of determinants. All the MRCISD calculation here are using a CAS(6,12) as reference but with varying numbers of correlated core and virtual orbitals.

The computational challenge of MRCISD are analyzed in Fig. 3.3. With scaling the MRCISD problems from 10 million determinants to 10 billion, the required minimal FLOPs increases about 6 order. For the 10 billion test case, the storage of determinant coefficients $\boldsymbol{C}$ and their matrix-vector product $\boldsymbol{\sigma}$ requires 500 GB, and the storage for MO integrals needs about 50 GB. Most astonishingly, to utilize the sparsity discussed in Sec. 2.3, it costs about 10^6 GB to store the one-eletron excitation list naively as $\{K, L, t, u, \langle K|\, \hat{E}_{tu}\, |L\rangle\}$. While the challenges of minimal FLOPs, memory requirements for $\boldsymbol{C}$, $\boldsymbol{\sigma}$ and MO integrals could be mitigated by distributing the work to different machines, the one-electron excitation lists must be compressed for any large relativistic MRCI calculations. In the remaining of this

chapter, a novel relativistic CI formulation with its distributed implementation is introduced and the parallel performances are evaluated in Linux clusters.

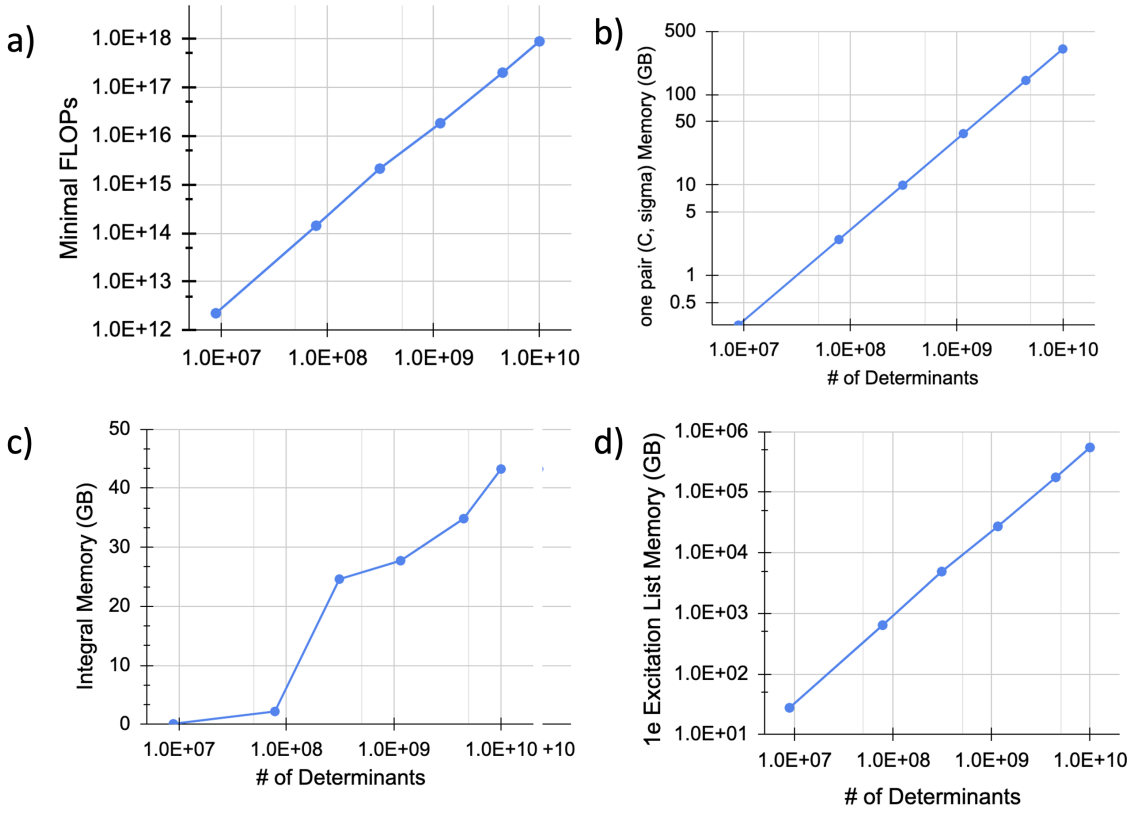

Figure 3.3. The computational challenges of MR[N_c, CAS(6,12), Nv]-CISD: a) minimal FLOPs required as the increase of number of determinants, b) memory required to store a pair of ($\boldsymbol{C}$ and $\boldsymbol{\sigma}$ as the increase of number of determinants, c) memory required to store a the full MO integrals as the increase of number of determinants, d) memory required to store the naive full one-electron excitation lists.

3.2 Distributed MRCI Sigma Formation and Implementation

The distributed MRCI sigma formation adopts the GAS concept for distribution of coefficient and computational work, and we developed efficient matrix-matrix multiplications with incorporation of the compressed one-electron excitation list. Note that with no symmetry of the MOs is considered in our implementation, we fully utilize the power of GAS for even

division of configurations to different computer nodes with better load balancing.

3.2.1 Definitions and Notations

In this chapter, the following definitions and notations are introduced:

- A generalized active space $\mathbb{X}_i \equiv \{\{\phi\}_i, n_i, \left|K^{\mathbb{X}_i}\right\rangle\}$ is defined by a unique set of orbitals $\{\phi\}_i$, an electron occupation number $n^{\mathbb{X}_i}$ in the space, and associated sub-determinants $\left|K^{\mathbb{X}_i}\right\rangle$. The number of orbitals in $\{\phi\}_i$ is noted as m_i and $\sum_i m_i = m_o$, where m_o is the total number of correlated orbitals. Similarly, $\sum_i n_i = n_e$ where n_e is the total number of correlated electrons. $\{\phi\} = \{\phi\}_1 \oplus \{\phi\}_2 \oplus ...$ where $\{\phi\}$ are all active orbitals.

- $\left|K^{\mathbb{X}_i}\right\rangle$ is a sub-determinant in active space $\mathbb{X}_i$ so that a full determinant $|K\rangle$ can be written as a sum of sub-determinants $|K\rangle = \left|K^{\mathbb{X}_1}\right\rangle \oplus \left|K^{\mathbb{X}_2}\right\rangle \oplus \cdots$ where $|K^{\mathbb{X}_1}\rangle \in \mathbb{X}_1$ and $|K^{\mathbb{X}_2}\rangle \in \mathbb{X}_2$.

- An electron configuration category $\mathcal{C}_i = \{\mathbb{X}_1^{\mathcal{C}_i}, \mathbb{X}_2^{\mathcal{C}_i}, ...\}$ is a unique set of active space configurations where electron occupation numbers in every GAS $\{n_j^{\mathcal{C}_i}\}$ are fixed. With this definition, the total determinant space could be divided into segments where each of them is a category. This is an analogous concept to the TTSS block in LUCIA/LUCIAREAL implementations.

- The total number of sub-determinants in a GAS of a category $\mathbb{X}_j^{\mathcal{C}_i}$ is noted as $N_j^{\mathcal{C}_i}$, and the total number of determinants for a category is noted as $N^{\mathcal{C}_i}$

- Categorical excitation operators are defined as the set of all excitation operators between active spaces:

$$\hat{\mathcal{E}}^{\mathbb{X}_p\mathbb{X}_q} = \left\{\hat{E}_{pq} : p \in \mathbb{X}_p, q \in \mathbb{X}_q\right\}$$
$$\hat{\mathcal{E}}^{\mathbb{X}_p\mathbb{X}_q\mathbb{X}_r\mathbb{X}_s} = \{\hat{e}_{pqrs} : p \in \mathbb{X}_p, q \in \mathbb{X}_q, r \in \mathbb{X}_r, s \in \mathbb{X}_s\}$$
$$\cdots$$

Thus, excited categories can be generated by applying categorical excitation operators on the reference electron configuration category $\mathcal{C}_0$.

3.2.2 Mapping Relativistic MRCI Vectors to Generalized Active Space (GAS) Framework

In order to organize the total space under the definition of GAS, a three-level addressing scheme is proposed as an extension to the Kozlowski and Pulay's RAS addressing scheme. The three levels of addresses refer to GAS address $A^{\mathbb{X}}$, categorical address $A^{\mathcal{C}}$ and the global address A^{g}.

In the first level, we focus on resolving the address of the sub-determinant $\left|K^{\mathbb{X}_i}\right\rangle$ in a GAS $\mathbb{X}_i$. And because of a complete expansion within GAS is always considered, the approach we used are identical to Knowles and Handy's addressing methods for CASCI as Eqs. (2.13) and (2.15).

Then in the second level, the address of the whole determinant is considered as a relative position within its category, *i.e.* categorical address. The whole category could be viewed as the tensor product of each GAS:

$$\left\{\left|K^{\mathcal{C}_i}\right\rangle\right\} = \left\{\left|K^{\mathbb{X}_1^{\mathcal{C}_i}}\right\rangle\right\} \otimes \left\{\left|K^{\mathbb{X}_2^{\mathcal{C}_i}}\right\rangle\right\} \otimes \cdots \tag{3.1}$$

Thus, the categorical address could be obtained by flattening the column-major tenor:

$$A^{\mathcal{C}}(K) = 1 + \sum_{j} \left[(A^{\mathbb{X}_j^{\mathcal{C}_i}}(K) - 1) \times \left(\prod_{k=1}^{j-1} N_k^{\mathcal{C}_i} \right) \right] \tag{3.2}$$

In the third level, the global address is determined. Since the whole space is divided into segments based on categories, the global address is easily obtained as:

$$A^{g}(K) = A^{\mathcal{C}}(K) + \sum_{k=0}^{i-1} N^{\mathcal{C}_k}, |K\rangle \in \mathcal{C}_i \tag{3.3}$$

Where the length of category could computed as the product of the the length of each GAS,

according to Sec. 3.2.4:

$$N^{\mathcal{C}_i} = \prod_j N_j^{\mathcal{C}_i} \tag{3.4}$$

$$N_j^{\mathcal{C}_i} = \binom{m_j^{\mathcal{C}_i}}{n_j^{\mathcal{C}_i}} \tag{3.5}$$

3.2.3 Compressed One Electron Excitation List

As shown in Fig. 3.3d, the quick scaling of the storage requirements of the naive one-electron excitation list prevents efficient utilization of the Hamiltonian sparsity in large relativistic MRCI calculations. Here we introduce a compressed one-electron excitation list by confining the excitation operator within one or two general active spaces: intra-GAS one-electron excitation list and inter-GAS one-electron excitation list. As suggested by the names, intra-GAS one-electron excitation list refers to that the excitations where p and q are in the same GAS, while inter-GAS one-electron excitation list refers to excitations where p and q are in different GASs.

For full space determinants, the elements of an one-electron excitation $\langle K| \hat{E}_{pq} |L\rangle$ contains 5 elements: $A^g(K)$, p, q, $A^g(L)$, $\langle K| \hat{E}_{pq} |L\rangle$. Here we only consider the case when $p < q$, the other cases could be deduced similarly. In order to form a nonzero element, the two determinants $|K\rangle$ and $|L\rangle$ must has the following occupation state:

$$|K\rangle = |b_1 \cdots b_{p-1} 1 \cdots b_{q-1} 0 \cdots b_n\rangle \tag{3.6}$$

$$|L\rangle = |b_1 \cdots b_{p-1} 0 \cdots b_{q-1} 1 \cdots b_n\rangle \tag{3.7}$$

Where the b_i is electron occupancy, and the value of 1 and 0 represents that the corresponding orbital is occupied or empty. Then, the non-zero one-electron symbolic matrix elements could

be easily computed as:

$$\forall p < q : \langle K| a_p^\dagger a_q |L\rangle = \begin{cases} +1, \text{ if } \sum_{i=p+1}^{q-1} b_i \text{ is even} \\ -1, \text{ if } \sum_{i=p+1}^{q-1} b_i \text{ is odd} \end{cases} \tag{3.8}$$

As full space determinant $|K\rangle \in \mathcal{C}_i$ can be rewritten as a sum of sub-determinants $|K\rangle = \left|K^{\mathbb{X}_1^{\mathcal{C}_i}}\right\rangle \oplus \left|K^{\mathbb{X}_2^{\mathcal{C}_i}}\right\rangle \oplus \cdots$ where $\left|K^{\mathbb{X}_1^{\mathcal{C}_i}}\right\rangle \in \mathbb{X}_1^{\mathcal{C}_i}$ and $\left|K^{\mathbb{X}_2^{\mathcal{C}_i}}\right\rangle \in \mathbb{X}_2^{\mathcal{C}_i}$. The intra-GAS one-electron excitation implicitly suggest that $|K\rangle$ and $|L\rangle$ are in the same category. Then the symbolic matrix element could be rewritten as:

$$\begin{aligned} &\text{when } |K\rangle, |L\rangle \in \mathcal{C}_i \text{ and } p, q \in \mathbb{X}_j : \\ &\quad \langle K| \hat{E}_{pq} |L\rangle = \left\langle K^{\mathbb{X}_j^{\mathcal{C}_i}} \right| \hat{E}_{p^{\mathbb{X}_j} q^{\mathbb{X}_j}} \left| L^{\mathbb{X}_j^{\mathcal{C}_i}} \right\rangle \times \prod_{k \neq j} \delta(K^{\mathbb{X}_k^{\mathcal{C}_i}}, L^{\mathbb{X}_k^{\mathcal{C}_i}}) \end{aligned} \tag{3.9}$$

And for inter-GAS one-electron excitation, $|K\rangle$ and $|L\rangle$ must be in different categories. Similar the symbolic matrix element could be rewritten as:

$$\begin{aligned} &\text{when } |K\rangle \in \mathcal{C}_i, |L\rangle \in \mathcal{C}_k, p \in \mathbb{X}_j, q \in \mathbb{X}_l, p < q : \\ &\quad \langle K| \hat{E}_{pq} |L\rangle = \left\langle K^{\mathbb{X}_j^{\mathcal{C}_i}} K^{\mathbb{X}_l^{\mathcal{C}_i}} \right| \hat{E}_{p^{\mathbb{X}_j} q^{\mathbb{X}_l}} \left| L^{\mathbb{X}_j^{\mathcal{C}_k}} L^{\mathbb{X}_l^{\mathcal{C}_k}} \right\rangle \times P^{\mathbb{X}_j \mathbb{X}_l} \times \prod_{m \neq j,l} \delta(K^{\mathbb{X}_m^{\mathcal{C}_i}}, L^{\mathbb{X}_m^{\mathcal{C}_k}}) \end{aligned} \tag{3.10}$$

where the $P^{\mathbb{X}_j \mathbb{X}_l}$ is a phase factor defined as:

$$\text{when } p \leq q : P^{\mathbb{X}_j \mathbb{X}_l} = \begin{cases} +1, \text{ if } \sum_{a=j+1}^{l-1} n_{a_i}^{\mathcal{C}} \text{ is even} \\ -1, \text{ if } \sum_{a=j+1}^{l-1} n_{a_i}^{\mathcal{C}} \text{ is odd} \end{cases} \tag{3.11}$$

Thus, instead of storing the full space one-electron excitation list, we choose to only store the sub-determinant address involved in the excitations, and the δ parts in Eqs. (3.9) and (3.10) are left to be reconstructed the *on-the-fly* during sigma formation.

For intra-GAS one-electron excitation, the following 5 elements are stored: $A^{\mathbb{X}_i}(K)$, $p^{\mathbb{X}_i}$, $q^{\mathbb{X}_i}$, $A^{\mathbb{X}_i}(L)$, $\left\langle K^{\mathbb{X}_i} \right| \hat{E}_{p^{\mathbb{X}_i} q^{\mathbb{X}_i}} \left| L^{\mathbb{X}_i} \right\rangle$, where the symbolic matrix elements are compute similarly

as the full space:

$$\text{when } p^{\mathbb{X}_i} < q^{\mathbb{X}_i} : \left\langle K_i^{\mathbb{X}} \right| \hat{E}_{p^{\mathbb{X}_i} q^{\mathbb{X}_i}} \left| L^{\mathbb{X}_i} \right\rangle = \begin{cases} +1, \text{ if } \sum_{j=p^{\mathbb{X}_i}+1}^{q^{\mathbb{X}_i}-1} b_j \text{ is even} \\ -1, \text{ if } \sum_{j=p^{\mathbb{X}_i}+1}^{q^{\mathbb{X}_i}-1} b_j \text{ is odd} \end{cases} \tag{3.12}$$

For inter-GAS one-electron excitation list, the address of four sub-determinants are resolved and store, resulting in 7 elements for each excitation: $A^{\mathbb{X}_i}(K)$, $A^{\mathbb{X}_j}(K)$, $p^{\mathbb{X}_i}$, $q^{\mathbb{X}_j}$, $A^{\mathbb{X}'_i}(L)$, $A^{\mathbb{X}'_j}(L)$, $\left\langle K^{\mathbb{X}_i} K^{\mathbb{X}_i} \right| \hat{E}_{p^{\mathbb{X}_i} q^{\mathbb{X}_j}} \left| L^{\mathbb{X}'_i} L^{\mathbb{X}'_j} \right\rangle$, where the symbolic matrix elements are computed as: ,

$$\text{when } p < q : \left\langle K^{\mathbb{X}_i} K^{\mathbb{X}_j} \right| \hat{E}_{p^{\mathbb{X}_i} q^{\mathbb{X}_j}} \left| L^{\mathbb{X}'_i} L^{\mathbb{X}'_j} \right\rangle = \begin{cases} +1, \text{ if } \sum_{k=p^{\mathbb{X}_i}+1}^{m_i} b_k + \sum_{l=1}^{q^{\mathbb{X}_j}-1} b_l \text{ is even} \\ -1, \text{ if } \sum_{k=p^{\mathbb{X}_i}+1}^{m_i} b_k + \sum_{l=1}^{q^{\mathbb{X}_j}-1} b_l \text{ is odd} \end{cases} \tag{3.13}$$

3.2.4 Blockwise Sigma Formation with Dense Matrix-Matrix Multiplications

Given a correlation space partitioned into a number of N_{GAS} GAS and certain occupation restrictions on each GAS, there are a number of N_{Cat} determinant categories. Then, the sigma formation of $|K\rangle \in \mathcal{C}_i$ can be rewritten as summation over categorical segments:

$$\sigma(K) = \sum_{ab}^{N_{\text{DAS}}} {}^{1\text{e}}\sigma^{\mathbb{X}_a \mathbb{X}_b}(K) + \sum_{abcd}^{N_{\text{DAS}}} {}^{2\text{e}}\sigma^{\mathbb{X}_a \mathbb{X}_b \mathbb{X}_c \mathbb{X}_d}(K) \tag{3.14}$$

where the segmented one-electron and two-electron sigma formation are defined with $\hat{\mathcal{E}}^{\mathbb{X}_a \mathbb{X}_b}$ and $\hat{\mathcal{E}}^{\mathbb{X}_a \mathbb{X}_b} \hat{\mathcal{E}}^{\mathbb{X}_c \mathbb{X}_d}$:

$${}^{1\text{e}}\sigma^{\mathbb{X}_a \mathbb{X}_b}(K) = \sum_{L \in \mathcal{C}_j} \sum_{\hat{E}_{pq} \in \hat{\mathcal{E}}^{\mathbb{X}_a \mathbb{X}_b}} h'_{pq} \left\langle K \right| \hat{E}_{pq} \left| L \right\rangle C(L) \tag{3.15}$$

$${}^{2\text{e}}\sigma^{\mathbb{X}_a \mathbb{X}_b \mathbb{X}_c \mathbb{X}_d}(K) = \frac{1}{2} \sum_{L \in \mathcal{C}_j} \sum_{J \in \mathcal{C}_k} \sum_{\hat{E}_{pq} \in \hat{\mathcal{E}}^{\mathbb{X}_a \mathbb{X}_b}} \sum_{\hat{E}_{rs} \in \hat{\mathcal{E}}^{\mathbb{X}_c \mathbb{X}_d}} g_{pqrs} \left\langle K \right| \hat{E}_{pq} \left| J \right\rangle \left\langle J \right| \hat{E}_{rs} \left| L \right\rangle C(L) \tag{3.16}$$

where the category of L ($\mathcal{C}_j$) for for 1 electron or 2 electron part are uniquely determined by the categorical operators.

From , it's easy to decompose the global and categorical address of K into its address of sub-determinants:

$$ {}^{1e}\sigma^{\mathbb{X}_a\mathbb{X}_b}(K) = {}^{1e}\sigma^{\mathbb{X}_a\mathbb{X}_b}(\cdots, K^{\mathbb{X}_a^{\mathcal{C}_i}}, \cdots, K^{\mathbb{X}_b^{\mathcal{C}_i}} \cdots) \tag{3.17} $$

$$ {}^{2e}\sigma^{\mathbb{X}_a\mathbb{X}_b\mathbb{X}_c\mathbb{X}_d}(K) = {}^{2e}\sigma^{\mathbb{X}_a\mathbb{X}_b}(\cdots, K^{\mathbb{X}_a^{\mathcal{C}_i}}, \cdots, K^{\mathbb{X}_b^{\mathcal{C}_i}}, \cdots, K^{\mathbb{X}_c^{\mathcal{C}_i}}, \cdots, K^{\mathbb{X}_d^{\mathcal{C}_i}} \cdots) \tag{3.18} $$

With plugin of Eqs. (3.12) and (3.13), for one-electron part, we can have:

$$ \begin{aligned} &\text{when } \forall c \neq \{a,b\}, \left|K^{\mathbb{X}_c^{\mathcal{C}_i}}\right\rangle = \left|L^{\mathbb{X}_c^{\mathcal{C}_j}}\right\rangle : \\ &\quad {}^{1e}\sigma^{\mathbb{X}_a\mathbb{X}_b}(\cdots, K^{\mathbb{X}_a^{\mathcal{C}_i}}, \cdots, K^{\mathbb{X}_b^{\mathcal{C}_i}} \cdots) = \\ &\qquad P^{\mathbb{X}_a\mathbb{X}_b} \sum_{L^{\mathbb{X}_a^{\mathcal{C}_j}} L^{\mathbb{X}_b^{\mathcal{C}_j}}} \sum_{p^{\mathbb{X}_a} q^{\mathbb{X}_b}} h'_{pq} \left\langle K^{\mathbb{X}_a^{\mathcal{C}_i}} K^{\mathbb{X}_b^{\mathcal{C}_i}} \middle| \hat{E}_{p^{\mathbb{X}_a} q^{\mathbb{X}_b}} \middle| L^{\mathbb{X}_a^{\mathcal{C}_j}} L^{\mathbb{X}_b^{\mathcal{C}_j}} \right\rangle C(\cdots, L^{\mathbb{X}_a^{\mathcal{C}_j}}, \cdots, L^{\mathbb{X}_b^{\mathcal{C}_j}} \cdots) \end{aligned} \tag{3.19} $$

$$ \begin{aligned} &\text{when } \forall e \neq \{a,b,c,d\}, \left|K^{\mathbb{X}_e^{\mathcal{C}_i}}\right\rangle = \left|L^{\mathbb{X}_e^{\mathcal{C}_j}}\right\rangle : \\ &\quad {}^{2e}\sigma^{\mathbb{X}_a\mathbb{X}_b\mathbb{X}_c\mathbb{X}_d}(\cdots, K^{\mathbb{X}_a^{\mathcal{C}_i}}, \cdots, K^{\mathbb{X}_b^{\mathcal{C}_i}}, \cdots, K^{\mathbb{X}_c^{\mathcal{C}_i}}, \cdots, K^{\mathbb{X}_d^{\mathcal{C}_i}} \cdots) = \\ &\qquad \frac{1}{2} P^{\mathbb{X}_a\mathbb{X}_b} P^{\mathbb{X}_c\mathbb{X}_d} \sum_{L^{\mathbb{X}_a^{\mathcal{C}_j}} L^{\mathbb{X}_b^{\mathcal{C}_j}} L^{\mathbb{X}_c^{\mathcal{C}_j}} L^{\mathbb{X}_d^{\mathcal{C}_j}}} \sum_{p^{\mathbb{X}_a} q^{\mathbb{X}_b} r^{\mathbb{X}_c} s^{\mathbb{X}_d}} \left\{ g_{pqrs} \left\langle K^{\mathbb{X}_a^{\mathcal{C}_i}} K^{\mathbb{X}_b^{\mathcal{C}_i}} \middle| \hat{E}_{p^{\mathbb{X}_a} q^{\mathbb{X}_b}} \middle| J^{\mathbb{X}_a^{\mathcal{C}_j}} J^{\mathbb{X}_b^{\mathcal{C}_j}} \right\rangle \right. \\ &\qquad \left. \times \left\langle J^{\mathbb{X}_c^{\mathcal{C}_i}} J^{\mathbb{X}_d^{\mathcal{C}_i}} \middle| \hat{E}_{r^{\mathbb{X}_c} s^{\mathbb{X}_d}} \middle| L^{\mathbb{X}_c^{\mathcal{C}_j}} L^{\mathbb{X}_d^{\mathcal{C}_j}} \right\rangle C(\cdots, L^{\mathbb{X}_a^{\mathcal{C}_j}}, \cdots, L^{\mathbb{X}_b^{\mathcal{C}_j}}, \cdots, L^{\mathbb{X}_c^{\mathcal{C}_j}}, \cdots, L^{\mathbb{X}_d^{\mathcal{C}_j}} \cdots) \right\} \end{aligned} \tag{3.20} $$

We extended Kownles-Handy algorithms into GAS region and developed a matrix-matrix multiplication segmented two-electron sigma formation. The following extra notations are defined to simplify the discussion:

- $\mathbb{X}_{abcd}^{\mathcal{C}_i} = \mathbb{X}_a^{\mathcal{C}_i} \otimes \mathbb{X}_b^{\mathcal{C}_i} \otimes \mathbb{X}_c^{\mathcal{C}_i} \otimes \mathbb{X}_d^{\mathcal{C}_i}$

- $\mathbb{X}^{\mathcal{C}_i}_{\overline{abcd}} = \bigotimes_{e\neq\{a,b,c,d\}} \mathbb{X}^{\mathcal{C}_i}_e$
- $\mathrm{NZ}^{\mathbb{X}^{\mathcal{C}_i}_a \mathbb{X}^{\mathcal{C}_j}_b}$: the nonzero elements arising from one-electron excitation list.

Thus, the segmented sigma formation could be performed in the folloing steps:

$\forall J^{\mathbb{X}^{\mathcal{C}_k}_{abcd}}$, and $J^{\mathbb{X}^{\mathcal{C}_k}_{\overline{abcd}}} = K^{\mathbb{X}^{\mathcal{C}_i}_{\overline{abcd}}} = L^{\mathbb{X}^{\mathcal{C}_j}_{\overline{abcd}}}$:

$$\boldsymbol{X}(\mathrm{NZ}^{\mathbb{X}^{\mathcal{C}_i}_a \mathbb{X}^{\mathcal{C}_k}_b}, \mathrm{NZ}^{\mathbb{X}^{\mathcal{C}_k}_c \mathbb{X}^{\mathcal{C}_j}_d}) \leftarrow \boldsymbol{g}(pq,rs) \left\langle K^{\mathbb{X}^{\mathcal{C}_i}_{ab}} \right| \hat{E}_{p^{\mathbb{X}_a} q^{\mathbb{X}_b}} \left| J^{\mathbb{X}^{\mathcal{C}_k}_{ab}} \right\rangle \left\langle J^{\mathbb{X}^{\mathcal{C}_k}_{cd}} \right| \hat{E}_{r^{\mathbb{X}_c} s^{\mathbb{X}_d}} \left| L^{\mathbb{X}^{\mathcal{C}_j}_{cd}} \right\rangle \tag{3.21}$$

$$\boldsymbol{\Omega}(\mathrm{NZ}^{\mathbb{X}^{\mathcal{C}_k}_c \mathbb{X}^{\mathcal{C}_j}_d}, J^{\mathbb{X}^{\mathcal{C}_j}_{\overline{abcd}}}) \leftarrow \sum_{L^{\mathbb{X}^{\mathcal{C}_j}_{pqrs}}} C(\cdots, L^{\mathbb{X}^{\mathcal{C}_j}_a}, \cdots, L^{\mathbb{X}^{\mathcal{C}_j}_b}, \cdots, L^{\mathbb{X}^{\mathcal{C}_j}_c}, \cdots, L^{\mathbb{X}^{\mathcal{C}_j}_d} \cdots) \tag{3.22}$$

$$\boldsymbol{\Lambda}(\mathrm{NZ}^{\mathbb{X}^{\mathcal{C}_i}_a \mathbb{X}^{\mathcal{C}_k}_b}, J^{\mathbb{X}^{\mathcal{C}_j}_{\overline{abcd}}}) \leftarrow \frac{1}{2} P^{\mathbb{X}_a \mathbb{X}_b} P^{\mathbb{X}_c \mathbb{X}_d} \sum_{\mathrm{NZ}^{\mathbb{X}^{\mathcal{C}_k}_c \mathbb{X}^{\mathcal{C}_j}_d}} \boldsymbol{X}(\mathrm{NZ}^{\mathbb{X}^{\mathcal{C}_i}_a \mathbb{X}^{\mathcal{C}_k}_b}, \mathrm{NZ}^{\mathbb{X}^{\mathcal{C}_k}_c \mathbb{X}^{\mathcal{C}_j}_d}) \boldsymbol{\Omega}(\mathrm{NZ}^{\mathbb{X}^{\mathcal{C}_k}_c \mathbb{X}^{\mathcal{C}_j}_d}, J^{\mathbb{X}^{\mathcal{C}_j}_{\overline{abcd}}}) \tag{3.23}$$

$${}^{2\mathrm{e}}\sigma^{\mathbb{X}_a \mathbb{X}_b \mathbb{X}_c \mathbb{X}_d}(\cdots, K^{\mathbb{X}^{\mathcal{C}_i}_a}, \cdots, K^{\mathbb{X}^{\mathcal{C}_i}_b}, \cdots, K^{\mathbb{X}^{\mathcal{C}_i}_c}, \cdots, K^{\mathbb{X}^{\mathcal{C}_i}_d} \cdots) \leftarrow \sum_{\mathrm{NZ}^{\mathbb{X}^{\mathcal{C}_i}_a \mathbb{X}^{\mathcal{C}_k}_b}} \boldsymbol{\Lambda}(\mathrm{NZ}^{\mathbb{X}^{\mathcal{C}_i}_a \mathbb{X}^{\mathcal{C}_k}_b}, J^{\mathbb{X}^{\mathcal{C}_j}_{\overline{abcd}}})) \tag{3.24}$$

where the Eq. (3.23) is the matrix-matrix multiplication step, while Eqs. (3.21) and (3.22) are the gathering step and Eq. (3.24) is the scattering step.

3.2.5 Distributed Implementation

With the scheme in Sec. 3.2.2, the total MRCI vector space are broken down into small segments. Here we are using the naive static balancing approach where the CI vector segments are solely distributed to MPI ranks based on their lengths. Once the division is established for a MRCI calculation, it will remained static along the whole davidson iterations, and each rank will only store the $\boldsymbol{C}^i$ and $\boldsymbol{\sigma}^i$ segments corresponding to the same determinants from the division scheme. Without any prior considerations such as the connections between each categories, the distributed sigma formalism will need to iterate all the $\{\boldsymbol{C}^i\}$ segments across the entire MPI ranks.

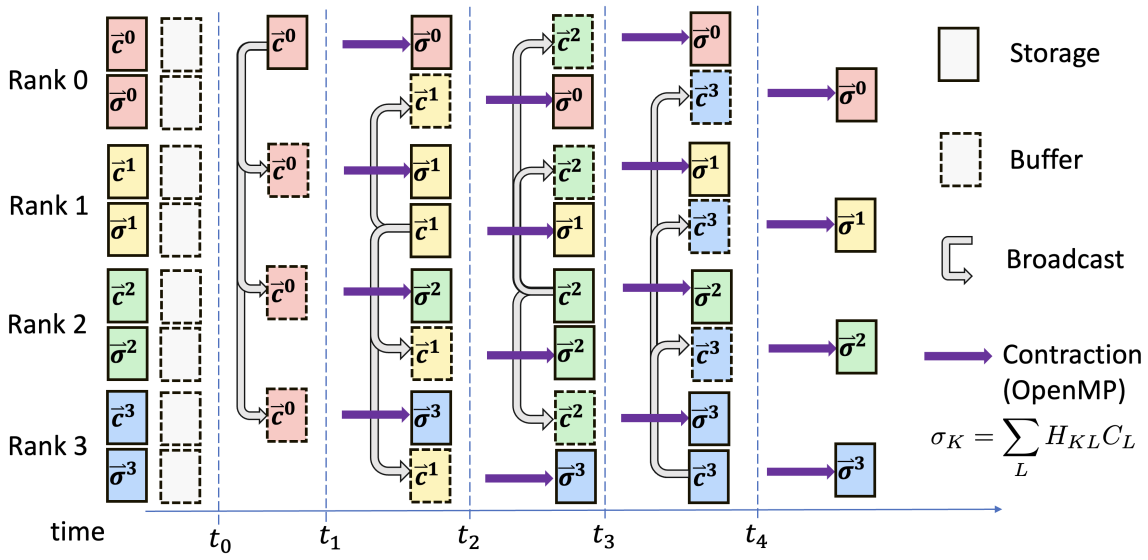

Figure 3.4. A schematic of the distributed sigma formation with 4 MPI Ranks. The non-blocking broadcast is used to transfer $\{\boldsymbol{C}^i, i \neq 0\}$ coefficients between different MPI ranks. The communiation and computation are overlapped between t_1 and t_4.

Here we adopted the latest MPI standard and utilized the non-blocking broadcast to minimizing the communication costs with multiple machines. An example schematic for each sigma formation with 4 MPI ranks is sketched in Fig. 3.4. At start of the sigma formation, we allocated two buffers ($\boldsymbol{b}_1$ and $\boldsymbol{b}_2$) on each MPI rank to hold the $\{\boldsymbol{C}^i\}$ segments from other ranks. Then in the first trunk of time between t_0 and t_1, a blocking broadcast is performed to send $\boldsymbol{C}^0$ to $\boldsymbol{b}_1$ on different ranks. Starting at t_1, a non-blocking broadcast is issued for data transfer of $\boldsymbol{C}^1$ to $\boldsymbol{b}_2$ on each rank and at the same time, sigma formation are done with the $\boldsymbol{C}^0$ (temporiarily stored in $\boldsymbol{b}_1$). In this way broadcasting $\boldsymbol{C}^1$ and contraction of $\boldsymbol{\sigma}^i = \boldsymbol{H}^{i0}\boldsymbol{C}^0$ are performed simultaneously. Similarly, broadcasting $\boldsymbol{C}^2$ overlaps with contraction of $\boldsymbol{\sigma}^i = \boldsymbol{H}^{i1}\boldsymbol{C}^1$ between t_2 and t_3; broadcasting $\boldsymbol{C}^3$ overlaps with contraction of $\boldsymbol{\sigma}^i = \boldsymbol{H}^{i2}\boldsymbol{C}^2$ between t_3 and t_4. At the last trunk of time, the last contraction $\boldsymbol{\sigma}^i = \boldsymbol{H}^{i3}\boldsymbol{C}^3$is conducted to finalize the sigma formation. Note that each segmented contractions are paralleled with shared-memory multiprocessing SMP *via* OpenMP, hence our implementation is a hybrid MPI/OpenMP program.

3.3 Test Calculations and Performance Evaluations

In this section, we will evaluate the performance especially the parallel scaling of the new MRCI formalism and its distributed implementation. During our development, we found out that the performance of this MRCI program highly depends on the underlying hardware and runtime environment settings.

3.3.1 Test Environments and Test Cases

All of the test we conducted are on the high performance computing cluster *Klone* at University of Washington. The hardware and software details are summarized in Tab. 3.3. For the simplicity, we used benzene as our the test molecule. X2C Hamiltonian was used with cc-pVDZ basis. The same reference CAS(6, 12) was across all the test cases with up to single and double excitations between correlated core, CAS and correlated virtual space. We formulate multiple MRCISD benchmarks with variances in terms of number of correlated core and virtual orbitals, and the details are summarized in Tab. 3.2. Note that benzene-9.9b is a full correlated MRCISD calculation with no frozen core and virtual orbitals and due to the resources limits, the test in this section only covers up to benzene-1.1b case.

Table 3.3. Test environment details (Hardware and Software) of *Klone*

CPU Architecture	Intel Cascade Lake (Xeon(R) Gold 6230)
CPU Frequency	2.1 GHz
# of Sockets	2
# of Cores per Socket	20
# of NUMA per socket	1
Total Memory	192 GB
Memory per NUMA	96 GB
NIC speed	100 Gbps
L3 Cache	27.5 MB
L3 Cache per core	0.6875 MB
MPI Compiler	Intel MPI 2021

3.3.2 Parallel Performance

The parallel performances are evaluated in two aspects: shared memory multiprocessing (SMP) performance and inter-node performance. We use the benzenze-78m (defined Tab. 3.2) for all the parallel performance tests. The speedup is defined as:

$$\mathcal{S}(n) = \frac{t(1)}{t(n)} \tag{3.25}$$

where $t(1)$ is the wall time to build single sigma vectors using 1 core (for SMP case) or 1 node (for inter-node case), while $t(n)$ is the wall time to perform the same sigma formation using n cores or n nodes.

For SMP performance, we tested up to 40 cores which is the largest number of cores from a single computer node. As shown in Fig. 3.5a), initially, the implementation scales well up to around 10 CPUs with 7.2 times speedup; but for CPUs more than 10 cores, the parallel efficiency is worsen, only 11.3 times speedup with 20 cores, and 13.4 cores with 40 cores. It is often challenging to obtain a good SMP performance over large number of cores for Linux clusters due to the memory bandwidth especially the fast caches (27.5 MB of L3 cache are shared by all 40 cores in our case). The similar situation was reported by Knecht [75] *et. al.* in 2009 and they only obtained 2.58 speed up for 4 shared memory processes.

For inter-node performance, the result is more satisfactory. As shown in Fig. 3.5b), we are able to gain 10 times speedup for using 16 nodes compared to using only 1 nodes. Since the large portion of the communication is done using non-blocking broadcast, it would be hard to completely separate the computation and communication times. Still we are able to measure the time elapsed during the whole computations and the total time for sigma formation on each node. Then we designate the difference between time as the time spent for non-overlap communication and idled due to imbalanced workloads:

$$t_{\text{comm}} = \max_{i=0}^{N_{\text{node}}-1}(t^i_{\text{total}} - t^i_{\text{comp}}) \tag{3.26}$$

Such breakdown for different ranks are shown in Fig. 3.5c). The time for pure computation goes down proportionally as the increase of number of computer nodes, while the time used for communication and load balance remains similarly. The nearly constant communication time provides great horizontal scalability for calculations needing large amount of machines.

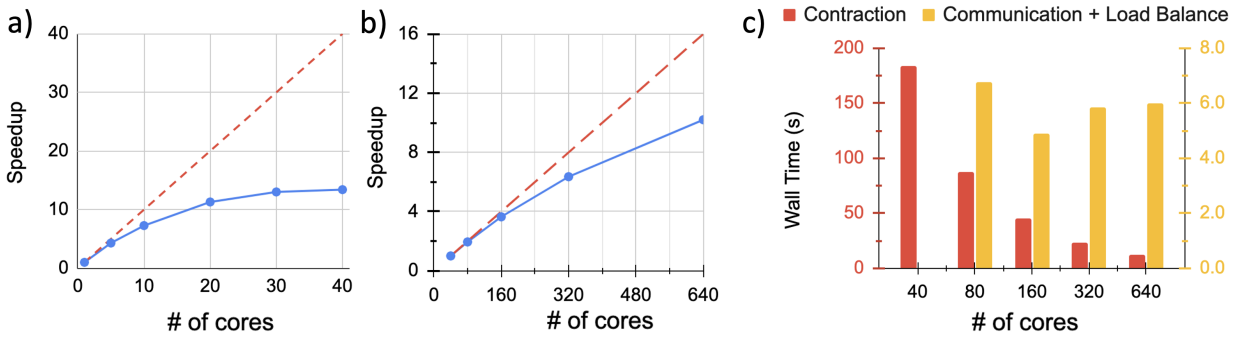

Figure 3.5. The parallel performance of the distributed MRCI implementation using GAS. All tests here are using benzenze-78m defined in Tab. 3.2 and the average wall time of single sigma vector formation are compared. a) SMP speedup of single sigma build time on single machine with multiple CPUs. b) Inter-node speedup of single sigma build time with multiple machines. The red dash lines in a) and b) are ideal scalings. c) The breakdown of contraction and communication for sigma build time with multiple machines.

3.3.3 Performance Tuning

In our tests, we also found out that the inter-node performance of our MRCI implementation relies on a good setting of using computational resources. Because of the bad scaling of the SMP performance, we were considering breaking down the cores of each machine into two separate MPI ranks with 20 CPUs for each of the rank. Also, the Intel MPI compiler provides different runtime algorithms for non-blocking broadcast through setting the environment variable *I_MPI_ADJUST_IBCAST*. Through running the default Intel MPI Benchmarks for non-blocking collectives (IMB-NBC), specifically non-blocking broadcast with 8 nodes on *Klone*, we found out that the Binomial algorithm (*I_MPI_ADJUST_IBCAST* = 1) has the best performance. Thus we designed the four experiments with settings defined in Tab. 3.4 to run the same benzene-78m test case.

Table 3.4. Different test setting of running benzene-78m with 8 nodes and 40 cores per node.

Test Case	# of MPI Ranks	# of Cores per Ranks	*I_MPI_ADJUST_IBCAST*
A	8	40	1 (optimized)
B	8	40	0 (default)
C	16	20	1 (optimized)
D	16	20	0 (default)

From the results showing in Fig. 3.6, first of all, a clearly great improvement over the communication time is observed by switching the non-blocking run time algorithm from default to optimized one. Both from test setting B to A or test setting D to C, although the computation times are comparable, the communication times using A and C shrink to only around 1/3 of B and D respectively. Unfortunately, on *Klone*, breaking the whole node into two ranks increases both the computation and communication times. This might due to the fact the all of the 40 cores shares the same L3 cache, have two separate ranks working on different part of the sigma might introduces additional cache misses.

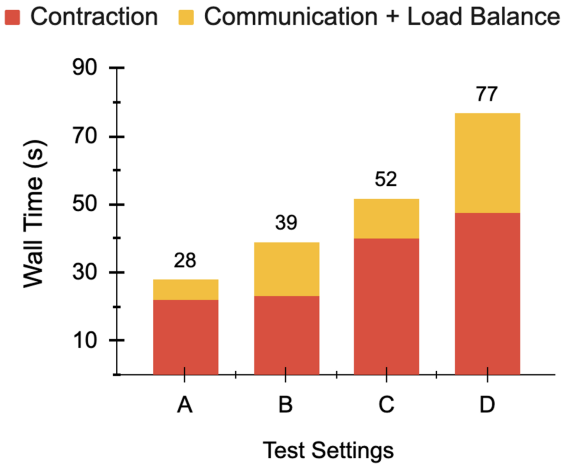

Figure 3.6. The average wall time of single sigma vector formation in different computational settings on *Klone*. All tests here are using benzene-78m defined in Tab. 3.2 and run on 8 nodes with 40 cores per node.

We also investigated the influence of breaking down the orbital space into different GAS

sizes. The experiments are done with the virtual orbital spaces of the benzene-311m benchmark, as shown in Tab. 3.5. When moving to 5 orbitals per virtual GAS scheme to 20 orbitals per virtual GAS scheme, we observed that the number categories goes down by 90%, the standard deviation of the length distributed to different nodes increase by three order of magnitude.

Table 3.5. The CI vector distribution profile for running benzene-311m with various number of orbital per virtual GAS on 8 nodes and 40 cores per node.

# of orbitals per virtual GAS	# of virtual GASs	# of Categories	STD of Determinants
5	36	12,690	82
10	18	3,438	337
15	12	1,650	11,456
20	9	999	33,570

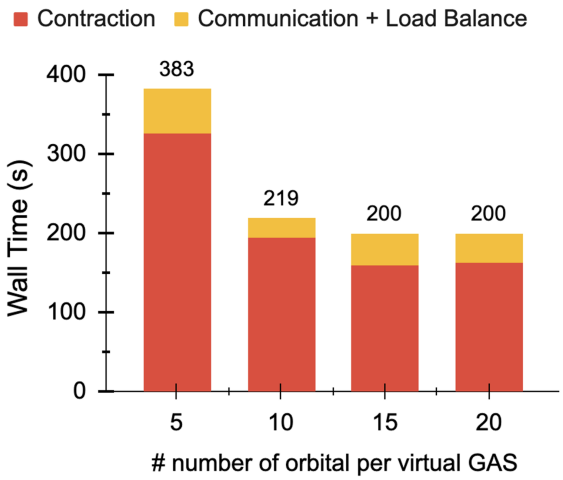

Figure 3.7. The average wall time of single sigma vector formation with different division of the virtual space. All tests here are using benzene-311m defined in Tab. 3.2 and run on 8 nodes with 40 cores per node.

However as the sigma formation time shown in Fig. 3.7, we only found out significant performance regression when number of orbital is 5 per virtual GAS. When number of orbitals in each GAS is smaller, there will more batches of small matrix-matrix multiplications instead

of small batches of the larger one. Thus, the time for computation is expected to increase for smaller number of orbitals in each GAS. The mysterious part was the communication/load balancing time was also large for number of orbital is 5 per virtual GAS, even if it have better segmentation of the whole CI vector (only 82 deification out of near 39 million determinants). As we describe in Sec. 3.2.5, the distribution of the CI vectors are solely based on the length of each segments, which might result in randomness on the static load balancing. More research on how to quantify the workload for a segment of CI vector need to be conduct in order to optimize the static load balancing in the future.

3.3.4 Performance Scaling with Problem Dimensions

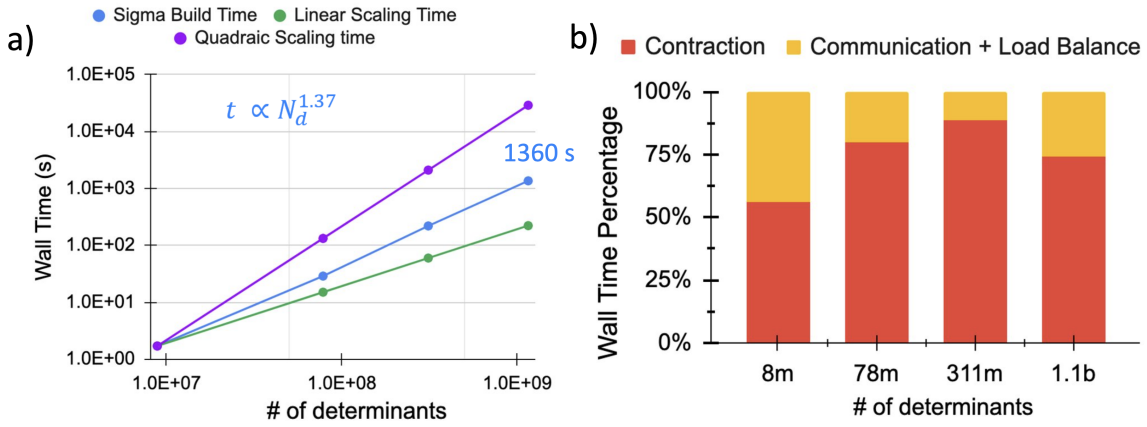

Figure 3.8. The computation scaling of the distributed MRCI implementation with various number of determinants. All the tests here are defined in Tab. 3.2 and run on 8 nodes with 40 cores per nodes. a) The average wall time of single sigma vector formation for MRCI problems with different dimensions. b) The breakdown of contraction and communication time in percentage for all the test cased in a).

With the best performance setting on *Klone*, we then investigated how our implementation scales with the problem dimensions. Test benchmarks of benzene (defined Tab. 3.2) with 8 million, 78 million, 311 million and 1.1 billion are tested with 8 computer nodes on *Klone*. As the result shown in Fig. 3.8a, the sigma formation time scales nearly linearly as $t \propto N_d^{1.37}$. For the largest test we tested here (benzene-1.1b), only around 1430 s is needed for

single sigma formation. To our best knowledge, no one has been reported such numbers for large scale relativistic MRCI methods. Breaking down the computation and communication time into percentage as Fig. 3.8b), we found out that with increase of the determinants space from 8m to 311m, the calculations shift to be more computation intensive, which make is promising to use large number of computer nodes. For the case of benzene-1.1b, the increase of communication time was likely due to the static load balance change with introducing of more correlated core orbitals.

Chapter 4

MRCI BENCHMARKS ON ATOMIC ELECTRONIC FINE STRUCTURE SPLITTINGS

To establish a standard procedure for the accuracy evaluation of the relativistic multi-reference methods, a few benchmark sets on atomic electronic fine structure splitting are built, which includes p-block, d-block and f-block elements calculations. This chapter is adapted with permission from: Hang Hu, Andrew J. Jenkins, Hongbin Liu, Joseph M. Kasper, Michael J. Frisch, and Xiaosong Li *J. Chem. Theory Comput.*, **2020**, 16(5), 2975–2984, Copyright [58]

4.1 Computational Details

The benchmark sets in this chapter contains three parts which computes the splitting of open shell s^2p^1, s^2d^1 and f^1 systems from neutral group 13 elements, neutral group 3 elements and uranium(V) atom, respectively. The CASSCF and MRCI results are computed using X2C Hamiltonian (Eq. (1.15)) and then compared against experiments and available computation results from existing literature. One-electron X2C transformation is carried out in an uncontracted basis over primitives. After four-component to two-component transformation, primitive bases are re-contracted and all following electronic structure methods (X2C-SA-CASSCF, X2C-MRCI) are performed in contracted basis.

In the optimization of reference X2C-SA-CASSCF wave functions, state-averaging is used. In all calculations presented, all states arising from the ground state term are equally averaged over. For group 13, the p^1 electron configuration gives 6 ^{2}P states, all of which are included in the equal state averaging procedure. Likewise, 10 ^{2}D states and 14 ^{2}F states are used for the group 3 elements and U(V)$^{5+}$ ions, respectively. State-averaging equally

over all states of a term recovers Kramers symmetry[63]. This symmetry is preserved in all subsequent X2C-MRCI calculations.

Importantaly for all the benchmarks here, certain virtual orbitals are not included in the treatment of dynamic correlation; these are the aforementioned 'frozen virtual' orbitals. Care must be taken in defining the correlated and frozen virtual orbital spaces. The lowest lying virtual orbitals produced during the X2C-SA-CASSCF procedure tend to be diffuse (as is common with SCF procedures) and are not likely to be key contributors to the correlation energy, therefore the spaces should not be defined by orbital energy alone. In the present work, virtual orbitals which are valence-like and suitable for correlating the neutral atom/molecule are generated from an Improved Virtual Orbital (IVO) procedure [59, 57]. In this procedure, a closed-shell cationic Fock matrix is constructed and diagonalized and subsequently used to transform the set of SCF virtual orbitals. This is a unitary transformation of the virtual space and so does not affect the energy of any model which treats all the virtuals equally, but it generates a set which is much more suitable for truncation. Selection of correlated virtual orbitals is based on this energy ordering and the physical nature of the orbital.

4.2 Fine Structure Splitting in Group 13 p-Block Elements

The p^1 electron configuration of group 13 elements gives rise to a ^{2}P ground state, which is further split into $^2P_{1/2} \rightarrow {}^2P_{3/2}$ levels due to spin-orbit coupling. Previous studies, using both relativistic two-component X2C-SA-CASSCF and four-component CASSCF[63, 154], have shown the importance of including dynamic correlation when computing fine structure splittings of group 13 p-block elements.

Table 4.1 lists computed fine structure splittings of selected group 13 elements using various methods with spin-orbit coupling treated at different levels, compared to experimental values. All X2C calculations were performed using the all-electron X2C-TZPAll-2c basis,[119] optimized for X2C calculations. CASPT2-SOC results[126] were computed using a large ANO-RCC basis. [124] Four-component Dirac-Coulomb-Breit CASSCF (4C-CASSCF) and

four-component internally contracted CASPT2 (4C-CASPT2) results[154] were obtained using the uncontracted relativistically optimized cc-pVTZ[30, 31] basis set. For all calculations in Tab. 4.1, the CASSCF reference includes all valence electrons and orbitals, resulting in a space consisting of 3 electrons and 8 (bi)spinor orbitals. Note that CASPT2-SOC calculation use a one-component framework with perturbative spin-orbit coupling. For X2C-MRCI calculations in Tab. 4.1, RAS1 space is empty, and RAS3 space includes all virtual spinor orbitals that are not included in RAS2/CAS. Such a MRCI configuration space is comparable to those used in the CASPT2 calculations.

	X2C-SA-CASSCF	X2C-MRCISD	CASPT2-SOC[126]	4C-CASSCF[154]	4C-CASPT2[154]	Exp.[85]
Ga	90(−11.8)	97 (−4.9)	99 (−2.9)	85 (−16.7)	93 (−8.8)	102
In	239 (−12.8)	254 (−7.3)	261 (−4.7)	230 (−16.1)	245 (−10.6)	274
Tl	863 (−10.7)	903 (−6.5)	893 (−7.6)	N/A	N/A	966

Table 4.1. The ground state ^{2}P energy splitting ($^2P_{1/2} \rightarrow {}^2P_{3/2}$ in meV) of group 13 elements. Percentage errors with respect to experiments are reported in parentheses. Calculations using the perturbative CASPT2-SOC[126] method and the four-component Dirac-Coulomb-Breit CASSCF method[154] are included for comparison.

Table 4.1 suggests that methods (X2C-SA-CASSCF and 4C-CASSCF) that have limited dynamic correlation underestimate fine structure splittings of group 13 elements. Including dynamic correlation via perturbation or MRCI significantly improves the computational results compared to experimental measurements.

The four component calculations show a larger error compared to other methods. This is likely due to the use of internal-contraction, with contraction errors of the order of tens of meV reported for MRCI[152]. For the largest atom in the test set, Tl, variational multireference X2C approaches consistently outperform the perturbative one-component method.

The X2C-MRCI framework introduced in this work allows for a flexible and adjustable definition of the correlation space. This capability gives an opportunity to probe the effect of correlation space on the accuracy of relativistic calculations. Figure 4.1 shows three different correlation spaces defined in the MRCI framework, with the calculated results listed

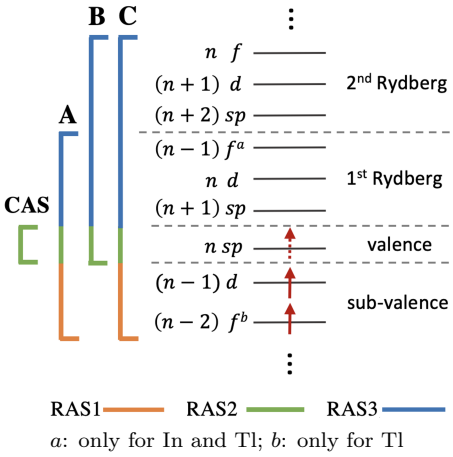

a: only for In and Tl; *b*: only for Tl

	X2C-SA-CASSCF	X2C-MRCISD		
		A	**B**	**C**
Ga	56	500,184	11,256	3,629,976
In	56	1,515,660	17,976	5,903,436
Tl	56	8,682,792	17,976	33,871,656

Figure 4.1. Top panel: definitions of selected correlation spaces. Orbital space is constructed from the X2C-SA-CASSCF reference, where solid and dotted arrows indicate fully and partially occupied orbitals, respectively. Note that virtual orbitals are ordered symbolically instead of energetically. **Bottom panel**: total numbers of two-component configurations in X2C-SA-CASSCF and X2C-MRCISD calculations.

in Tab. 4.2 for group 13 p-block elements. The largest correlation space **C** includes first- and second-Rydberg virtual spinor orbitals and sub-valence electrons, resulting in $\sim$ 30M two-component MRCI configurations for Tl. Table 4.2 shows that increasing the size of correlation space increases the $^2P_{1/2} - {}^2P_{3/2}$ fine structure splitting. Including the lowest Rydberg shells ($(n+1)sp$, nd, and $(n-1)f$) and sub-valence electrons in the correlation space **A** only slightly changes the fine structure splitting. The most significant increase in the splitting comes from the inclusion of second Rydberg shells in the correlation space (**B** and **C**). Between atoms, correlation spaces of a comparable size show similar errors. For all three group 13 elements investigated, MRCISD results converge to the experimental values as the correlation space increases.

Another advantage of the MRCI implementation using the RAS framework is the flexi-

	X2C-SA-CASSCF	X2C-MRCISD			Exp.[85]
		A	**B**	**C**	
Ga	90 (−11.8)	92 (−9.8)	97 (−4.9)	100 (−2.0)	102
In	239 (−12.8)	244 (−10.9)	254 (−7.3)	265 (−3.3)	274
Tl	863 (−10.7)	856 (−11.4)	902 (−6.6)	905 (−6.3)	966

Table 4.2. Ground state ^{2}P energy splittings ($^2P_{1/2} \rightarrow {}^2P_{3/2}$ in meV) of group 13 elements computed using X2C-MRCISD with three different correlation spaces defined in Fig. 4.1. Percentage errors with respect to experiments are reported in parentheses.

		Ga	In	Tl
X2C-MRCIS	$(m_h = 1, m_e = 1)$	94 (−7.8)	242 (−11.7)	848 (−12.2)
X2C-DDCI	$(m_h = 1, m_e = 2)$	99 (−2.9)	266 (−2.9)	926 (−4.1)

Table 4.3. Ground state fine structure splitting of group 13 elements ($^2P_{1/2} \rightarrow {}^2P_{2/3}$ in meV) using correlation space **C** defined in Fig. 4.1. Percentage errors with respect to experiments are reported in parentheses. Two MRCI implementations (MRCIS, DDCI) with flexible excitation restrictions in RAS1 and RAS3 are compared.

bility in choosing the truncation level of the excitation operator by restricting the maximum number of holes in RAS1 and the maximum number of electrons in RAS3. Table 4.3 shows the how different MRCI excitation truncations affect fine structure calculations of Ga ground state. Note that, in contrast to CIS, X2C-MRCIS also includes dynamic correlations even though it augments the CASSCF reference with only single excitations because the underlying reference already includes multiply excited configurations. For the same correlation space, X2C-DDCI[46] ($m_h = 1, m_e = 2$) and X2C-MRCISD ($m_h = 2, m_e = 2$) produced similar results, both outperforming X2C-MRCIS ($m_h = 1, m_e = 1$). This observation confirms that electron correlation arising from double excitations to the RAS3 space is an important contribution to the fine structure splitting.

4.3 Fine Structure Splitting in Group 3 d-Block Elements

For group 3 d-block elements, the d^1 electron configuration gives rise to a ^{2}D ground state, which is further split into $^2D_{3/2} \rightarrow {}^2D_{5/2}$ levels due to spin-orbit coupling. Table 4.4 lists ground state fine structure splittings of selected group 3 elements using multireference meth-

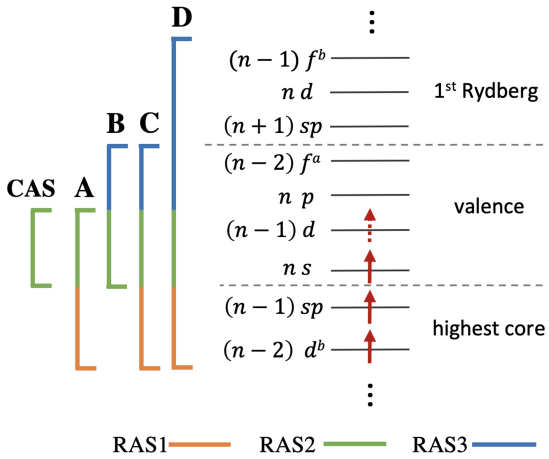

a: only for La; *b*: only for Y and La

	X2C-SA-CASSCF	X2C-MRCISD			
		A	**B**	**C**	**D**
Sc	220	26,356	796	220,972	2,252,020
Y	220	130,306	796	1,131,772	27,667,804
La	220	130,306	2,820	8,348,926	50,502,238

Figure 4.2. Top panel: definitions of selected correlation spaces. Orbital space is constructed from the X2C-SA-CASSCF reference, where solid and dotted arrows indicate fully and partially occupied orbitals, respectively. Note that virtual orbitals are ordered symbolically instead of energetically. **Bottom panel**: total numbers of two-component configurations in X2C-SA-CASSCF and X2C-MRCISD calculations.

ods with various correlation spaces defined in Fig. 4.2. The X2C-SA-CASSCF reference includes a total of 12 spinor orbitals (ns and $(n-1)d$) with 3 electrons in the active space, resulting in 220 two-component configurations. Since the ground state splitting of Sc computed by X2C-SA-CASSCF is already in excellent agreement with experiment, MRCI results do not show any improvement. Including the highest core electrons or/and valence virtual orbitals (np or/and $(n-2)f$) in correlation spaces **A**, **B**, **C**, defined in Fig. 4.2, significantly improve the fine structure splittings of Y and La. This observation suggests that dynamic correlation is important for predicting fine structure splittings of row 5-6 elements.

The dependence of X2C-MRCISD ground state energies and fine structure splittings of La on the correlation space is investigated in Fig. 4.3. As the correlation space increases, both the ground state energy and fine structure splitting of La are improved. Including additional

	X2C-SA-CASSCF	X2C-MRCISD				Exp.[85]
		A	**B**	**C**	**D**	
Sc	21	23	22	23	23	21
Y	55	58	60	65	64	66
La	92	101	107	116	115	130

Table 4.4. Ground state fine structure splittings ($^2D_{3/2} - {}^2D_{5/2}$ in meV) of group 3 d-block elements. X2C-MRCISD calculations use various correlation spaces defined in Fig. 4.2. The X2C-SA-CASSCF reference consists of 3 electrons in 12 spinor orbitals (ns and $(n-1)d$).

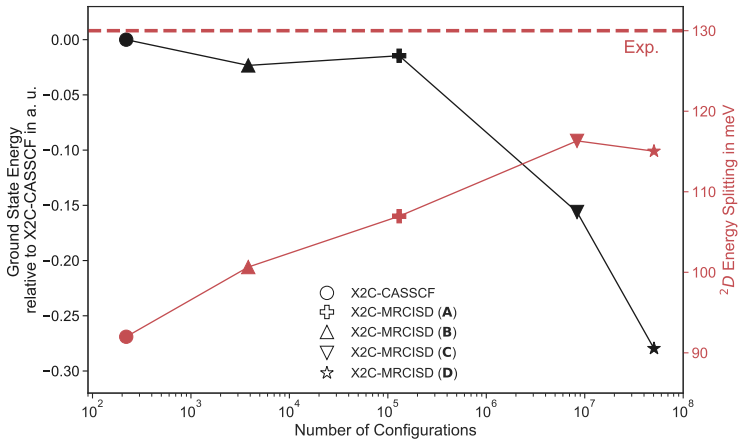

Figure 4.3. Dependence of X2C-MRCISD ground state energies (in a.u.) and fine structure splittings ($^2D_{3/2} - {}^2D_{5/2}$ in meV) of La on the correlation space. X2C-MRCISD ground state energies are relative to the X2C-CASSCF value.

valence shells ($4f$ and $6p$ in space **B**) or highest energy core orbitals ($4d$ and $5sp$ in space **A**) in the correlation space only slightly improves the energy but significantly improves the fine structure splitting of La. On the other hand, including the first Rydberg shells ($7sp$, $6d$, and $5f$ in space **D**) in the correlation space significantly improves the ground state energy but does not show any major effect on the fine structure splitting. Figure 4.3 suggests that high energy virtual canonical orbitals are important contributions to the correlation energy but may not be critical in evaluating fine structure splittings of d-block elements.

For Y and La, X2C-SA-CASSCF calculations using a larger active space that is equivalent

to correlation space **B** produce fine structure splittings of 60 meV and 122 meV, respectively, compared to the results of 60 meV and 108 meV (Tab. 4.4) computed using X2C-MRCISD with a smaller active space reference and correlation space **B**. The improvement for La using a larger active space suggests that excited configurations beyond doubles can be important contributions to fine structure splittings of late-row elements.

4.4 Open-Shell Uranium(V)

Free $U(V)^{5+}$ ion has an open-shell valence electron configuration of $5f^1$, which splits into $^2F_{5/2}$ and $^2F_{7/2}$ levels due to spin-orbit coupling. The X2C-SA-CASSCF reference includes 1 electron and $5f$ shell (14 spinor orbitals in total) in the active space. Four different correlated spaces defined in Fig. 4.4 were used for X2C-MRCISD calculations. For these calculations, the SARC-DKH[110] all electron basis set is used for uranium.

	X2C-SA-CASSCF	X2C-MRCISD				Exp.[68]
		A	B	C	D	
$U(V)^{5+}$	974 (+3.3)	975 (+3.4)	974 (+3.3)	995 (+5.5)	989 (+4.9)	943

Table 4.5. Ground state fine structure splittings ($^2F_{5/2} - {}^2F_{7/2}$ in meV) of $U(V)^{5+}$. X2C-MRCISD calculations use various correlation spaces defined in Fig. 4.4 with a X2C-SA-CASSCF reference of 1 electron in 14 spinor orbitals.

The $^2F_{5/2} - {}^2F_{7/2}$ splitting is experimentally measured to be 943 meV.[68] The X2C-SA-CASSCF(1,14) result of 972 meV (3.1% error) is already in very good agreement with experiment, suggesting that the including static correlation in the f orbital space and spin-orbit coupling is sufficient for describing the fine structure splitting of uranium(V). Independent of the correlation space, additional dynamic correlation via the X2C-MRCISD procedure adds little improvement to the ground state ^2F fine structure splitting. The X2C-MRCISD results approach an asymptotic limit of 993 meV which seems worse than the X2C-SA-CASSCF value. This is likely due to the empirical Botteger factor used for two-electron spin-orbit coupling corrections which seems to underestimate the two-body coupling strength for f-block elements.

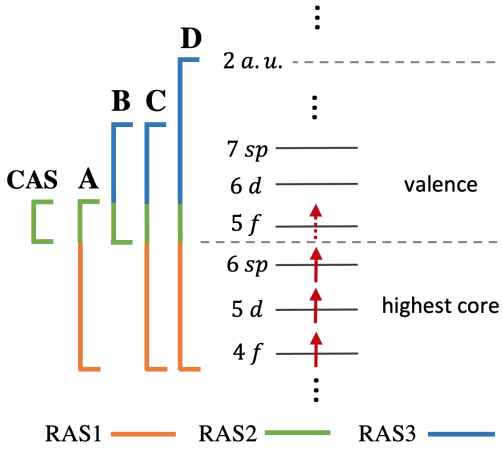

	X2C-SA-CASSCF	X2C-MRCISD			
		A	**B**	**C**	**D**
$U(V)^{5+}$	14	183,470	34	2,071,382	36,370,190

Figure 4.4. Top panel: definitions of selected correlation spaces. Orbital space is constructed from the X2C-SA-CASSCF reference, where solid and dotted arrows indicate fully and partially occupied orbitals, respectively. Note that virtual orbitals are ordered symbolically instead of energetically. **Bottom panel**: total numbers of two-component configurations in X2C-SA-CASSCF and X2C-MRCISD calculations.

Figure 4.5 plots the ground state energy and fine structure splitting as a function of the CI operator expansion. The X2C-MRCI correlation space used in this study includes $5d$, $5f$, $6d$, and $7sp$ orbitals. Both the ground state energy and fine structure splitting reach the asymptotic limit at the X2C-MRCISD level for the $U(V)^{5+}$ ion. Including higher-order excited configurations (*e.g.*, X2C-MRCISDT and X2C-MRCISDTQ) does not significantly improve either the ground state energy or the fine structure splitting. While X2C-MRCIS slightly improves the energy, it corrects the fine structure splitting by nearly 35% compared to that at the asymptotic limit.

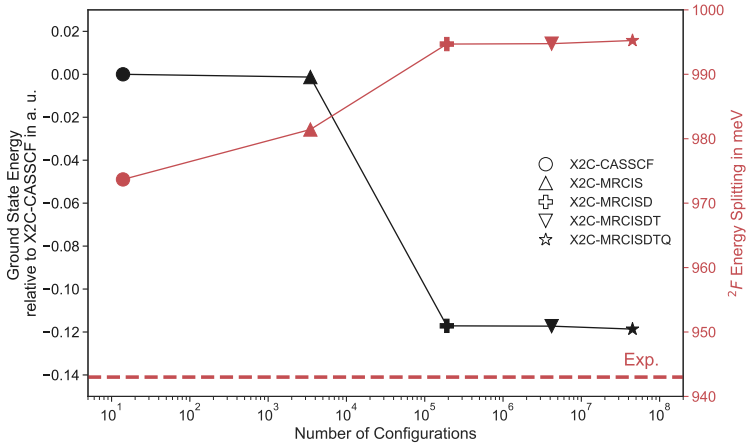

Figure 4.5. Dependence of X2C-MRCI ground state energies and fine structure splittings ($^2\mathrm{F}_{5/2} - {}^2\mathrm{F}_{7/2}$ in meV) of $\mathrm{U(V)}^{5+}$ on the operator expansions. The ground state energy relative to X2C-CASSCF and ^{2}F states energy splittings of $\mathrm{U(V)}^{5+}$. The correlation space used includes $5d$, $5f$, $6d$, and $7sp$ orbitals.

Chapter 5

MRCI APPLICATIONS ON RESOLVING L-EDGE X-RAY ABSORPTION SPECTRA (XAS) OF TRANSITION METAL COMPLEXES

One of the important application of the MRCI methods with energy specific Davidson solver is to resolve X-Ray spectra in transition metal complexes. In $L_{2,3}$ spectrum of first row transition metal complexes, it involves the excitation of an electron from the $2p$ to low-lying unoccupied orbitals. Within the MRCI framework, the core excitation could be build easily with $2p$ orbitals as RAS1 space, and the the low-lying unoccupied orbitals as RAS2 active space with up to single excitation allowed from RAS1 space (*i.e.*, $m_h = 1$). Additional dynamic correlation could be included with extra higher-energy virtual orbitals in RAS3 and extend more core orbitals in RAS1 with single and double excitations. The XAS of free iron cation (Fe^{3+}) as well as the analogs in tetrahedral ($FeCl_4^-$) and octahedral ($FeCl_6^{3-}$) ligand fields are investigated and compared to experiments and other theoretical work. This chapter is adapted with permission from: Andrew J. Jenkins, Hang Hu, Lixin Lu, Michael J. Frisch, and Xiaosong Li *J. Chem. Theory Comput.*, **2022**, 18(1), 141–150, [62]

5.1 Introduction

X-ray absorption spectroscopy (XAS) has been widely used to elucidate electronic and geometrical information of metals and metal complexes, as the spectra are highly element and state specific.[20, 105] Theoretical methods are key tools in understanding the experimental spectra. As X-ray absorption spectroscopy involves core electrons, theoretical methods that incorporate relativistic effects are vitally important for the understanding and prediction of

the spectra of even first-row transition metals.

K-edge XAS spectra (excitations from the 1s core level) demonstrate simple scalar relativistic effects, with *ab initio* calculations that neglect scalar relativistic effects red-shifting the absorption spectra compared to experiment[21, 91, 111, 44, 14]. L-edge X-ray spectroscopy measures electronic transitions from the $2p$ core orbitals. Like K-edge spectroscopy, L-edge XAS is also element specific, but offers some advantages over K-edge XAS. L-edge spectra have finer linewidths due to longer core-hole life-times, allowing for higher sensitivity. Additionally, spectral features in L-edge XAS are often more intense as transitions are electric dipole allowed. Interpretation and prediction of L-edge spectra is complicated by several factors, including significant relativistic and spin-orbit effects. In addition to scalar relativistic effects affecting the $2s$ and $2p$-orbitals, the spin and orbital angular momentum of an electron in the $2p$-orbital couple, causing a splitting of the $2p$ orbitals into two sets, $2p_{1/2}$ and $2p_{3/2}$, differing in total angular momentum J (1/2 and 3/2 respectively). This results in the X-ray absorption spectra containing two peaks corresponding to excitations from the two sets of p orbitals; these are known as the L_2 and L_3 edges, with the L_3 edge lower in energy. This fundamentally arises from the spin-orbit coupling. *Ab initio* calculations that neglect spin-orbit coupling predict a single peak. Furthermore, spin-orbit coupling in the d orbitals, ligand field splitting, and charge transfer states result in secondary features and spread the spectra over a range of energy, approximately 20 eV for iron containing systems.

The various theoretical and computational methods used to predict L-edge X-ray spectra have recently been reviewed in detail[67, 13, 12, 148]. The most rigorous way of including relativistic effects, spin-orbit coupling, and correlation effect is to solve the Dirac equation in a multiconfigurational framework, using either a four-component [64, 144, 3, 132, 8, 7, 76, 9, 50] or two-component wavefunction.[63, 58, 73, 41, 71, 72] Four-component methods are inherently demanding, therefore much effort has been made to decouple the four-component equations into electron only two-component equation, retaining the key physical relativistic effects of the full four-component equations, but at a reduced computational cost.

In this chapter, the exact two-component X2C method[88, 96, 112, 60, 97, 95, 131, 93,

113, 32, 47, 81, 33, 94] is used to decouple the four-component Dirac-Hartree-Fock into a reduced dimension electronic two-component approach. Relativistic and spin-orbit effects are variationally included at the orbital level in the X2C-Hartree-Fock reference. To account for the multi-configurational behaviour in the ground state of transition metals, we use an X2C state averaged complete active space self consistent field (X2C-SA-CASSCF) method in the Kramers' unrestricted framework.[63, 58] The use of multiconfigurational active space for the description of transition metals allows a natural extension to study their X-ray spectra. Using the restricted active space (RAS) formalism[109, 101], excitations can be made from specified core orbitals to the valence space; this has allowed the prediction of various X-ray spectra of transition metals, including K-edge, L-edge and resonance inelastic scattering[34, 49, 116, 117, 22, 16, 99, 66, 18]. In this chapter, the X2C multireference restricted active space configuration interaction (X2C-MRRASCI) approach is developed to predict the L-edge spectra of transition metals complexes.

5.2 Computational Details

The eigenvalues of the X2C-MRRASCI Hamiltonian matrix determine the energies of the excited states, *i.e.*, the peak position in the L-edge spectrum. We now define how to calculate the intensity of each transition. As stated above, the transition probabilities for L-edge spectra are electric dipole-allowed. Using the MO-dipole integrals, d^{ω}, for the Cartesian directions $\omega = \{x, y, z\}$, the oscillator strength for a transition between states 0 and n can be evaluated (within the dipole approximation)

$$\gamma_{pq}^{0n} = \sum_{IJ} (C_I^0)^* \ \langle I|E_{pq}|J\rangle \ C_J^n \tag{5.1}$$

$$D^{\omega,0n} = \left(\sum_{p,q} \gamma_{pq}^{0n}.d_{qp}^{\omega}\right).\left(\sum_{p,q} \gamma_{pq}^{n0}.d_{qp}^{\omega}\right) \tag{5.2}$$

$$|\mu|^2 = D^{x,0n} + D^{y,0n} + D^{z,0n} \tag{5.3}$$

$$f = \frac{2}{3}|\mu|^2.\Big(E_n - E_0\Big) \tag{5.4}$$

where $\hat{E}_{pq}$ is a single excitation operator, $|I\rangle, |J\rangle$ indicate determinants, C_J^n the coefficient of determinant $|J\rangle$ in state n and E_n the energy of state n. As the systems presented here have degenerate ground states, the oscillator strength is computed from each ground state and summed to give a total oscillator strength.

Primarily the variational inclusion of the relativistic effects and static correlations are considered by using X2C multireference restricted active space configuration interactions (X2C-MRRASCI), without further including dynamic correlations. For XAS calculations, the well-known d double-shell effect[115, 125] has been shown to only have a small effect on the spectrum[116].Accordingly, only one set of d orbitals may be included in the active space without significant loss in accuracy.

With the peak position and relative intensity determined, the spectrum is adjusted to account for both lifetime and experimental broadening. A Voigt convolution of a Lorentzian and a Gaussian is used. The Gaussian parameters are chosen to match the width of the main L_3 feature and represent broadening due to experimental resolution. Due to the difference in core-hole lifetimes between $p_{1/2}$ and $p_{3/2}$, separate Lorentzian broadening is applied to the L_3 and L_2 edges. A point equi-distance between the L_3 and L_2 edges separates the broadening regions. The total intensity is scaled such that the most intense L_3 peak has an intensity of 1.0. In addition, the computed spectrum is uniformly shifted to match the position of the most intense experimental peak. This shift is dependent on the specific active space and basis set used, but for the examples presented here lies in the range 11-15 eV. The character of the computed peaks can be determined from the X2C-MRRASCI density matrices for specific states and can be compared to any assigned peaks in the experimental spectrum. This aids in determining and validating the global shift but also allows analysis and understanding of the experimental spectrum.

5.3 The XAS of free Fe^{3+}

The benchmark calculations presented here focus on L-edge spectra of iron complexes. Therefore it is appropriate to first assess the performance of the X2C-MRRASCI procedure on the

free ion Fe^{3+}. The high spin ground state of Fe^{3+} is a six-fold degenerate $^6S_{5/2}$ state. These degenerate ground states can be described using X2C-SA-CASSCF, with an active space comprised of the d orbitals (5 electrons in 10 spinor orbitals) and state-averaging over the six states. This recovers the degeneracy of the states to within the energy convergence criteria. In order to compute the L-edge spectrum, a subsequent X2C-RASCI calculation is performed, using the *d* orbitals as the RAS2 space and the $2p$ orbitals as the RAS1 space, and allowing single excitations from RAS1. The computed spectrum, using a Sapporo-DKH3-DZP-2012 basis with diffuse functions[106], is shown in Fig. 5.1.

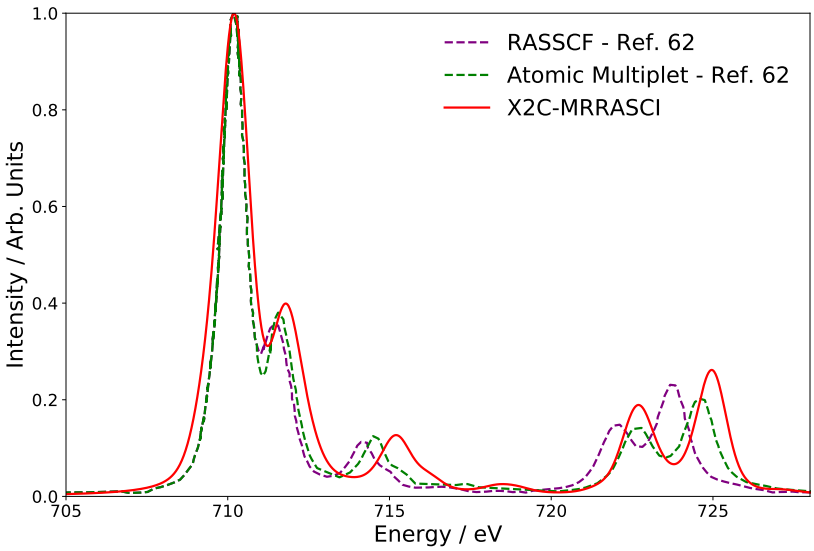

Figure 5.1. The $L_{2,3}$ edge of the XAS spectrum of Fe^{3+} computed using the X2C-MRRASCI procedure and compared to both the perturbative RASSI-RASSCF approach and semi-empirical atomic multiplet calculations of Pinjari *et al.* [118], reprinted from Pinjari, R. V.; Delcey, M. G.; Guo, M.; Odelius, M.; Lundberg, M. *Journal of Chemical Physics*, 2015, vol. 142, page 069901 with the permission of AIP Publishing. The computed spectra are shifted to align the most intense peak, and Voigt broadening applied.

The exact character of each peak of the spectrum has been analysed and discussed in detail[116, 118]. As expected, the most intense feature arises from $2p_{3/2} \rightarrow d$ orbitals, with shoulder peaks corresponding to different occupations of the *d* orbitals that are split by *d*

orbital spin orbit coupling, this is the L_3 region. The L_2 region, >720eV, corresponds to $2p_{1/2} \rightarrow d$. The spectrum computed using X2C-MRRASCI shows good agreement with literature predictions of the L-edge spectrum using RASSI-RASSCF and atomic multiplet calculations [118], and agrees with the character assigned in Ref. [118]. The three methods agree on the main features of the spectrum, but differ slightly in the relative energy spacing of the peaks. This difference in spacing is most obvious for the gap between the L_3 and L_2 regions, a direct result of the magnitude of the spin-orbit coupling in the $2p$ orbitals, with the energy gap being larger in X2C-MRRASCI.

5.4 The XAS of $FeCl_4^-$

In this sub-section, X2C-MRRASCI is used to compute the L-edge X-ray absorption spectrum of $FeCl_4^-$. In this molecule, the iron has an electronic configuration of $Fe(III) - d^5$. The ^6S ground state of a free ion splits in the tetrahedral ligand field of the Cl atoms to yield a $^6A_1$ ground state with an orbital occupancy of $e^2t_2^3$. The introduction of spin-orbit coupling further splits this into $E_{5/2}$ and $G_{3/2}$ states. Here, these lowest lying states are described by X2C-SA-CASSCF using 5 electrons in 10 spinor orbitals. As the $E_{5/2}$ and $G_{3/2}$ multiplets are degenerate within the accuracy requested here, state averaging over the 6 states of these multiplets is used.

In order to compute the absorption spectrum, the X2C-SA-CASSCF is used as a reference for X2C-RASCI computations. The X2C-SA-CASSCF active space is used as the RAS2 space, while the iron $2p$ orbitals and electrons comprise the RAS1 space. The computed spectrum is compared to the experimental spectrum[82] of $[Fe^{III}Cl_4](Et_4N)$ in Fig. 5.2.

In the computed spectrum, the relative positions of the peaks are reproduced; satellite peaks from 710 to 715 eV, two peaks in L_2. However, the intensity of the peak at 706 eV is overestimated. This peak corresponds to a transition from $p_{3/2}$ to a state of mixed e and t_2 occupation. The low-energy intensity (L_2) peak is overestimated in the computed spectrum, which might originate from the solvent effects present in experiment.

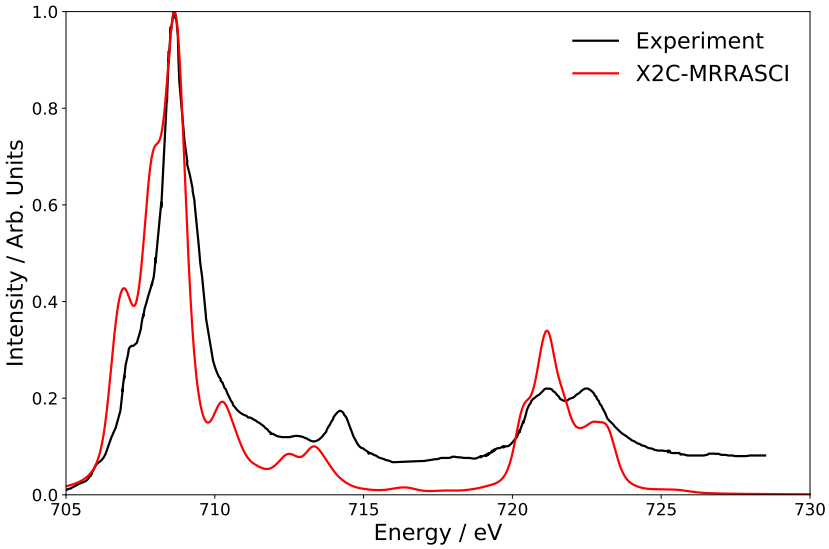

Figure 5.2. Comparison of the predicted and experimental[82] $L_{2,3}$ edge of the XAS spectrum of $FeCl_4^-$. The computed spectrum is shifted to align the most intense peak with experiment, and Voigt broadening applied. An ANO triple-zeta basis is used[114, 127]. Experimental data adapted with permission from Ref.[82], copyright 2017 American Chemical Society.

5.5 The XAS of $FeCl_6^{3-}$

In this section we test the X2C-MRRASCI method for the computation of the L-edge spectrum of $FeCl_6^{3-}$, a system that has been studied both experimentally[151] and theoretically[99, 22, 117, 116]. Furthermore, we investigate the effect of the RAS spaces on the result. In order to do this, we must fist understand the molecular orbitals. The bonding molecular orbitals of $FeCl_6^{3-}$ arise by ligand σ orbitals (symmetry adapted linear combination of p orbitals) mixing with Fe $3d$ orbitals to form bonding σ (and antibonding σ^*) orbitals of e_g symmetry. Additionally, weak bonding and anti-bonding orbitals are formed from the mixing of Fe t_{2g} orbitals with the $t_{2g}(\pi)$ orbitals formed from the ligand p orbitals.

The ground state of octahedral $FeCl_6^{3-}$ has a high spin electron configuration of $t_{2g}^3 e_g^2$. This gives a ^6A_g ground state. This degenerate ground state can be described by X2C-CASSCF using 5 electrons in the t_{2g} and e_g orbitals, state averaging over the six degenerate

micro-states of ^6A_g. This correctly gives six degenerate states, *i.e.*, a qualitatively correct set of states, using a minimal active space. These states are then used as a reference for the X2C-RASCI calculation of the L-edge spectrum.

In the molecular system, the L-edge spectrum corresponds to excitation from the $p_{1/2}$ and $p_{3/2}$ orbitals (of t_{1u} symmetry) to t_{2g} and e_g orbitals. Accordingly, the t_{1u} orbitals are included in the RAS1 space. The simplest RAS2 space, space A (shown in Fig. 5.3, is the same as the CAS space used in the orbital optimization and comprises 5 electrons in 10 orbitals (6 t_{2g} and 4 e_g).

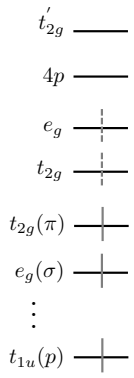

	A	B	C	D
RAS3	-	-	t'_{2g}	-
RAS2	t_{2g}, e_g	t_{2g}, e_g, $e_g(\sigma)$	t_{2g}, e_g, $e_g(\sigma)$	t_{2g}, e_g, $e_g(\sigma)$, t'_{2g}
RAS1	$t_{1u}(p)$	$t_{1u}(p)$	$t_{1u}(p)$	$t_{1u}(p)$

Figure 5.3. (**top**) Partial molecular orbital diagram for $FeCl_6^{3-}$. Orbitals fully occupied in the ground state are indicated by a solid line, while partial occupation is indicated by a dashed line. (**bottom**) Definition of the different RAS spaces (spaces A-D) used in the X2C-MRRASCI calculation on high spin $FeCl_6^{3-}$. All calculations use the same RAS1 space but differ in the composition of RAS2 and RAS3.

The computed L-edge spectrum is shown in comparison to experiment in Fig. 5.4. The results demonstrate that X2C-MRRASCI using only a limited active space satisfactorily reproduces the main experimental features of the spectrum. The experimental spectrum clearly shows the characteristic L-edge features but also shows a peak at $\sim$ 714 eV which has been assigned as a shake-up peak, corresponding to a $2p \rightarrow 3d$ transition coupled to

	RAS1	RAS2	RAS3	Determinants	States Computed
A	(6,6)	(5,10)	-	1512	900
B	(6,6)	(9,14)	-	8008	2500
C	(6,6)	(9,14)	(0,6)	419848	2000 (partial spectrum)

Table 5.1. Dimensions of the X2C-RASCI calculations on $FeCl_6^{3-}$. For each active space defined in Fig. 5.3, the number of electrons and spinor orbitals in each RAS sub-space is shown (*(electrons, orbitals)*). The resulting total number of determinants generated from these active spaces in X2C-RASCI is indicated in the 3rd column. The number of X2C-RASCI states actually computed, using an energy-specific Davidson procedure, for the $L_{2,3}$ spectrum in Fig. 5.4 is also given.

a $\sigma \rightarrow 3d$ ligand-metal-charge-transfer (LMCT)[151, 117]. This peak is not captured by calculation using space A, because excitation of the relevant σ orbitals is not allowed (they are not present in the active space).

In order to resolve the shake-up peak, the active space used was expanded. In space B, shown in Fig. 5.3, the σ orbitals are included. The computed spectrum, shown in Fig. 5.4, overestimates the overall intensity across the energy range, but importantly, shows the emergence of the LMCT peak when the σ orbitals are included. Furthermore, inclusion of the σ orbitals also gives rise to a higher energy satellite peak of the L_2 edge, a peak also predicted by Pinjari *et al.*[117], but not seen in the experimental data.

X2C-MRRASCI calculations using space B over-estimate the intensity of the shake-up peak compared to both experiment and the RASSI-RASSCF calculations of Pinjari *et al.*[117]. To investigate the source of this over-estimation, the $t_{2g}^{'}$ orbitals identified to play an important role in correlation[116, 117] have been included in RAS3 to act as correlating orbitals (see space 'C' in Fig. 5.3). However, the computed spectrum changes very little (see Fig. 5.4), showing the same over-estimation of the shake-up peak compared to experiment and RASSI-RASSCF. This suggests that orbital relaxation effects, as allowed in the RASSI-RASSCF calculations of Ref. [117], may be more important for describing this shake-up peak.

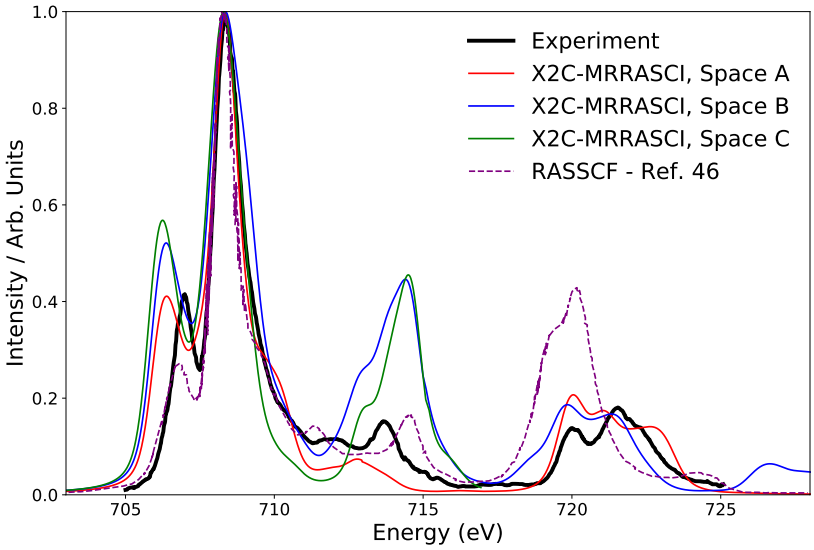

Figure 5.4. Comparison of the predicted and experimental $L_{2,3}$ edge of the XAS spectrum of $FeCl_6^{3-}$, using different active spaces A-C and an ANO triple-zeta basis[114, 127](note that the spectrum using Space C is not computed beyond 717 eV). Computed spectra have been broadened and shifted (see main text). Also shown is the perturbative RASSI-RASSCF spectrum of Pinjari *et al.*[117] that use space 'D' in Fig. 5.3 (see Ref.[117] for details). RASSI-RASSCF spectrum reprinted with permission from Pinjari, R. V.; Delcey, M. G.; Guo, M.; Odelius, M.; Lundberg, M. *Journal of Computational Chemistry*, vol 37, page 477, copyright 2016 Wiley publishing. Experimental data adapted with permission from Ref.[151], copyright 2003 American Chemical Society.

5.6 Conclusion

In this work we present X2C-MRRASCI, a combined X2C-SA-CASSCF and X2C-RASCI approach for the computation of L-edge X-ray absorption spectra. This approach allows for variational inclusions of relativistic effects and spin-orbit couplings at the molecular orbital level. The procedure is benchmarked for the L-edge spectra of iron complexes.

Results show that even with a minimal active space, key features of the absorption spectrum are captured. Although two-electron spin-orbit coupling is only approximated using an empirical scaling of the one-electron coupling, results show accurate separation of the L_3 and L_2 edges.

The use of small active spaces leads to a lack of dynamic correlation, which is likely to affect the relative intensities of the peaks in the systems we have studied but not the qualitative features, which are the focus of this work. Careful studies using larger active spaces are likely to resolve the overestimation of the intensity of low-energy transitions seen in each spectrum. Similar studies have already shown the significant effects of expanding the active space and adding perturbative corrections for dynamic correlation, particularly on the L_2 edge[22, 117]. However, the calculations on $FeCl_6^{3-}$ presented here do not suffer from large over-estimation of the intensities of the L_2 edge but rather over-estimate the shake-up peak. Expanding the active space to account for leading dynamic correlations, and to allow easier comparison to literature, shows little improvement over existing spaces used, suggesting orbital relaxation after core-excitation, as allowed in the RASSCF calculations of Ref. [117], may play an important role in the prediction of accurate intensities for these transitions. This effect warrants further development and investigation.

Perturbative spin-orbit coupling approaches have shown similar performance for early transition metals, however, a variational approach is likely to vital as the magnitude of the spin-orbit coupling is increased, for example, as one studies elements further down the periodic table. Through careful choice of the RAS spaces, the X2C-MRRASCI method detailed here may be used for further X-ray absorption studies, including M-edge, providing a useful analysis and predictive tool.

Chapter 6

MRCI APPLICATIONS ON STUDYING NON-RADIATIVE DECAY PATHWAYS OF ELECTRONICALLY EXCITED/IONIZED MOLECULES

In this chapter, the weakly coupled Ethane-Rare Gas (RG = Ar, Kr or Xe) dimers will be used as an example to demonstrate the computational flow using multi-reference methods to probe the non-radiative decay of energized electronic systems. This chapter is adapted with permission from: Sramana Kundu, Hang Hu, Xiaosong Li, Micah Schaible, and Thomas M. Orlando *J. Chem. Phys.*, **2023**, 158(12), 03 , Copyright ©2023 American Chemical Society.[86]

6.1 Introduction

Reactions caused by impact of photons or energetic particles (electrons, ions) occur under non-equilibrium conditions. Many-body interactions can affect and determine the effective energy exchange pathways, which ultimately determine the final physical and chemical state(s) of the target(s). Broadly speaking, the study of non-equilibrium processes is important in surface science [153, 10, 89, 11, 147, 83], radiation chemistry [2, 103, 87, 129], environmental science [104, 102, 65] and astrochemistry [100]. Following an ionization event, charge transfer between neighboring entities in the target is an important step in the propagation of the excess energy in the medium. Indeed, charge-transfer reactions between simple and complex collision partners, such as rare gas cations and simple hydrocarbons have been extensively studied in gas phase using crossed beam, flowing afterglow (FA), selected–ion–flow–drift–tube (SIFDT), and ion trapping methods. [54, 53, 146, 120] Most of these studies were done at thermal energies. This simplifies the interpretation of the results

since no additional kinetic energy above the recombination energy of the reactant ion is available. The general conclusion from these studies is that a resonant charge transfer is dominant, i.e. the energy levels of the product molecular ions most likely to be populated are those lying closest to the recombination energy of the reactant ion. [53, 146, 120] It can be expected that the strength of the Franck-Condon overlap between the rare gas cation and target molecule potential energy levels determine the efficiency of charge transfer [146], which would further affect the extent of fragmentation of the molecular cation in different rare gas systems. Depending on the inter-nuclear distance between the rare gas and molecule, non-adiabatic couplings could affect the transfer probability [51]. When the excitation energy is increased well above the ionization potential, in addition to the single-particle charge or hole transfer processes, complicated multi-electron/multi-hole interactions occur. These will follow deep valence, shallow core and deep core excitations and ionization. Gas and condensed phase cluster studies have revealed pronounced differences due to bonding geometry changes, and many body effects.[135, 123, 36, 150, 56] Energy exchange processes such as interatomic and intermolecular Coulomb decay (ICD) and electron transfer mediated decay (ETMD) have also been observed and studied in detail recently with very high time and energy resolution in weakly bonded systems, [123, 52, 26, 84, 122, 37, 130, 61] predominantly in the gas-phase. Such events can also be studied in weakly coupled adsorbed atoms and molecules [48], providing the opportunity to directly examine the fundamentals of single and multi-hole charge transfer in restricted geometries and energetics that are defined by the condensed rare gas atom and molecule identities. Since ionizing radiation and the subsequent Auger cascade events produce secondary electrons, the inelastic scattering losses of the secondary electrons contribute significantly to the ultimate energy deposition and exchange processes in samples under high energy or non-equilibrium conditions. A simple approach to directly examine this is via the use of a tunable electron beam to examine single- and multi-hole processes resulting from valence, as well as shallow and deep core level excitation. In addition, for condensed targets, dissociation and desorption induced by electronic transitions occur when such surfaces and interfaces are irradiated with essentially any type

of ionizing radiation. Examples include surface modification processes in the laboratory to the chemistry occurring in cold dust grains in the interstellar medium.[2, 1, 6, 90, 17, 155, 4] Depositing sub-monolayer quantities of the target species on several layer-thick rare gas substrates prepared at cryogenic temperatures is a useful method to study the species in the condensed phase. This overcomes the issue of quenching of electronic excitations in species directly adsorbed on metals due to interactions with the metal substrate. The rare gas layer confines the electronic excitations in adsorbates long enough for the relevant ionization and dissociation pathways to occur. [25, 138, 137] Rare gases are structurally simple, chemically inert and their physical and electronic properties are relatively well-known. The mechanism of electronic excitation leading to cation desorption from surfaces of condensed gases is not yet fully understood. Others have explained it in terms of Coulomb repulsion between localized valence holes.[138, 139, 69, 70] These experiments, however, were conducted at high incident electron energies (> 500 eV), and may not fully reveal the energy exchange and desorption processes, particularly near threshold desorption energies. Though there are limited studies of near-threshold desorption processes for simple systems,[6, 28, 55, 77, 121, 78], few involve complex heterogeneous molecular targets. It has been seen earlier when an organic cation mixed with a rare gas was deposited and irradiated with MeV electrons, the reaction channel changed from fragmentation to deprotonation on going from argon to xenon, with krypton showing a mixture of channels[38]. Also, it has been suggested that the extent of localization of the hole in the outermost p orbital of the rare gas following ionization, affects the extent of H+ scattering on condensed rare gas surfaces[136]. Depending on the protic or aprotic nature of the adsorbate molecule, the ions observed following ESD are clusters of protonated intact molecules or fragments of parent molecules [139]. In this study, cations generated by tunable low-energy electron bombardment of condensed ethane (C2H6), the simplest hydrocarbon with C–C and C–H bonds, deposited on different rare gases – argon, krypton and xenon – reveal how the energy (hole or charge) exchange and subsequent fragmentation and desorption processes occur and the probable importance of ICD and ETMD processes in the interfacial energy exchange events in weakly interacting condensates.

6.2 *Non-radiative Decay Channels in Ethane-Rare Gas Mixture*

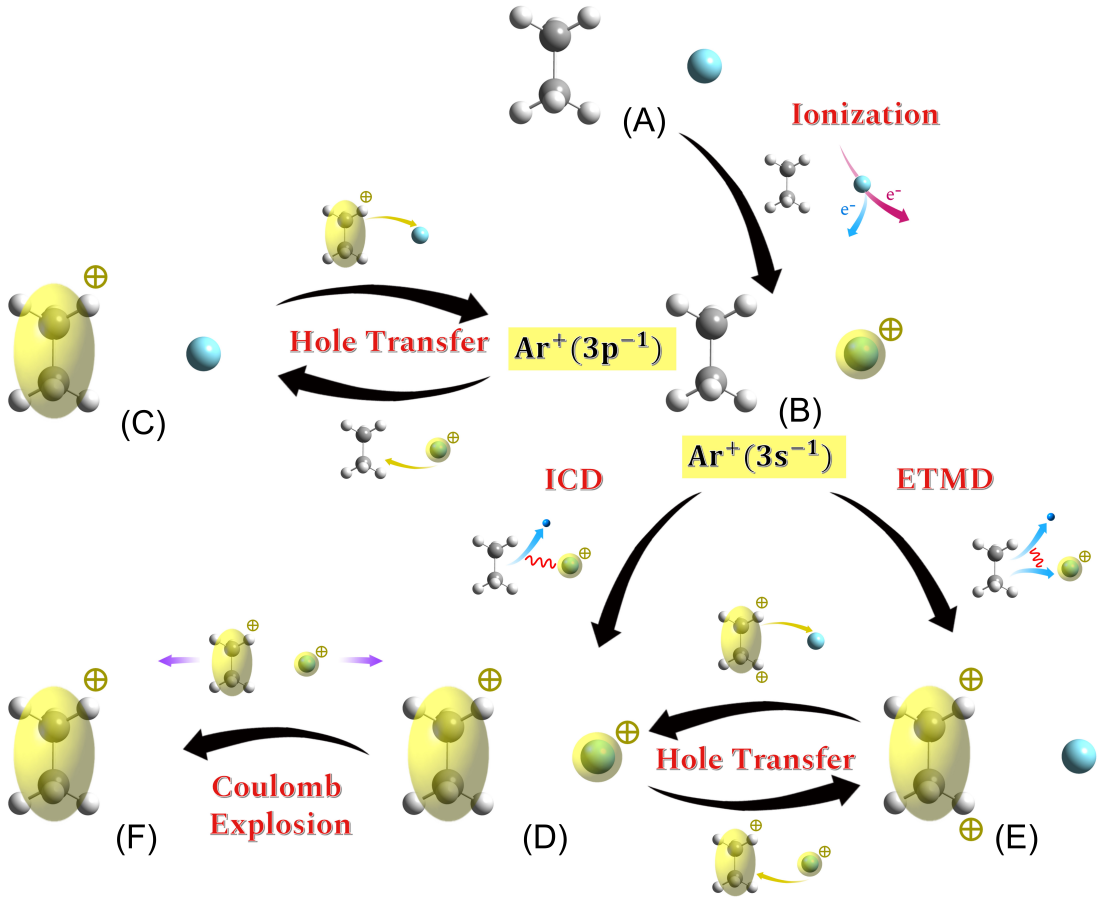

Figure 6.1. Schematic mechanisms of the possible nonradiative decay channels in Ethane-Ar dimer upon electron ionization. Direct ionization of neutral Ethane-Ar dimer (A) creates a shallow (Ar $3p$) or deep (Ar $3s$) single core hole state (B). For shallow hole state Ethane$-$Ar$^{+}(3p^{-1})$, it can resonate with single hole state Ethane$^{+}-$Ar (C) via hole transfer. For deeper hole state Ethane$-$Ar$^{+}(3s^{-1})$, ICD and ETMD could happen and leads to double hole state Ethane$^{+}-$Ar^{+}(D) and Ethane$^{++}-$Ar (E) respectively. The resulted double hole state from ICD and ETMD can also resonate with each other via hole transfer. The double hole states can experience strong coulomb repulsion, either leading to uncoupled single hole state on Ethane (F) or direct fragmentation.

The important energy decay pathways as the result of the shallow or inner core electron ionization of the Ar atom in Ethane$-$Ar dimer are illustrated in Fig. 6.1 and Fig. 6.2. Electron or photon irradiation can directly ionize the core level of Ar $3p$ or Ar $3s$ and

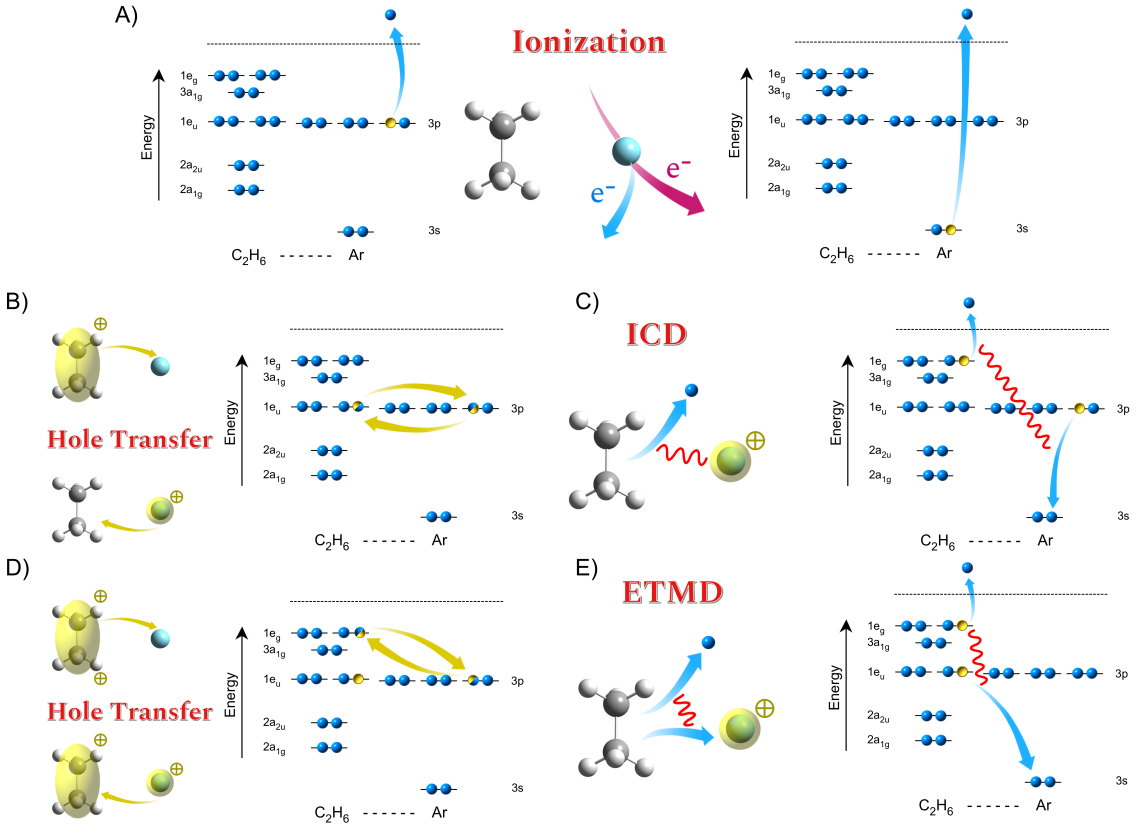

Figure 6.2. A) Electron ionization process, where an electron on Ar $3s$ or $3p$ level is ionized and a single hole state is formed; B) Resonant hole transfer between single hole states Ethane$-$Ar$^+$ and Ethane$^+-$Ar; C) Interatomic coulomb decay of single hole state Ethane$-$Ar$^+(3s^{-1})$; D) Resonant hole transfer between double hole states Ethane$^+-$Ar$^+$ and Ethane$^{++}-$Ar; E) Electron-transfer-mediate decay of single hole state Ethane$-$Ar$^+(3s^{-1})$

leave the system as a single hole state (Fig. 6.2A). Subsequently, for shallow single hole state $Ar^+(3p^{-1})$, it can resonate with the hole state $EtH^+(1e_u^{-1})$, due to their close energy levels (Fig. 6.2B); for deeper single hole state $Ar^+(3s^{-1})$ could be relaxed and results in the ionization of the nearby Ethane molecule via ICD ((Fig. 6.2C) or ETMD ((Fig. 6.2E). If the energy level of final state after the ICD and ETMD aligned closely, they can become resonant and interchange between each other via hole transfer (Fig. 6.2D). With a single hole (Fig. 6.1C/F) or double holes (Fig. 6.1E) localized on Ethane molecule, fragmentation could occur to form cations such as CH_3^+, $C_2H_4^+$, and etc. For Kr and Xe, the overall possible

channels should be similar with some of them being inaccessible when the energy levels are not aligned.

Experimentally, to probe above non-radiative decay pathways, Ethane or Ethane-RG mixtures were deposited on a clean gold-plated copper substrate and exposed to controlled low-energy electron irradiation in an ultrahigh vacuum chamber with a time-of-flight mass spectrometer (TOFMS). Fig. 6.3A-C shows the mass spetra of pure Ethane under electron irradiation, where the dominant cation product is CH_3^+ and small yield of $C_2H_n^+$ cations appear only in higher energy range (> 25 eV). When rare gas atoms are introduced in the system, $C_2H_n^+$ cations starts to appear at lower energy range ($15 - 17$ eV) and the yield of all cations increases across the probed energy range. Note that the yields of cation fragments follows the trends of Ar, Kr and Xe within the whole probed range of energy levels ($20 - 50$ eV).

6.3 Accurate Descriptions on the Energy Levels of the Hole States

All the non-radiative pathways presented in Fig. 6.1 are can be summarized in the form of reaction equations:

$$\text{single hole state resonance:} \qquad \mathrm{EtH^+ + RG \rightleftharpoons EtH + RG^+} \tag{6.1}$$

$$\text{ICD:} \qquad \mathrm{EtH + RG^+ \rightarrow EtH^+ + RG^+ + e^-} \tag{6.2}$$

$$\text{ETMD:} \qquad \mathrm{EtH + RG^+ \rightarrow EtH^{++} + RG + e^-} \tag{6.3}$$

$$\text{double hole state resonance:} \qquad \mathrm{EtH^+ + RG^+ \rightleftharpoons EtH^{++} + RG} \tag{6.4}$$

As all of the chemical processes are energy-conserved processes, it is important to depict the energy levels of each state accurately and obtain the whole energy landscape of the energized electronic systems.

To establish a computational work flow for core-hole state energy level and benchmark the accuracy of multi-reference methods, monomer calculations on single hole states of either single rare gas atom or single Ethane molecule is performed. The aug-cc-pVDZ basis [29] are

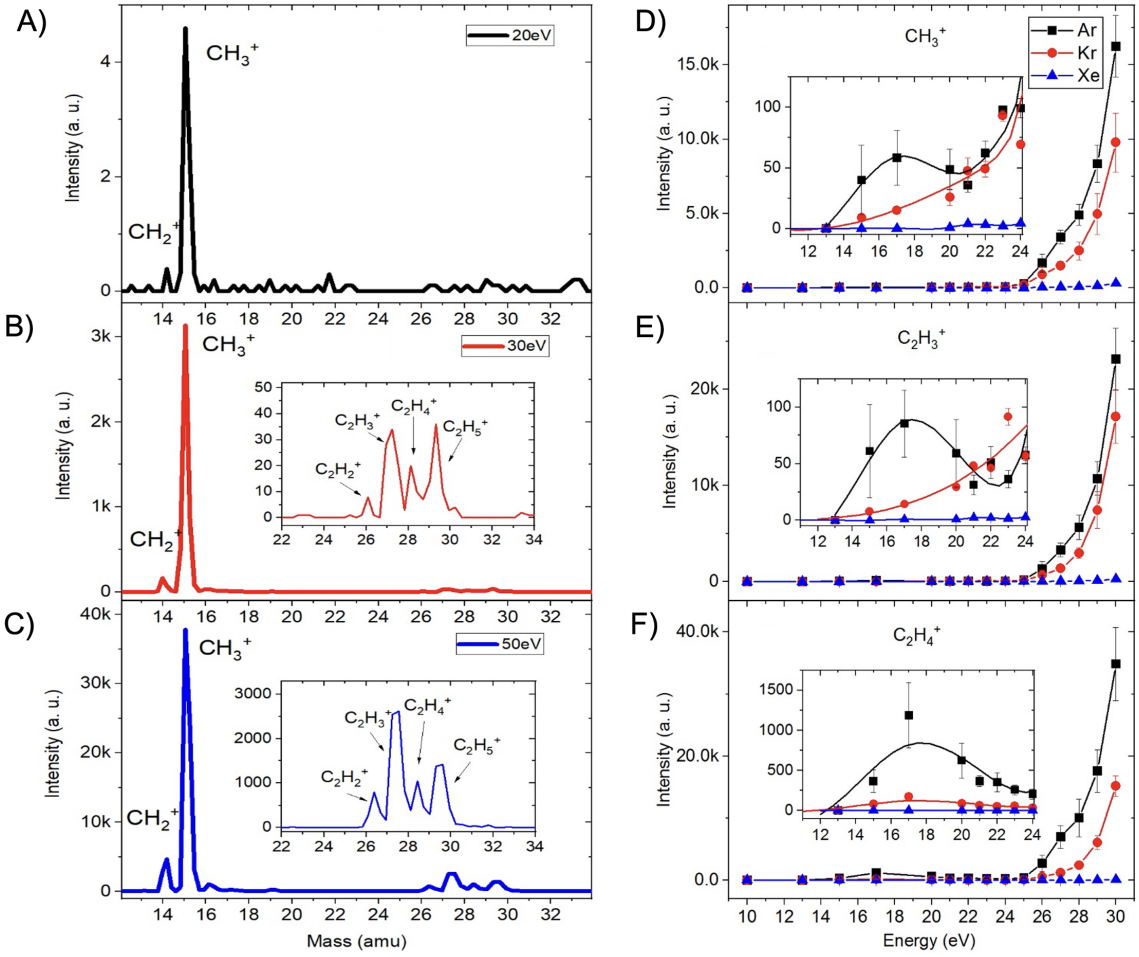

Figure 6.3. Experimental mass spectra of pure Ethane under electron irradiation of A) 20 eV, B) 30 eV, C) 50 eV. The fragmental intensity of D) CH_3^+, E) $C_2H_3^+$, F) $C_2H_4^+$ as a function of electron energy in Ethane-rare gas mixtures.

used for all the monomer benchmark calculations in this section while aug-cc-pVTZ basis is used for dimmer calculations. CASSCF and MRCISD (including single and double excitation to virtual space) in one-component framework are used, where the active space is chosen as the minimal active space including all the valence molecular orbitals (ns, np from rare gas atoms and $1e_g$, $3a_{1g}$, $1e_u$, $2a_{2u}$, $2a_{1g}$ from Ethane). The single core state are created by removing an electron from the fully filled CAS in neutral, and state averaging is used over all single core hole states during CASSCF. Scalar relativistic effects are included whenever Xe

atom is presented in the calculations, while in other cases, the non-relativistic Hamiltonian is used.

The energy levels of the core-hole states comes from the difference between a cation calculation and their neutral analog. Thus, only calculations treated with same level of theory and correlated space (i.e. similar electron correlation) are meaningful. In this perspective, two approaches at the level of CASSCF/HF and MRCISD/CISD are proposed:

$$\text{low accuracy and low computational cost: } E^{\text{core-hole}} = E^{\text{cation}}_{\text{CASSCF}} - E^{\text{neutral}}_{\text{HF}} \tag{6.5}$$

$$\text{high accuracy and high computational cost: } E^{\text{core-hole}} = E^{\text{cation}}_{\text{MRCISD}} - E^{\text{neutral}}_{\text{CISD}} \tag{6.6}$$

The result of rare gas atoms and single Ethane molecule are presented in Tab. 6.1 and Tab. 6.2. At the levels of CASSCF/HF, the energy of shallow hole states are better descried than the deep hole states compared to experimental data due to the lack of dynamic corrections. The deeper level of the core hole state are all overestimated $1 \sim 4$ eV. Once including the virtual orbitals for dynamic correction treatment at the level of MRCISD/CISD, accurate descriptions of the core-hole states (with error less than 1 eV) could be obtained.

Energy Levels	Experimental	$E^{\text{cation}}_{\text{CASSCF}} - E^{\text{neutral}}_{\text{HF}}$	$E^{\text{cation}}_{\text{MRCISD}} - E^{\text{neutral}}_{\text{CISD}}$
Ar^+ $3p^{-1}$	15.80	14.79 (−1.01)	15.47 (−0.33)
Ar^+ $3s^{-1}$	29.20	33.21 (+4.01)	29.98 (+0.78)
Kr^+ $4p^{-1}$	14.00	13.33 (−0.67)	13.85 (−0.15)
Kr^+ $4s^{-1}$	27.45	30.22 (+2.77)	27.07 (−0.38)
Xe^+ $5p^{-1}$	12.10	11.66 (−0.44)	12.14 (−0.04)
Xe^+ $5s^{-1}$	23.31	26.47 (+3.16)	23.67 (+0.36)

Table 6.1. Energy levels of valence and inner-valence hole on Ar, Kr and Xe atoms from experiments [143] and multi-reference calculations. CAS(7,4) is chosed as the active space for CASSCF, and all core are frozen and all virtual were used in MRCISD and CISD calculations. The singed errors of computational results are included in the parentheses.

With the knowledge from above benchmark tests, two dimer models are constructed, where the rare gas atom is placed perpendicular to the Ethane C-C bond axis (Fig. 6.4A) or along the Ethane C-C bond axis (Fig. 6.4B). The equilibrium geometry of neutral dimer in

Energy Levels	Experimental	$E^{\text{cation}}_{\text{CASSCF}}$ - $E^{\text{neutral}}_{\text{HF}}$	$E^{\text{cation}}_{\text{MRCISD}}$ - $E^{\text{neutral}}_{\text{CISD}}$
$1e_g^{-1}$	12.25	12.52 (+0.27)	12.59 (+0.34)
$3a_{1g}^{-1}$	13.35	12.19 (−1.16)	12.73 (−0.62)
$1e_u^{-1}$	15.45	15.31 (−0.14)	15.27 (−0.19)
$2a_{2u}^{-1}$	21.0	22.09 (+1.09)	21.09 (+0.09)
$2a_{1g}^{-1}$	24.5	26.29 (+1.79)	24.82 (+0.32)

Table 6.2. Energy levels of valence and inner-valence hole on Ethane monomer from experiments [23] and multi-reference calculations. CAS(15,7) is chosed as the active space for CASSCF, and all core are frozen and all virtual were used in MRCISD and CISD calculations. The singed errors of computational results are included in the parentheses.

both layouts are obtained with long-ranged corrected density function theory (Cam-B3LYP) and 6-31++g(d,p) basis and used in the following calculations. For dimer calculations, localized orbitals coming from fragment HF were used to ensure the calculations are performed in the basis of diabatic state determinants (localized hole on either part of the dimer).

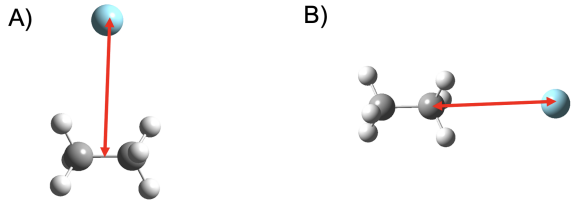

Vertical Layout Horizontal Layout

Dimer	Equilibrium Separation in A ($\mathring{A}$)	Equilibrium Separation in B ($\mathring{A}$)
Ethane − Ar	3.89	3.89
Ethane − Kr	4.10	4.16
Ethane − Xe	4.50	4.54

Figure 6.4. Top panel: Geometries of Ethane and rare gas dimers considered in the computational study. **Bottom panel**: The equilibrium separation between neutral Ethane and neutral rare gas atom under the level of Cam-B3LYP/6-31++g(d,p).

The energy levels of the shallow hole states at the level of CASSCF/HF are depicted in Fig. 6.5, and which are slightly higher than their monomer levels. The nearly perfect

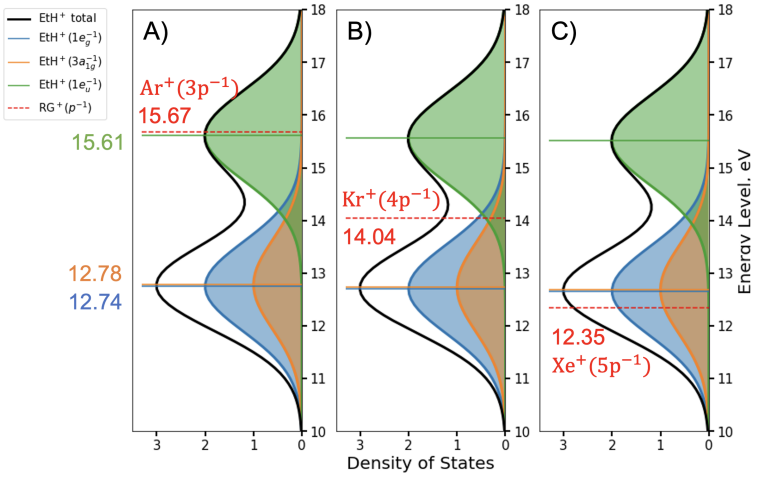

Figure 6.5. Density of state plot of single shallow hole states in Ethane-RG dimer model at the level of CASSCF. The reference neutral energy level is computed as HF energy.

alignment of $Ar^+(3p^{-1})$ level with $EtH^+(1e_u^{-1})$ level might explain the largest increase of the fragments in lower energy level ranges (see Fig. 6.3). For $Kr^+(4p^{-1})$, although it is not near either of the Ethane shallow hole level, it could access all three channels. As for $Xe^+(5p^{-1})$, it could resonate with both $EtH^+(1e_g^{-1})$ and $EtH^+(3a_{1g}^{-1})$ states. Without computing the electronic coupling matrix elements, it is impossible to even qualitatively explain the yield trends among the three systems.

The energy levels of the shallow hole states at the level of CASSCF/HF are presented in Fig. 6.6. For ICD or ETMD process, since the ionized electron (see Eq. (6.2) and Eq. (6.3)) will carry kinetic energies, the pathway only exists when the initial single hole state has higher energy level than the final double hole state. Thus from the Fig. 6.6, it seems that strong ICD and ETMD channels are found in Ethane-Ar dimer, while only ICD channels are open in Ethane-Kr or Ethane-Xe dimer. However, from the monomer benchmark tests, the energy landscape especially for the single deeper hole states need to be corrected at the level of MRCISD/CISD before final conclusion could be draw.

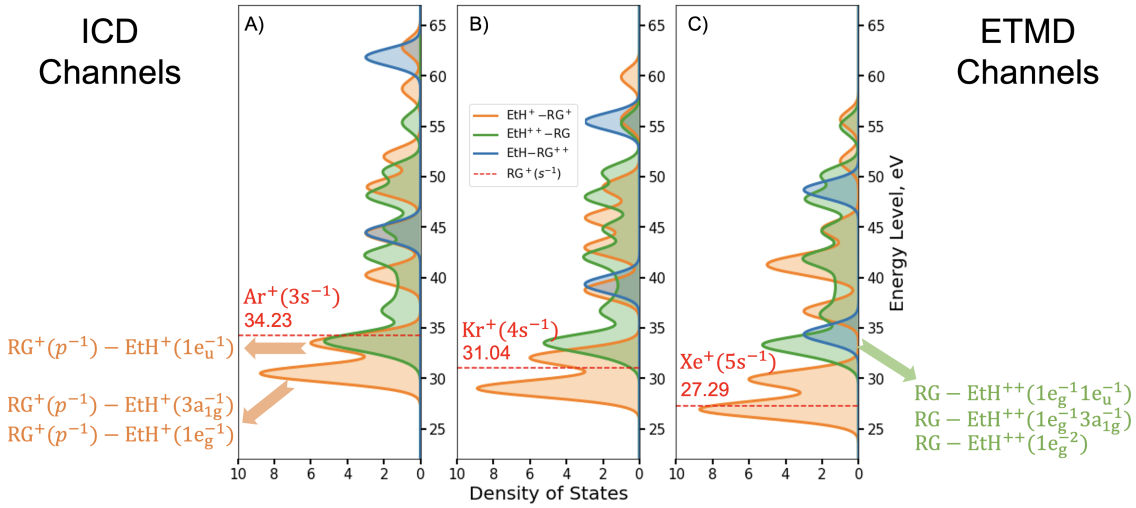

Figure 6.6. Density of state plot of single deep hole states and double hole states in Ethane-RG dimer model at the level of CASSCF. The reference neutral energy level is computed as HF energy.

6.4 Computation of Electronic Coupling Matrix Element

From Fermi's golden rule [24, 39], the probability of a non-radiative pathway is proportional to the square of strength of the coupling matrix elements (CMEs) between the initial state $|\Psi_i\rangle$ and the final state $|\Psi_f\rangle$ as:

$$\Gamma \sim |\langle \Psi_f | \hat{V} | \Psi_i \rangle|^2 \tag{6.7}$$

where $\hat{V}$ is coupling potential operator. An attempt for explanation on the yield trend of the cation fragments in Ethane-RG mixture is to seek computational approach of such electronic CMEs. Use the framework of the CASSCF and MRCI, it is straightforward to obtain the wavefunction of diabatic initial/final states and their CMEs. Fig. 6.7 is an example of computing CMEs of single hole state resonance (via hole transfer) at the level of CASSCF.

The electronic CMEs at the level of CASSCF of single hole and double hole states resonance are computed as Tab. 6.3 and Tab. 6.4, respectively. For single core-hole resonance, the

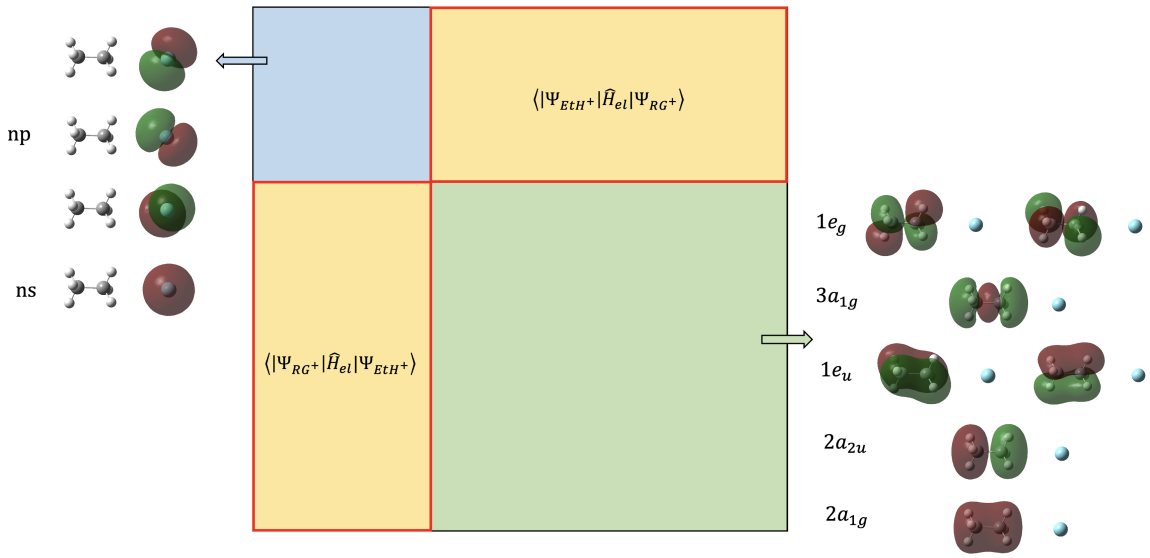

Figure 6.7. Schematic computations of the coupling matrix element at the level of CASSCF, for single hole state resonance via hole transfer. The Electron Hamiltonian is construct with the basis of diabatic state determinants and grouped by Ethane$-Ar^+$ as upper diagonal sub-block and Ethane$^+-$Ar as lower diagonal sub-block. Sub-block diagonalization is performed and Hamiltonian is transformed to give the coupling matrix element of $\langle \Psi_{\mathrm{RG}^+} | \hat{H}_{el} | \Psi_{\mathrm{EtH}^+} \rangle$ as the off-diagonal block.

	Vertical Layout		
	$Ar^+(3p^{-1})$	$Kr^+(4p^{-1})$	$Xe^+(5p^{-1})$
$EtH^+(1e_g^{-1})$	5.60×10^{-3}	4.65×10^{-3}	2.78×10^{-3}
$EtH^+(3a_{1g}^{-1})$	4.08×10^{-4}	2.24×10^{-4}	4.40×10^{-4}
$EtH^+(1e_u^{-1})$	6.90×10^{-3}	5.46×10^{-3}	2.95×10^{-3}
	Horizontal Layout		
	$Ar^+(3p^{-1})$	$Kr^+(4p^{-1})$	$Xe^+(5p^{-1})$
$EtH^+(1e_g^{-1})$	2.16×10^{-3}	1.74×10^{-3}	9.78×10^{-4}
$EtH^+(3a_{1g}^{-1})$	5.93×10^{-3}	5.07×10^{-3}	3.19×10^{-3}
$EtH^+(1e_u^{-1})$	5.93×10^{-4}	7.31×10^{-4}	3.41×10^{-4}

Table 6.3. The electronic CMEs (in *a.u.*) of single hole states resonance at level of CASSCF. The contribution from degenerate states is computed as the square root of the summed square CMEs.

CMEs follow the same trend as the yield of the cation fragments in Fig. 6.3. The $RG^+(np^{-1})$ hole state couples strongly with the $EtH^+(1e_g^{-1})$ and $EtH^+(1e_u^{-1})$ levels in thg vertical layout of the dimer, while it couples strongly with the $3a_{1g}^{-1}$ level in horizontal layout. This could be expected from the spatial geometry of the hole densities, where larger hole density overlap gives stronger CMEs. For double-hole resonance, the results are similarly with the strongest coupling comes between $EtH^{++}(1e_g^{-1}1e_u^{-1})$ and $RG^+(np^{-1})$−$EtH^+(1e_u^{-1})$. As those results is at the level of CASSCF, the influence of dynamic correlation remains to be explored using MRCISD calculations in the future.

	Vertical Layout		
	$Ar^+(3p^{-1})$−$EtH^+(1e_u^{-1})$	$Kr^+(4p^{-1})$−$EtH^+(1e_u^{-1})$	$Xe^+(5p^{-1})$−$EtH^+(1e_u^{-1})$
$EtH^{++}(1e_g^{-2})$	3.98×10^{-3}	3.11×10^{-3}	2.01×10^{-3}
$EtH^{++}(1e_g^{-1}3a_{1g}^{-1})$	1.52×10^{-3}	9.72×10^{-4}	4.57×10^{-4}
$EtH^{++}(1e_g^{-1}1e_u^{-1})$	4.81×10^{-3}	3.11×10^{-3}	1.43×10^{-3}
	Horizontal Layout		
	$Ar^+(3p^{-1})$−$EtH^+(1e_u^{-1})$	$Kr^+(4p^{-1})$−$EtH^+(1e_u^{-1})$	$Xe^+(5p^{-1})$−$EtH^+(1e_u^{-1})$
$EtH^{++}(1e_g^{-2})$	8.07×10^{-5}	9.65×10^{-5}	4.78×10^{-5}
$EtH^{++}(1e_g^{-1}3a_{1g}^{-1})$	1.34×10^{-3}	2.07×10^{-3}	6.52×10^{-4}
$EtH^{++}(1e_g^{-1}1e_u^{-1})$	1.18×10^{-3}	2.37×10^{-3}	3.05×10^{-4}

Table 6.4. The electronic CMEs (in *a.u.*) of double hole states resonance at level of CASSCF.The contribution from degenerate states is computed as the square root of the summed square CMEs.

While the CMEs of the hole states resonance can be directly obtained after a multi-reference calculation, those of ICD and ETMD is more difficult as the ionized electron (with kinetic energies) requires special treatment. One approach to approximate the process is to excite the hole electron into a pseudo-continuum represented by diffuse functions [5] . Once proper diffuse functions are set in the calculation, the CMEs between a deep core hole state and two hole one particle (2h1p) state would be easily extracted in the smilar fashion of 6.7 from our MRCI framework.

BIBLIOGRAPHY

[1] Mustafa Akbulut, Norbert J. Sack, and Theodore E. Madey. Elastic and Inelastic Processes in the Interaction of 1–10 eV Ions with Solids: Ion Transport through Surface Layers. *Surface Science Reports*, 28(7):177–245, 1997.

[2] Elahe Alizadeh, Thomas M. Orlando, and Léon Sanche. Biomolecular Damage Induced by Ionizing Radiation: The Direct and Indirect Effects of Low-Energy Electrons on DNA. *Annual Review of Physical Chemistry*, 66(1):379–398, 2015.

[3] Adel Almoukhalalati, Stefan Knecht, Hans Jørgen Aa. Jensen, Kenneth G. Dyall, and Trond Saue. Electron Correlation within the Relativistic No-pair Approximation. *Journal of Chemical Physics*, 145(7):074104, 2016.

[4] Christopher R. Arumainayagam, Hsiao-Lu Lee, Rachel B. Nelson, David R. Haines, and Richard P. Gunawardane. Low-energy Electron-induced Reactions in Condensed Matter. *Surface Science Reports*, 65(1):1–44, 2010.

[5] Vitali Averbukh and Lorenz S. Cederbaum. Ab Initio Calculation of Interatomic Decay Rates by a Combination of the Fano Ansatz, Green's-Function Methods, and the Stieltjes Imaging Technique. *Journal of Chemical Physics*, 123(20):204107, 2005.

[6] Phaedon Avouris and Robert E. Walkup. Fundamental Mechanisms of Desorption and Fragmentation Induced by Electronic Transitions at Surfaces. *Annual Review of Physical Chemistry*, 40(1):173–206, 1989.

[7] Paul S. Bagus, Connie J. Nelin, Eugene S. Ilton, Michel J. Sassi, and Kevin M. Rosso. Analysis of X-Ray Adsorption Edges: $L_{2,3}$ Edge of $FeCl_4^-$. *Journal of Chemical Physics*, 147(22):224306, 2017.

[8] Jefferson E. Bates and Toru Shiozaki. Fully Relativistic Complete Active Space Self-Consistent Field for Large Molecules: Quasi-second-order Minimax Optimization. *Journal of Chemical Physics*, 142(4):044112, 2015.

[9] Stefano Battaglia, Sebastian Keller, and Stefan Knecht. Efficient Relativistic Density-Matrix Renormalization Group Implementation in a Matrix-Product Formulation. *Journal of Chemical Theory and Computation*, 14(5):2353–2369, 2018.

[10] Kurt H. Becker, Nazieh M. Masoud, Kevin E. Martus, and Karl H. Schoenbach. Electron-driven Processes in High-pressure Plasmas. *The European Physical Journal D - Atomic, Molecular, Optical and Plasma Physics*, 35(2):279–297, 2005.

[11] Stacey F. Bent. Organic Functionalization of Group IV Semiconductor Surfaces: Principles, Examples, Applications, and Prospects. *Surface Science*, 500(1):879–903, 2002.

[12] Nicholas A. Besley. Density Functional Theory Calculations of Core–Electron Binding Energies at the K-Edge of Heavier Elements. *Journal of Chemical Theory and Computation*, 17(6):3644–3651, 2021.

[13] Nicholas A. Besley. Modeling of the Spectroscopy of Core Electrons With Density Functional Theory. *Wiley Interdisciplinary Reviews: Computational Molecular Science*, 11(6):1527, 2021.

[14] Nicholas A. Besley and Frans A. Asmuruf. Time-dependent Density Functional Theory Calculations of the Spectroscopy of Core Electrons. *Physical Chemistry Chemical Physics*, 12:12024–12039, 2010.

[15] J. C. Boettger. Approximate Two-Electron Spin-orbit Coupling Term For Density-Functional-Theory DFT Calculations Using The Douglas-Kroll-Hess Transformation. *Physical Review B*, 62:7809–7815, 2000.

[16] Sergey I. Bokarev, Marcus Dantz, Edlira Suljoti, Oliver Kühn, and Emad F. Aziz. State-Dependent Electron Delocalization Dynamics at the Solute-Solvent Interface: Soft-x-ray Absorption Spectroscopy and Ab Initio Calculations. *Physical Review Letters*, 111(8):083002, 2013.

[17] Michael C. Boyer, Nathalie Rivas, Audrey A. Tran, Clarissa A. Verish, and Christopher R. Arumainayagam. The Role of Low-energy (20eV) Electrons in Astrochemistry. *Surface Science*, 652:26–32, 2016.

[18] Abel Carreras, Hanjie Jiang, Pavel Pokhilko, Anna I. Krylov, Paul M. Zimmerman, and David Casanova. Calculation of Spin–orbit Couplings Using RASCI Spinless One-particle Density Matrices: Theory and Applications. *Journal of Chemical Physics*, 153(21):214107, 2020.

[19] Ernest R Davidson. The Iterative Calculation of a Few of the Lowest Eigenvalues and Corresponding Eigenvectors of Large Real-symmetric Matrices. *Journal of Chemical Physics*, 17(1):87–94, 1975.

[20] Frank de Groot and Akio Kotani. *Core Level Spectroscopy of Solids*. CRC Press, 2008.

[21] Serena DeBeer George, Taras Petrenko, and Frank Neese. Time-dependent Density Functional Calculations of Ligand K-edge X-ray Absorption Spectra. *Inorganica Chimica Acta*, 361(4):965–972, 2008.

[22] Mickael G. Delcey, Lasse Kragh Sørensen, Morgane Vacher, Rafael C. Couto, and Marcus Lundberg. Efficient Calculations of a Large Number of Highly Excited States for Multiconfigurational Wavefunctions. *Journal of Computational Chemistry*, 40:1789—-1799, 2019.

[23] Sujit K. Dey, A.J. Dixon, Ian E. McCarthy, and Erich Weigold. (e,2e) Spectroscopy of Ethane. *Journal of Electron Spectroscopy and Related Phenomena*, 9(4):397–412, 1976.

[24] Paul Adrien Maurice Dirac. The Quantum Theory of the Emission and Absorption of Radiation. *Proc. R. Soc. Lond. A*, 114:243–265, 1927.

[25] Kazunari Domen and Trees-Juen Chuang. Electronically Excited Photodissociation and Desorption of Adsorbates: CH_2I_2 on Al_2O_3 and Ag Surfaces. *Physical Review Letters*, 59:1484–1487, 1987.

[26] Andreas Dreuw and Shirin Faraji. A Quantum Chemical Perspective on (6-4) Photolesion Repair by Photolyases. *Phys. Chem. Chem. Phys.*, 15:19957–19969, 2013.

[27] Wlodzislaw Duch. *GRMS Or Graphical Representation of Model Spaces: Vol. 1 Basics.* Springer Science Business Media, 2012.

[28] Gérald Dujardin, Lucette Hellner, Marie-Joëlle Ramage, and Roger Azria. Desorption of Ions Following Valence Excitation of Rare-Gas Solids. *Physical Review Letters*, 64:1289–1292, 1990.

[29] Thom H. Dunning. Gaussian Basis Sets for Use in Correlated Molecular Calculations. I. The Atoms Boron through Neon and Hydrogen. *Journal of Chemical Physics*, 90(2):1007–1023, 1989.

[30] Kenneth G. Dyall. Relativistic and Nonrelativistic Finite Nucleus Optimized Triple-Zeta Basis Sets for the 4p, 5p and 6p Elements. *Theoretical Chemistry Accounts*, 108(6):335–340, 2002.

[31] Kenneth G. Dyall. Relativistic Quadruple-Zeta and Revised Triple-Zeta and Double-Zeta Basis Sets for the 4p, 5p, and 6p Elements. *Theoretical Chemistry Accounts*, 115(5):441–447, 2006.

[32] Franco Egidi, Joshua J. Goings, Michael J. Frisch, and Xiaosong Li. Direct Atomic-Orbital-Based Relativistic Two-Component Linear Response Method for Calculating Excited-State Fine Structures. *Journal of Chemical Theory and Computation*, 12(8):3711–3718, 2016.

[33] Franco Egidi, Shichao Sun, Joshua J. Goings, Giovanni Scalmani, Michael J. Frisch, and Xiaosong Li. Two-Component Non-Collinear Time-Dependent Spin Density Functional Theory for Excited State Calculations. *Journal of Chemical Theory and Computation*, 13(6):2591–2603, 2017.

[34] Nicholas Engel, Sergey I. Bokarev, Edlira Suljoti, Raul Garcia-Diez, Kathrin M. Lange, Kaan Atak, Ronny Golnak, Alexander Kothe, Marcus Dantz, Oliver Kühn, and Emad F. Aziz. Chemical Bonding in Aqueous Ferrocyanide: Experimental and Theoretical X-ray Spectroscopic Study. *Journal of Physical Chemistry B*, 118(6):1555–1563, 2014.

[35] B. Scott Fales and Todd J. Martínez. Efficient Treatment of Large Active Spaces through Multi-GPU Parallel Implementation of Direct Configuration Interaction. *Journal of Chemical Theory and Computation*, 16(3):1586–1596, 2020.

[36] E Fasshauer, M Förstel, S Pallmann, M Pernpointner, and U Hergenhahn. Using ICD for Structural Analysis of Clusters: a Case Study on NeAr clusters. *New Journal of Physics*, 16(10):103026, 2014.

[37] Elke Fasshauer, Markus Pernpointner, and Kirill Gokhberg. Interatomic Decay of Inner-valence Ionized States in ArXe Clusters: Relativistic Approach. *The Journal of Chemical Physics*, 138(1), 2013.

[38] Vladimir I. Feldman, Fedor F. Sukhov, Aleksei Yu. Orlov, and Nina A. Shmakova. Effect of Matrix Electronic Characteristics on Trapping and Degradation of Organic Radical Cations in Solid Rare Gases: A Case Study of Methylal Radical Cation. *The Journal of Physical Chemistry A*, 104(16):3792–3799, 2000.

[39] Enrico Fermi. *Nuclear Physics: a Course Given by Enrico Fermi at the University of Chicago*. University of Chicago Press, 1950.

[40] Timo Fleig, Hans Jørgen Aa. Jensen, Jeppe Olsen, and Lucas Visscher. The Generalized Active Space Concept for the Relativistic Treatment of Electron Correlation. III. Large-scale Configuration Interaction and Multiconfiguration Self-Consistent-Field Four-Component Methods with Application to UO2. *The Journal of Chemical Physics*, 124(10):104106, 2006.

[41] Timo Fleig, Christel M Marian, and Jeppe Olsen. Spinor Optimization for a Relativistic Spin-dependent CASSCF Program. *Theoretical Chemistry Accounts*, 97(1-4):125–135, 1997.

[42] Timo Fleig, Jeppe Olsen, and Christel M. Marian. The Generalized Active Space Concept for the Relativistic Treatment of Electron Correlation. I. Kramers-restricted Two-component Configuration Interaction. *The Journal of Chemical Physics*, 114(11):4775–4790, 2001.

[43] Timo Fleig, Jeppe Olsen, and Lucas Visscher. The Generalized Active Space Concept for the Relativistic Treatment of Electron Correlation. II. Large-scale Configuration Interaction Implementation based on Relativistic 2- and 4-spinors and its Application. *The Journal of Chemical Physics*, 119(6):2963–2971, 2003.

[44] Giovanna Fronzoni, Renato De Francesco, and Mauro Stener. Time Dependent Density Functional Theory of X-ray Absorption Spectroscopy of Alkaline-Earth Oxides. *Journal of Physical Chemistry B*, 109(20):10332–10340, 2005.

[45] Zhengting Gan and R.J. Harrison. Calibrating Quantum Chemistry: A Multi-Teraflop, Parallel-vector, Full-configuration Interaction Program for the Cray-X1. In *SC '05: Proceedings of the 2005 ACM/IEEE Conference on Supercomputing*, pages 22–22, 2005.

[46] Vanesa M. García, Rosa Caballol, and Jean P. Malrieu. Treatment of Core-valence Correlation Effects through Difference-dedicated Configuration Interaction: Application to the Lowest Electronic States of K, Rb, KH, RbH, and K_2. *Journal of Chemical Physics*, 109(2):504–511, 1998.

[47] Joshua J. Goings, Joseph M. Kasper, Franco Egidi, Shichao Sun, and Xiaosong Li. Real Time Propagation of the Exact Two Component Time-Dependent Density Functional Theory. *Journal of Chemical Physics*, 145(10):104107, 2016.

[48] Gregory A. Grieves and Thomas M. Orlando. Intermolecular Coulomb Decay at Weakly Coupled Heterogeneous Interfaces. *Physical Review Letters*, 107:016104, 2011.

[49] Meiyuan Guo, Lasse Kragh Sørensen, Mickaël G. Delcey, Rahul V. Pinjari, and Marcus Lundberg. Simulations of Iron K Pre-edge X-ray Absorption Spectra Using the Restricted Active Space Method. *Physical Chemistry Chemical Physics*, 18(4):3250–3259, 2016.

[50] Loic Halbert, Marta L. Vidal, Avijit Shee, Sonia Coriani, and André Severo Pereira Gomes. Relativistic EOM-CCSD for Core-Excited and Core-Ionized State Energies Based on the Four-Component Dirac–Coulomb(Gaunt) Hamiltonian. *Journal of Chemical Theory and Computation*, 17(6):3583–3598, 2021.

[51] Michael Hawley and Mark A. Smith. Charge-transfer Chemistry of Argon(1+) (2P3/2) and Krypton(1+) (2P3/2) at Very Low Collision Energies. *The Journal of Physical Chemistry*, 96(16):6693–6697, 1992.

[52] Uwe Hergenhahn. Interatomic and Intermolecular Coulombic Decay: The Early Years. *Journal of Electron Spectroscopy and Related Phenomena*, 184(3):78–90, 2011.

[53] Zdenek Herman and Břetislav Friedrich. A Crossed-Beam Scattering Study of CH+4 and CH+3 Formation in Charge Transfer Collisions of Kr+ with CH4 at about 1 eV. *The Journal of Chemical Physics*, 102(18):7017–7023, 1995.

[54] Zdeněk K. Herman, Keith Birkinshaw, and V. Pacák. A Beam Scattering Study of Non-dissociative Charge Transfer between Kr+ and CH4 at Collision Energies Below 1 eV. *International Journal of Mass Spectrometry and Ion Processes*, 135(1):47–53, 1994.

[55] Janine Herring, Alex Aleksandrov, and Thomas M. Orlando. Stimulated Desorption of Cations from Pristine and Acidic Low-Temperature Water Ice Surfaces. *Physical Review Letters*, 92:187602, 2004.

[56] Janine Herring-Captain, Gregory A. Grieves, Alex Alexandrov, Matthew T. Sieger, Haiyan Chen, and Thomas M. Orlando. Low-energy ($5--250$ eV) Electron-stimulated Desorption of H^+, H_2^+, and $H^+(H_2O)_n$ from Low-temperature Water Ice Surfaces. *Phys. Rev. B*, 72:035431, 2005.

[57] Kimihiko Hirao and Sigeru Huzinaga. Improved Virtual Orbitals in the Potential of the SCF Ion. *Chemical Physics Letters*, 45(1):55–58, 1977.

[58] Hang Hu, Andrew J. Jenkins, Hongbin Liu, Joseph M. Kasper, Michael J. Frisch, and Xiaosong Li. Relativistic Two-Component Multireference Configuration Interaction Method with Tunable Correlation Space. *Journal of Chemical Theory and Computation*, 16(5):2975–2984, 2020.

[59] William J. Hunt and William A. Goddard. Excited States of H_2O Using Improved Virtual Orbitals. *Chemical Physics Letters*, 3(6):414–418, 1969.

[60] Miroslaŵ Ilias and Trond Saue. An Infinite-order Relativistic Hamiltonian by a Simple One-Step Transformation. *Journal of Chemical Physics*, 126:064102, 2007.

[61] Till Jahnke, Uwe Hergenhahn, Bernd Winter, Reinhard Dörner, Ulrike Frühling, Philipp V. Demekhin, Kirill Gokhberg, Lorenz S. Cederbaum, Arno Ehresmann, André Knie, and Andreas Dreuw. Interatomic and Intermolecular Coulombic Decay. *Chemical Reviews*, 120(20):11295–11369, 2020.

[62] Andrew J. Jenkins, Hang Hu, Lixin Lu, Michael J. Frisch, and Xiaosong Li. Two-Component Multireference Restricted Active Space Configuration Interaction for the Computation of L-Edge X-ray Absorption Spectra. *Journal of Chemical Theory and Computation*, 18(1):141–150, 2022.

[63] Andrew J. Jenkins, Hongbin Liu, Joseph M. Kasper, Michael J. Frisch, and Xiaosong Li. Variational Relativistic Complete Active Space Self-Consistent Field Method. *Journal of Chemical Theory and Computation*, 15:2974–2982, 2019.

[64] Hans J Aa. Jensen, Kenneth G. Dyall, Trond Saue, and Knut Fægri. Relativistic Four-component Multiconfigurational Self-Consistent-Field Theory for Molecules: Formalism. *Journal of Chemical Physics*, 104(11):4083–4097, 1996.

[65] Brant M. Jones, Alexandr Aleksandrov, Xin Zhang, Kevin M. Rosso, and Thomas M. Orlando. Electron- and Thermal-Stimulated Synthesis of Water on Boehmite (-AlOOH) Nanoplates. *The Journal of Physical Chemistry C*, 123(31):18986–18992, 2019.

[66] Ida Josefsson, Kristjan Kunnus, Simon Schreck, Alexander Föhlisch, Frank de Groot, Philippe Wernet, and Michael Odelius. Ab Initio Calculations of X-ray Spectra: Atomic Multiplet and Molecular Orbital Effects in a Multiconfigurational SCF Approach to the L-Edge Spectra of Transition Metal Complexes. *Journal of Physical Chemistry Letters*, 3(23):3565–3570, 2012.

[67] Joseph M. Kasper, Torin F. Stetina, Andrew J. Jenkins, and Xiaosong Li. Ab Initio Methods for L-edge X-ray Absorption Spectroscopy. 1(1):011304, 2020.

[68] Victor Kaufman and Leon J. Radziemski. The Sixth Spectrum of Uranium (U(VI)). *J. Opt. Soc. Am.*, 66(6):599–600, 1976.

[69] Hitoshi Kawanowa, Kaoru Hanatani, Yukiko Gotoh, and Ryutaro Souda. Electron-Stimulated Desorption of Positive Ions from Methanol Adsorbed on a Solid Ar Substrate. *Surface Review and Letters*, 10(02n03):271–275, 2003.

[70] Hitoshi Kawanowa, Masayuki Kondo, Kiyoshi Hanatani, Yoshihiko Gotoh, and Ryutaro Souda. Electron Stimulated Desorption of Cations from C6H6 and C6H12 Molecules Adsorbed on Pt(111) and Ar Spacer Layer. *Nuclear Instruments and Methods in Physics Research Section B: Beam Interactions with Materials and Atoms*, 203:178–182, 2003.

[71] Inkoo Kim and Yoon Sup Lee. Two-component Kramers Restricted Complete Active Space Self-Consistent Field Method with Relativistic Effective Core Potential Revisited: Theory, Implementation, and Applications to Spin-orbit Splitting of Lower p-Block Atoms. *Journal of Chemical Physics*, 139(13):134115, 2013.

[72] Yong Seok Kim and Yoon Sup Lee. The Kramers' Restricted Complete Active Space Self-Consistent-Field Method for Two-Component Molecular Spinors and Relativistic Effective Core Potentials Including Spin–Orbit Interactions. *Journal of Chemical Physics*, 119(23):12169–12178, 2003.

[73] Stefan Knecht, Hans Jørgen Aa. Jensen, and Trond Saue. Relativistic Quantum Chemical Calculations Show that the Uranium Molecule U_2 Has a Quadruple Bond. *Nature Chemistry*, 11(1):40–44, 2019.

[74] Stefan Knecht, Hans Jørgen Aa. Jensen, and Timo Fleig. Large-scale Parallel Configuration Interaction. I. Nonrelativistic and Scalar-relativistic General Active Space Implementation with Application to (Rb–Ba)+. *Journal of Chemical Physics*, 128(1):014108, 2008.

[75] Stefan Knecht, Hans Jørgen Aa. Jensen, and Timo Fleig. Large-scale Parallel Configuration Interaction. II. Two- and Four-component Double-group General Active Space Implementation with Application to BiH. *Journal of Chemical Physics*, 132(1):014108, 2010.

[76] Stefan Knecht, Ös Legeza, and Markus Reiher. Communication: Four-component Density Matrix Renormalization Group. *Journal of Chemical Physics*, 140(4):041101, 2014.

[77] Michael L. Knotek. Stimulated Desorption. *Reports on Progress in Physics*, 47(11):1499, 1984.

[78] Michael L. Knotek and Peter J. Feibelman. Ion Desorption by Core-Hole Auger Decay. *Physical Review Letters*, 40:964–967, 1978.

[79] Peter J Knowles and Nicholas C. Handy. A New Determinant-based Full Configuration Interaction Method. *Chemical Physics Letters*, 111(4-5):315–321, 1984.

[80] Peter J. Knowles and Nicholas C. Handy. A Determinant Based Full Configuration Interaction program. *Computer Physics Communications*, 54(1):75–83, 1989.

[81] Lukas Konecny, Marius Kadek, Stanislav Komorovsky, Olga L. Malkina, Kenneth Ruud, and Michal Repisky. Acceleration of Relativistic Electron Dynamics by Means of

X2C Transformation: Application to the Calculation of Nonlinear Optical Properties. *Journal of Chemical Theory and Computation*, 12(12):5823–5833, 2016.

[82] Joanna K. Kowalska, Brahamjot Nayyar, Julian A. Rees, Christine E. Schiewer, Sonny C. Lee, Julie A. Kovacs, Franc Meyer, Thomas Weyhermüller, Edwige Otero, and Serena DeBeer. Iron $L_{2,3}$-Edge X-ray Absorption and X-ray Magnetic Circular Dichroism Studies of Molecular Iron Complexes with Relevance to the FeMoco and FeVco Active Sites of Nitrogenase. *Inorganic Chemistry*, 56(14):8147–8158, 2017.

[83] Takihiro Kozawa, Hiroki Yamamoto, akinori Saeki, and Seiichi Tagawa. Effects of Low Energy Electrons on Pattern Formation in Chemically Amplified Resist. *Journal of Photopolymer Science and Technology*, 19(3):361–366, 2006.

[84] J. Kočišek, J. Lengyel, M. Fárník, and P. Slavíček. Energy and Charge transfer in Ionized Argon Coated Water Clusters. *The Journal of Chemical Physics*, 139(21), 2013.

[85] Alexander Kramida, Yuri Ralchenko, Joseph Reader, and NIST ASD Team. NIST Atomic Spectra Database (version 5.6.1), 2018. National Institute of Standards and Technology, Gaithersburg, MD.

[86] Sramana Kundu, Hang Hu, Xiaosong Li, Micah Schaible, and Thomas M. Orlando. Electron Scattering with Ethane Adsorbed on Rare Gas Multilayers: Hole transfer, Coulomb Decay, and Ion Dissociation. *Journal of Chemical Physics*, 158(12):124309, 2023.

[87] Sramana Kundu, Micah J. Schaible, Aaron D. McKee, and Thomas M. Orlando. Direct Damage of Deoxyadenosine Monophosphate by Low-Energy Electrons Probed by X-ray Photoelectron Spectroscopy. *The Journal of Physical Chemistry B*, 124(9):1585–1591, 2020.

[88] Werner Kutzlenigg and Wenjian Liu. Quasirelativistic Theory Equivalent to Fully Relativistic Theory. *Journal of Chemical Physics*, 123:241102, 2005.

[89] Hakaru Kyuragi. Role of Low-energy Secondary Electrons in Synchrotron Radiation-Excited Chemical Vapor Deposition of Silicon Nitride Films. *Journal of Vacuum Science Technology A*, 15(5):2644–2652, 1997.

[90] Anne Lafosse, Mathieu Bertin, and Roger Azria. Electron Driven Processes in Ices: Surface Functionalization and Synthesis Reactions. *Progress in Surface Science*, 84(5):177–198, 2009.

[91] Patrick J. Lestrange, Phu D. Nguyen, and Xiaosong Li. Calibration of Energy-Specific TDDFT for Modeling K-Edge XAS Spectra of Light Elements. *Journal of Chemical Theory and Computation*, 11:2994–2999, 2015.

[92] Shaopeng Li. *Development of Algorithms for the Direct Multi-Configuration Self- Consistent Field (MCSCF) Method*. PhD thesis, 1996.

[93] Zhendong Li, Yunlong Xiao, and Wenjian Liu. On the Spin Separation of Algebraic Two-Component Relativistic Hamiltonians. *Journal of Chemical Physics*, 137:154114, 2012.

[94] Junzi Liu and Lan Cheng. Relativistic Coupled-Cluster and Equation-of-Motion Coupled-Cluster Methods. *Wiley Interdisciplinary Reviews: Computational Molecular Science*, 11(6):1536, 2021.

[95] Wenjian Liu. Ideas of Relativistic Quantum Chemistry. *Molecular Physics*, 108:1679–1706, 2010.

[96] Wenjian Liu and Daoling Peng. Infinite-order Quasirelativistic Density Functional Method Based on the Exact Matrix Quasirelativistic Theory. *Journal of Chemical Physics*, 125:044102, 2006.

[97] Wenjian Liu and Daoling Peng. Exact Two-component Hamiltonians Revisited. *Journal of Chemical Physics*, 131(3):031104, 2009.

[98] Per-Olov Löwdin. Quantum Theory of Many-Particle Systems. III. Extension of the Hartree-Fock Scheme to Include Degenerate Systems and Correlation Effects. *Physical Review*, 97:1509–1520, 1955.

[99] Marcus Lundberg and Mickaël G. Delcey. *Multiconfigurational Approach to X-ray Spectroscopy of Transition Metal Complexes*, pages 185–217. Springer International Publishing, Cham, 2019.

[100] Theodore E. Madey, Robert E. Johnson, and Thom M. Orlando. Far-out Surface Science: Radiation-Induced Surface Processes in the Solar System. *Surface Science*, 500(1):838–858, 2002.

[101] Per Åke Malmqvist, Alistair Rendell, and Björn O. Roos. The Restricted Active Space Self-consistent-field Method, Implemented with a Split Graph Unitary Group Approach. *Journal of Physical Chemistry*, 94(14):5477–5482, 1990.

[102] Timothy W. Marin, Charles D. Jonah, and David M. Bartels. Reaction of OH* Radicals with H_2 in Sub-critical Water. *Chemical Physics Letters*, 371(1):144–149, 2003.

[103] Aaron D. McKee, Micah J. Schaible, Rutger A. Rosenberg, Sramana Kundu, and Thomas M. Orlando. Low Energy Secondary Electron Induced Damage of Condensed Nucleotides. *Journal of Chemical Physics*, 150(20):204709, 2019.

[104] Dan Meisel, Donald M. Camaioni, and Thom M. Orlando. *Radiation and Chemistry in Nuclear Waste: The NO_x System and Organic Aging*, chapter 21, pages 342–361. 2000.

[105] Patrick Norman and Andreas Dreuw. Simulating X-ray Spectroscopies and Calculating Core-Excited States of Molecules. *Chemical Reviews*, 118(15):7208–7248, 2018.

[106] Takeshi Noro, Masahiro Sekiya, and Toshikatsu Koga. Segmented Contracted Basis Sets for Atoms H Through Xe: Sapporo-(DK)-nZP Sets (n = D, T, Q). *Theoretical Chemistry Accounts*, 131:1124, 2012.

[107] Jeppe Olsen. The Initial Implementation and Applications of a General Active Space Coupled Cluster Method. *Journal of Chemical Physics*, 113(17):7140–7148, 2000.

[108] Jeppe Olsen, Poul Jørgensen, and Jack Simons. Passing the One-Billion Limit in Full Configuration-Interaction (FCI) Calculations. *Chemical Physics Letters*, 169(6):463–472, 1990.

[109] Jeppe Olsen, Björn O. Roos, Poul Jørgensen, and Hans Jørgen Aa. Jensen. Determinant Based Configuration Interaction Algorithms for Complete and Restricted Configuration Interaction Spaces. *Journal of Chemical Physics*, 89(4):2185–2192, 1988.

[110] Dimitrios A. Pantazis and Frank Neese. All-Electron Scalar Relativistic Basis Sets for the Actinides. *Journal of Chemical Theory and Computation*, 7(3):677–684, 2011.

[111] Bo Peng, Patrick J Lestrange, Joshua J Goings, Marco Caricato, and Xiaosong Li. Energy-Specific Equation-of-Motion Coupled-Cluster Methods for High-Energy Excited States: Application to K-Edge X-Ray Absorption Spectroscopy. *Journal of Chemical Theory and Computation*, 11(9):4146–4153, 2015.

[112] Daoling Peng, Wenjian Liu, Yunlong Xiao, and Lan Cheng. Making Four- and Two-Component Relativistic Density Functional Methods Fully Equivalent Based on the Idea of From Atoms to Molecule. *Journal of Chemical Physics*, 127:104106, 2007.

[113] Daoling Peng, Nils Middendorf, Florian Weigend, and Markus Reiher. An Efficient Implementation of Two-Component Relativistic Exact-Decoupling Methods for Large Molecules. *Journal of Chemical Physics*, 138:184105, 2013.

[114] Widmark Per-Olof, Persson B. Joakim, and Roos Björn O. Density Matrix Averaged Atomic Natural Orbital (ANO) Basis Sets for Correlated Molecular Wave Functions II. Second Row Atoms. *Theoretical Chemistry Accounts*, 79:419–432, 1991.

[115] Kristine Pierloot. The CASPT2 Method in Inorganic Electronic Spectroscopy: from Ionic Transition Metal to Covalent Actinide Complexes. *Molecular Physics*, 101(13):2083–2094, 2003.

[116] Rahul V. Pinjari, Michaël G. Delcey, Meiyuan Guo, Michaël Odelius, and Marcus Lundberg. Restricted Active Space Calculations of L-edge X-ray Absorption Spectra: From Molecular Orbitals to Multiplet States. *Journal of Chemical Physics*, 141(12):124116, 2014.

[117] Rahul V. Pinjari, Mickaël G. Delcey, Meiyuan Guo, Michael Odelius, and Marcus Lundberg. Cost and Sensitivity of Restricted Active-space Calculations of Metal L-edge X-ray Absorption Spectra. *Journal of Computational Chemistry*, 37(5):477–486, 2016.

[118] Rahul V. Pinjari, Mickaël G. Delcey, Meiyuan Guo, Michael Odelius, and Marcus Lundberg. Erratum: "Restricted Active Space Calculations of L-edge X-ray Absorption Spectra: From Molecular Orbitals to Multiplet States" [J. Chem. Phys. 141, 124116 (2014)]. *Journal of Chemical Physics*, 142(6):069901, 2015.

[119] Patrik Pollak and Florian Weigend. Segmented Contracted Error-Consistent Basis Sets of Double- and Triple-Valence Quality for One- and Two-Component Relativistic All-Electron Calculations. *Journal of Chemical Theory and Computation*, 13(8):3696–3705, 2017.

[120] C. Praxmarer, Armin Hansel, Werner Lindinger, and Zdeněk Herman. A Selected-ion-flow-drift-tube Study of Charge Transfer Processes between Atomic, Molecular, and Dimer Ion Projectiles and Polyatomic Molecules Ethane, Propane, and n-butane. *The Journal of Chemical Physics*, 109(11):4246–4251, 1998.

[121] David E. Ramaker. Comparison of Photon Stimulated Dissociation of Gas Phase and Chemisorbed CO. *The Journal of Chemical Physics*, 78(6):2998–3013, 1983.

[122] Xueguang Ren, Enliang Wang, Anna D. Skitnevskaya, Alexander B. Trofimov, Kirill Gokhberg, and Alexander Dorn. Experimental Evidence for Ultrafast Intermolecular

Relaxation Processes in Hydrated Biomolecules. *Nature Physics*, 14(10):1062–1066, 2018.

[123] Clemens Richter, Daniel Hollas, Clara-Magdalena Saak, Marko Förstel, Tsveta Miteva, Melanie Mucke, Olle Björneholm, Nicolas Sisourat, Petr Slavíček, and Uwe Hergenhahn. Competition between proton transfer and intermolecular Coulombic decay in water. *Nature Communications*, 9(1):4988, 2018.

[124] Björn O. Roos, Roland Lindh, Per-Åke Malmqvist, Valera Veryazov, and Per-Olof Widmark. Main Group Atoms and Dimers Studied with a New Relativistic ANO Basis Set. *Journal of Physical Chemistry A*, 108(15):2851–2858, 2004.

[125] Björn O. Roos, Roland Lindh, Per-Åke Malmqvist, Valera Veryazov, and Per-Olof Widmark. *Multiconfigurational Quantum Chemistry*. Wiley, 2016.

[126] Björn O. Roos and Per-Åke Malmqvist. Relativistic Quantum Chemistry: The Multiconfigurational Approach. *Physical Chemistry Chemical Physics*, 6(11):2919–2927, 2004.

[127] Pou-Amerigo Rosendo, Merchan Manuela, Nebot-Gil Ignacio, Widmark Per-Olof, and Roos Björn O. Density Matrix Averaged Atomic Natural Orbital (ANO) Basis Sets for Correlated Molecular Wave Functions III. First Row Transition Metal Atoms. *Theoretical Chemistry Accounts*, 92:149–181, 1995.

[128] Elda Rossi, Gian Luigi Bendazzoli, Stefano Evangelisti, and Daniel Maynau. A Full-Configuration Benchmark for the N2 Molecule. *Chemical Physics Letters*, 310(5):530–536, 1999.

[129] Léon Sanche. Role of Secondary Low Energy Electrons in Radiobiology and Chemoradiation Therapy of Cancer. *Chemical Physics Letters*, 474(1):1–6, 2009.

[130] Robin Santra, Jürgen Zobeley, Lorenz S. Cederbaum, and Nimrod Moiseyev. Interatomic Coulombic Decay in van der Waals Clusters and Impact of Nuclear Motion. *Physical Review Letters*, 85:4490–4493, 2000.

[131] Trond Saue. Relativistic Hamiltonians for Chemistry: A Primer. *ChemPhysChem*, 12:3077–3094, 2011.

[132] Toru Shiozaki and Wataru Mizukami. Relativistic Internally Contracted Multireference Electron Correlation Methods. *Journal of Chemical Theory and Computation*, 11(10):4733–4739, 2015.

[133] Per E.M. Siegbahn. A New Direct CI Method for Large CI Expansions in a Small Orbital Space. *Chemical Physics Letters*, 109(5):417–423, 1984.

[134] Jetze Sikkema, Lucas Visscher, Trond Saue, and Miroslav Iliaš. The Molecular Mean-Field Approach for Correlated Relativistic Calculations. *Journal of Chemical Physics*, 131(12):124116, 2009.

[135] Petr Slavíček, Nikolai V. Kryzhevoi, Emad F. Aziz, and Bernd Winter. Relaxation Processes in Aqueous Systems upon X-ray Ionization: Entanglement of Electronic and Nuclear Dynamics. *The Journal of Physical Chemistry Letters*, 7(2):234–243, 2016.

[136] Ryutaro Souda. Ion-surface Charge Exchange during Sputtering and Low-energy H^+ Scattering from Ar, Kr, and Xe Layers Formed on Metal Surfaces. *Physical Review B*, 63:113407, 2001.

[137] Ryutaro Souda. Electron-Stimulated Desorption of Positive Ions from Methane and Fluoromethane Nanoclusters. *The Journal of Chemical Physics*, 116(19):8556–8559, 2002.

[138] Ryutaro Souda. Electron Stimulated Solvation and Reaction of Water, Ammonia, and Methane in Nanoclusters Adsorbed on Solid Ar Substrate. *The Journal of Chemical Physics*, 117(13):5967–5970, 2002.

[139] Ryutaro Souda. Radiolysis of NH3, C2H6, C2H4, and C2F6 Molecules in Physisorbed Ultrathin Films Studied by Electron-stimulated Desorption. *Chemical Physics Letters*, 382(3):387–392, 2003.

[140] Joseph Sucher. Foundations of the Relativistic Theory of Many-electron Atoms. *Physical Review A*, 22:348–362, 1980.

[141] Shichao Sun, Torin F. Stetina, Tianyuan Zhang, Hang Hu, Edward F. Valeev, Qiming Sun, and Xiaosong Li. Efficient Four-Component Dirac–Coulomb–Gaunt Hartree–Fock in the Pauli Spinor Representation. *Journal of Chemical Theory and Computation*, 17(6):3388–3402, 2021.

[142] Attila Szabo and Neil S. Ostlund. *Modern Quantum Chemistry: Introduction to Advanced Electronic Structure Theory*. Dover Publications, 1996.

[143] Roland Thissen, Pascal Lablanquie, Roland I. Hall, Masashi Ukai, and Kenji Ito. Photoionization of Argon, Krypton and Xenon Clusters in the Inner Valence Shell Region. *Journal of Chemical Physics*, 4(3):335–342, 1998.

[144] Jørn Thyssen, Timo Fleig, and Hans Jørgen Aa Jensen. A Direct Relativistic Four-component Multiconfiguration Self-Consistent-Field Method for Molecules. *Journal of Chemical Physics*, 129(3):034109, 2008.

[145] Lea Thøgersen and Jeppe Olsen. A Coupled Cluster and Full Configuration Interaction Study of CN and CN. *Chemical Physics Letters*, 393(1):36–43, 2004.

[146] Masaharu Tsuji, Hiroyuki Kouno, Ken-ichi Matsumura, Tsuyoshi Funatsu, Yukio Nishimura, Hiroshi Obase, Hirofumi Kugishima, and Kouichi Yoshida. Dissociative Charge-transfer Reactions of Ar+ with Simple Aliphatic Hydrocarbons at Thermal Energy. *The Journal of Chemical Physics*, 98(3):2011–2022, 1993.

[147] Willem F. van Dorp, Cornelis W. Hagen, Peter A. Crozier, and Pieter Kruit. Growth Behavior Near the Ultimate Resolution of Nanometer-scale Focused Electron Beam-induced Deposition. *Nanotechnology*, 19(22):225305, 2008.

[148] Marta L. Vidal, Pavel Pokhilko, Anna I. Krylov, and Sonia Coriani. Equation-of-Motion Coupled-Cluster Theory to Model L-Edge X-ray Absorption and Photoelectron Spectra. *Journal of Physical Chemistry Letters*, 11(19):8314–8321, 2020.

[149] Konstantinos D. Vogiatzis, Dongxia Ma, Jeppe Olsen, Laura Gagliardi, and Wibe A. de Jong. Pushing Configuration-Interaction to the Limit: Towards Massively Parallel MCSCF Calculations. *Journal of Chemical Physics*, 147(18):184111, 2017.

[150] R. von Pietrowski, Klaus von Haeften, Tim Laarmann, Thomas Möller, Luc Museur, and Andrei V. Kanaev. Electronic and Geometric Structure of Doped Rare-Gas Clusters: Surface, Site and Size Effects Studied with Luminescence Spectroscopy. *The European Physical Journal D - Atomic, Molecular, Optical and Plasma Physics*, 38(2):323–336, 2006.

[151] Erik C. Wasinger, Frank M.F. de Groot, Britt Hedman, Keith O. Hodgson, and Edward I. Solomon. L-edge X-ray Absorption Spectroscopy of Non-heme Iron Sites: Experimental Determination of Differential Orbital Covalency. *Journal of the American Chemical Society*, 125(42):12894–12906, 2003.

[152] Hans-Joachim Werner and Peter J Knowles. An Efficient Internally Contracted Multiconfiguration-Reference Configuration Interaction Method. *Journal of Chemical Physics*, 89(9):5803–5814, 1988.

[153] Jiazhan Xu, Wolfgang J. Choyke, and John T. Yates. Enhanced Silicon Oxide Film Growth on Si (100) using Electron Impact. *Journal of Applied Physics*, 82(12):6289–6292, 1997.

[154] Boyi Zhang, Jonathon E. Vandezande, Ryan D. Reynolds, and Henry F. Schaefer. Spin-orbit Coupling via Four-Component Multireference Methods: Benchmarking on p-Block Elements and Tentative Recommendations. *Journal of Chemical Theory and Computation*, 14(3):1235–1246, 2018.

[155] Xiaoyang Zhu. Surface Photochemistry. *Annual Review of Physical Chemistry*, 45(1):113–144, 1994.